

THEORETICAL STUDIES ON ELECTRONIC
SPECTRA OF HETEROGENEOUS
UNCONVENTIONAL SUPERCONDUCTORS

A Dissertation

Presented to the Faculty of the Graduate School

of Cornell University

in Partial Fulfillment of the Requirements for the Degree of

Doctor of Philosophy

by

Kyungmin Lee

August 2016

© 2016 Kyungmin Lee

ALL RIGHTS RESERVED

THEORETICAL STUDIES ON ELECTRONIC SPECTRA OF
HETEROGENEOUS UNCONVENTIONAL SUPERCONDUCTORS

Kyungmin Lee, Ph.D.

Cornell University 2016

Spectroscopy serves as a window into the physics of condensed matter systems. In the study of unconventional superconductors, spectroscopic probes such as scanning tunneling spectroscopy, angle-resolved photoemission spectroscopy, and optical measurements have played important roles in determination of their gap structure, which is a crucial piece of information in uncovering the mechanism of high temperature superconductivity, as well as a stepping stone for theoretical studies of exotic physics of the materials. Although these unconventional superconductors often are highly heterogeneous, theoretical calculation of electronic spectra for heterogeneous systems is non-trivial.

In this dissertation we present theoretical studies on electronic spectra of heterogeneous unconventional superconductors. We begin with a study on proximity induced topological superconductivity in topological metal-superconductor heterostructure. Contrary to the heterostructure suggested by Fu and Kane, where topological superconductivity is limited to the interface between topological insulator and superconductor, finite density of states at Fermi level carries superconductivity to the naked surface of topological metal, allowing surface probes access to topological superconductivity. We then present an analysis of scanning tunneling spectroscopy measurement on LiFeAs. We find signatures of coupling between electron and antiferromagnetic spin fluctuation, strongly suggesting the role of the bosonic mode in the pairing mechanism of the material's superconductivity.

We then move on to a discussion of various electronic spectra in superconducting cuprates, namely, how glassy nematicity affects local density of states, spectral function, and optical conductivity. We find that heterogeneity of glassy state and the form factor of nematicity work together to produce a number of “anomalous” features in the electronic spectra observed in underdoped cuprates. Lastly, we discuss near-vortex electronic spectra in superconducting LiFeAs under magnetic field. From the spatial dependence of tunneling spectra, we argue that the gap structure of LiFeAs can be deduced.

BIOGRAPHICAL SKETCH

As a child, Kyungmin Lee wanted to be a scientist, who, to him at the time, was a person in a lab coat, mixing colorful liquids in flasks to make robots. After learning physics, he was intrigued by the laws of the universe, and decided to study them. He entered Daegu Science High School, where he spent many nights discussing with friends planets in orbits, rotating buckets, and trains moving close to the speed of light. (He had not heard of the cruelty done to an Austrian cat.) The time he spent eventually won him two trips abroad, to Leicester, U. K. and Antalya, Turkey.

Kyungmin decided to continue his pursuit of interest in physics at Seoul National University, where he majored in physics and computer science. During college he became interested in the physics of many bodies. After graduating from SNU, he moved to Ithaca, New York to start his career in academia at Cornell University and joined Eun-Ah Kim's group. He studied theories of various types of unconventional superconductivity during his Ph.D. program at Cornell. After seven years, through peaks and valleys, he arrived at the end of his journey in Ithaca.

*To my parents
and my sister.*

ACKNOWLEDGEMENTS

Seven years have passed since I came to Ithaca. During those years, I have come across many wonderful people whom I owe much to.

I consider myself extremely lucky to have had Eun-Ah Kim as my advisor and mentor, without whom the works presented in this dissertation would not have been possible. Everything I know about being a researcher I learned from her: how to approach problems, how to communicate, and to think about making a contribution to the scientific community. I do not have words to express my gratitude for all her efforts to reach me and guide me in the right direction.

I would also like to thank Séamus Davis and Erich Mueller for being wonderful committee members. Their insightful comments and feedback not only during the writing of this dissertation, but throughout the whole Ph.D. program, have provided a broader perspective on physics.

I have been very fortunate to have remarkable people in the group: Yi-Ting Hsu, who always comes up with interesting questions, and persevered through many hours of my nonsensical ramblings; Oinam Nganba Meetei, who I could discuss the finest details of calculations and gave me relief; Andrej Mesaros, who, with such breadth and depth of interest and knowledge, could explain almost anything in ways that even I could understand; Jian-Huang She, who has taught me a great deal through discussions on iron-based superconductors and critical phenomena; and Abolhassan Vaezi, who has inspired me with his intuition on abstract concepts.

I would like to thank many friends that I met in Ithaca: People from my year who have helped my soft landing to Ithaca – Kartik Ayyer, Thomas Bachlechner, Inês Firmo, Shivam Ghosh, Mihir Khadilkar, and Jesse Silverberg; my officemates Matthew Reichl and Bhuvanesh Sundar who I enjoyed sharing office with, as well

as all the crossword puzzles we played; and Ran Wei, who has been a real good friend in the last years of my graduate school.

I owe my survival through seven years of graduate school in Ithaca to all these great people, and also many others.

TABLE OF CONTENTS

1	Introduction	1
2	Overview on Bardeen-Cooper-Schrieffer (and Bogoliubov-de Gennes) Theory	5
2.1	Bardeen-Cooper-Schrieffer Theory	6
2.2	Bogoliubov-de Gennes Theory	7
2.3	Nambu Basis and Particle-Hole Symmetry	8
2.4	Expectation Value of an Observable	10
2.5	Spin Degrees of Freedom	11
2.6	Translational Invariance	12
3	Superconducting Proximity Effect in Topological Metals	15
3.1	Introduction	16
3.2	Model Hamiltonian for Heterostructure	17
3.3	Distance Dependence of Pair Amplitudes	21
3.4	Majorana Vortex Bound State on the Naked Surface	23
3.5	Conclusions	26
4	Scanning Tunneling Spectroscopy and Quasiparticle Interference	33
4.1	Tunneling of Electron	33
4.2	Quasiparticle Interference	35
5	Identifying the ‘Fingerprint’ of Antiferromagnetic Spin-Fluctuations in Iron-Pnictide Cooper Pairing	39
6	Response to Gauge Field	59
6.1	Peierls Phase	59
6.2	Current and Superfluid Stiffness	60
6.3	Optical Conductivity	62
7	Cold-spots and Glassy Nematicity in Underdoped Cuprates	65
7.1	Introduction	66
7.2	The Model	70
7.3	Method of Solution	72
7.4	Results for the superconducting nematic glass	74
7.5	Other forms of glassy order	81
7.5.1	Superconducting d -form factor CDW glass	81
7.5.2	Optical conductivity for other models of antinodal gap	83
7.6	Conclusion	87

8 Superconductor under Magnetic Field	97
8.1 Magnetic Translation Operator	97
8.2 Two-dimensional Lattice System	100
8.3 Kinetic Energy in Magnetic Field	101
8.4 Bogoliubov Quasiparticles in Magnetic Field	102
8.5 Franz-Tešanović Gauge	104
9 Signatures of Unconventional Pairing in Near-vortex Electronic Structure of LiFeAs	111
9.1 Introduction	112
9.2 Model	114
9.3 Method	117
9.3.1 Non-Self-Consistent Approach	117
9.3.2 Self-Consistent Approach	118
9.4 Results	119
9.4.1 Non-Self-Consistent Approach on Single Band Model	119
9.4.2 Non-Self-Consistent Approach on Five Band Model	123
9.4.3 Self-Consistent Approach	124
9.5 Conclusion	128
A Dynamical Susceptibility at Non-zero Temperature	135
A.1 Linear Response Theory at Non-zero Temperature	135
A.2 Spectral Representation	137

CHAPTER 1

INTRODUCTION

In a material whose physics of interest is controlled by its electronic degrees of freedom, electronic spectra provides crucial information. Compared to other observables such as d.c. conductivity or specific heat, spectroscopic measurements provides energy resolution, making available a rich set of information of the excitations of the system. Especially in the study of unconventional superconductors, spectroscopic probes such as scanning tunneling spectroscopy [1, 2], angle-resolved photoemission spectroscopy [3], as well as optical measurements [4] have played important roles.

To turn experimentally observed spectra into understanding of the physics of the material, a theoretical analysis of the spectra is necessary. For conventional “metallic” superconductors, where mean-field theory with perturbative corrections work wonderfully, theoretical analysis of spectra is rather straightforward. In many unconventional superconductors, however, are strongly correlated materials: Electron-electron interaction or electron-boson interaction is too strong to be ignored or treated perturbatively. Calculation of electronic spectra of such system is non-trivial, with limited success from numerical methods such as quantum Monte Carlo or exact diagonalization.

Heterogeneity also makes calculation of spectra difficult. For translationally invariant systems, momentum conservation greatly reduces the Hilbert space, rendering calculations more approachable. However, when systems lose translational symmetry, where momentum is no longer conserved, the spatial dependence of the Hamiltonian need to be taken into account. Such heterogeneity can arise due to impurities, symmetry breaking order parameter with short-range cor-

relation, vortex formation in type-II superconductors, or artificially designed heterostructures. Although analytical solutions are not easily attainable, numerical methods allow calculation of spectra in such systems possible.

This dissertation is a discussion on theoretical computation of electronic spectra of heterogeneous unconventional superconductors. It consists of previously published papers, each preceded by related theoretical background. The structure is as follows: Chapter 2 is a basic overview of the Bogoliubov-de Gennes theory, followed by a research paper *Superconducting proximity effect in topological metals* in chapter 3. Chapter 4 discusses theoretical calculation of scanning tunneling spectroscopy and quasiparticle interference, followed by a research paper *Identifying the ‘fingerprint’ of antiferromagnetic spin-fluctuations in iron-pnictide cooper pairing* in chapter 5. Chapter 6 discusses gauge field, current, and optical conductivity on a lattice model model. The following chapter 7 is a research paper *Cold-spots and glassy nematicity in underdoped cuprates*. Chapter 8 discusses how to include magnetic field to Bogoliubov-de Gennes theory, followed by a research paper *Signatures of unconventional pairing in near-vortex electronic structure of LiFeAs* in chapter 9.

BIBLIOGRAPHY

1. Fischer, Ø., Kugler, M., Maggio-Aprile, I., Berthod, C. & Renner, C. Scanning tunneling spectroscopy of high-temperature superconductors. *Rev. Mod. Phys.* **79**, 353 (2007).
2. Fujita, K. *et al.* Spectroscopic imaging scanning tunneling microscopy studies of electronic structure in the superconducting and pseudogap phases of cuprate high- T_c superconductors. *J. Phys. Soc. Jpn.* **81**, 011005 (2012).
3. Damascelli, A., Hussain, Z. & Shen, Z.-X. Angle-resolved photoemission studies of the cuprate superconductors. *Rev. Mod. Phys.* **75**, 473 (2003).
4. Basov, D. N. & Timusk, T. Electrodynamics of high- T_c superconductors. *Rev. Mod. Phys.* **77**, 721 (2005).

CHAPTER 2

OVERVIEW ON BARDEEN-COOPER-SCHRIEFFER (AND BOGOLIUBOV-DE GENNES) THEORY

Superconductor is a phase of matter characterized by zero electrical resistivity and the expulsion of magnetic field. It was first discovered by H. Kamerlingh Onnes in 1911. Only after decades an almost complete theoretical picture of superconductivity was developed by Bardeen, Cooper and Schrieffer in the 1950s [1]. In Bardeen-Cooper-Schrieffer (BCS) theory, superconductivity arises as an instability of metallic state with Fermi surface due to effective attractive interaction mediated by phonons. In 1986, however, a new class of “high-temperature” cuprate superconductors was discovered by Bednorz and Müller [2], whose superconductivity does not seem to be explained by phonon-mediation. And then after two decades, another class of iron-based superconductors were discovered by Kamihara *et al.* [3, 4]. The mechanism of superconductivity in these classes of materials is still at large. Much of the phenomenology of the condensed state, nevertheless, seems to be well described by the BCS theory. In studying the spectra of these unconventional superconductors, BCS theory still remains useful.

In this chapter, we present a brief overview of BCS theory. We start from the BCS theory for systems with translational invariance, and then move on to Bogoliubov-de Gennes formalism which can be used to describe heterogeneous superconductors.

2.1 Bardeen-Cooper-Schrieffer Theory

The BCS theory of superconductivity is a Hartree-Fock theory of an interacting Hamiltonian. The *reduced Hamiltonian* which contains the bare essentials for BCS theory is

$$\mathcal{H} = \sum_{\mathbf{k}\sigma} \epsilon_{\mathbf{k}} n_{\mathbf{k}\sigma} + \sum_{\mathbf{k}\mathbf{k}'} V_{\mathbf{k}'\mathbf{k}} b_{\mathbf{k}'}^* b_{\mathbf{k}}, \quad (2.1)$$

where $\epsilon_{\mathbf{k}}$ is the dispersion of the non-interacting electron, $n_{\mathbf{k}\sigma} \equiv c_{\mathbf{k}\sigma}^* c_{\mathbf{k}\sigma}$ the number of electrons with momentum \mathbf{k} and spin σ , with $c_{\mathbf{k}\sigma}^*$ creating an electron with (crystal) momentum \mathbf{k} and spin σ . Here we use $*$ to indicate operator conjugation, reserving \dagger to operator conjugation together with matrix Hermitian conjugate.

$V_{\mathbf{k}'\mathbf{k}}$ is the (effective) attractive interaction, which can be written in terms of *pairons* $b_{\mathbf{k}}^* \equiv c_{\mathbf{k}\uparrow}^* c_{-\mathbf{k}\downarrow}^*$. The crux of BCS theory lies in the mean-field decomposition of the interaction in the “anomalous” channel. By making the following mean-field approximation to the commutator

$$[c_{\mathbf{p}\uparrow}, \mathcal{H}] = \epsilon_{\mathbf{p}} c_{\mathbf{p}\uparrow} + \sum_{\mathbf{k}\mathbf{p}} V_{\mathbf{k}'\mathbf{p}} b_{\mathbf{k}} c_{-\mathbf{p}\downarrow}^* \approx \epsilon_{\mathbf{p}} c_{\mathbf{p}\uparrow} + \Delta_{\mathbf{p}} c_{-\mathbf{p}\downarrow}^* \equiv [c_{\mathbf{p}\uparrow}, \mathcal{H}_{\text{BCS}}] \quad (2.2)$$

such that the right hand side is linear in terms of c and c^* , we arrive at the BCS Hamiltonian

$$\mathcal{H}_{\text{BCS}} = \sum_{\mathbf{k}\sigma} \epsilon_{\mathbf{k}} n_{\mathbf{k}\sigma} + \sum_{\mathbf{k}} \Delta_{\mathbf{k}} c_{\mathbf{k}\uparrow}^* c_{-\mathbf{k}\downarrow}^* + \Delta_{\mathbf{k}}^* c_{-\mathbf{k}\downarrow} c_{\mathbf{k}\uparrow}. \quad (2.3)$$

The above Hamiltonian, together with the self-consistency equation

$$\Delta_{\mathbf{p}} = \sum_{\mathbf{k}} V_{\mathbf{p}\mathbf{k}} \langle c_{-\mathbf{k}\downarrow} c_{\mathbf{k}\uparrow} \rangle \quad (2.4)$$

describes the ground state of a superconductor.

2.2 Bogoliubov-de Gennes Theory

The original BCS theory presented in momentum basis for translationally invariant systems was later generalized to Bogoliubov-de Gennes formalism [5], which is formalized in real-space basis to describe heterogeneous superconductors. In this section, we present a general formalism which incorporates all variants of Bogoliubov-de Gennes theory used in later chapters (spin-singlet, spin-orbit coupled system, magnetic field, etc.).

Let me again begin with a generic interacting Hamiltonian

$$\mathcal{H} = \mathcal{K} + \mathcal{V} = \sum_{\alpha\beta} K_{\alpha\beta} c_{\alpha}^{*} c_{\beta} + \frac{1}{4} \sum_{\alpha\beta\mu\nu} V_{\alpha\beta;\mu\nu} c_{\alpha}^{*} c_{\beta}^{*} c_{\nu} c_{\mu}, \quad (2.5)$$

where the Greek subscripts represent all degrees of freedom of the fermionic Hilbert space (e.g., site indices for spinless fermions, or multi-indices representing spin and site for spinful fermions). Hermiticity of the Hamiltonian requires that

$$\mathcal{K} = \mathcal{K}^{\dagger} \Leftrightarrow K_{\alpha\beta} c_{\alpha}^{*} c_{\beta} = K_{\alpha\beta}^{*} c_{\beta}^{*} c_{\alpha} \Leftrightarrow K_{\alpha\beta} = K_{\beta\alpha}^{*}, \quad (2.6)$$

$$\mathcal{V} = \mathcal{V}^{\dagger} \Leftrightarrow V_{\alpha\beta;\mu\nu} c_{\alpha}^{*} c_{\beta}^{*} c_{\nu} c_{\mu} = V_{\alpha\beta;\mu\nu}^{*} c_{\mu}^{*} c_{\nu}^{*} c_{\beta} c_{\alpha} \Leftrightarrow V_{\alpha\beta;\mu\nu} = V_{\mu\nu;\alpha\beta}^{*}. \quad (2.7)$$

The mean-field decomposition of this Hamiltonian in the BCS channel writes

$$\mathcal{V}_{\text{HF}} = \frac{1}{4} \sum_{\alpha\beta\mu\nu} V_{\alpha\beta;\mu\nu} \left(F_{\alpha\beta}^{*} c_{\nu} c_{\mu} + F_{\mu\nu} c_{\alpha}^{*} c_{\beta}^{*} \right) \quad (2.8)$$

where $F_{\alpha\beta} \equiv \langle c_{\beta} c_{\alpha} \rangle$ is the pair amplitude on bond (α, β) . In terms of the “gap” order parameter defined as

$$\Delta_{\alpha\beta} \equiv \frac{1}{2} \sum_{\mu\nu} V_{\alpha\beta;\mu\nu} F_{\mu\nu}, \quad (2.9)$$

the Hartree-Fock term writes

$$\mathcal{V}_{\text{HF}} = \frac{1}{2} \sum_{\alpha\beta} \Delta_{\alpha\beta} c_{\alpha}^{*} c_{\beta}^{*} + \frac{1}{2} \sum_{\mu\nu} \Delta_{\mu\nu}^{*} c_{\nu} c_{\mu}. \quad (2.10)$$

The resulting Hamiltonian is then

$$\mathcal{H}_{\text{BdG}} = \sum_{\alpha\beta} \left[K_{\alpha\beta} c_{\alpha}^{*} c_{\beta} + \frac{1}{2} \Delta_{\alpha\beta} c_{\alpha}^{*} c_{\beta}^{*} + \frac{1}{2} \Delta_{\alpha\beta}^{*} c_{\beta} c_{\alpha} \right]. \quad (2.11)$$

2.3 Nambu Basis and Particle-Hole Symmetry

Up to constant terms, \mathcal{H}_{BdG} can be rewritten as

$$\mathcal{H}_{\text{BdG}} = \sum_{\alpha\beta} \frac{1}{2} K_{\alpha\beta} c_{\alpha}^{*} c_{\beta} - \frac{1}{2} K_{\beta\alpha} c_{\alpha} c_{\beta}^{*} + \frac{1}{2} \Delta_{\alpha\beta} c_{\alpha}^{*} c_{\beta}^{*} + \frac{1}{2} \Delta_{\alpha\beta}^{*} c_{\beta} c_{\alpha} \quad (2.12)$$

which can be presented in the matrix form by defining a “Nambu” spinor $\psi_{\alpha}^{\dagger} = (c_{\alpha}^{*}, c_{\alpha})$:

$$\mathcal{H}_{\text{BdG}} = \frac{1}{2} \sum_{\alpha\beta} \begin{pmatrix} c_{\alpha}^{*} & c_{\alpha} \end{pmatrix} \begin{pmatrix} K_{\alpha\beta} & \Delta_{\alpha\beta} \\ \Delta_{\beta\alpha}^{*} & -K_{\alpha\beta}^{*} \end{pmatrix} \begin{pmatrix} c_{\beta} \\ c_{\beta}^{*} \end{pmatrix} = \frac{1}{2} \sum_{\alpha\beta} \psi_{\alpha}^{\dagger} H_{\alpha\beta} \psi_{\beta}. \quad (2.13)$$

Fermion anticommutation requires that Δ be antisymmetric, i.e. $\Delta_{\alpha\beta} = -\Delta_{\beta\alpha}$.

Note that the spinor ψ_{α} counts the (complex) fermionic degrees of freedom twice; i.e., it satisfies the *Majorana condition*

$$\psi_{\alpha}^{*} = \tau_1 \psi_{\alpha} \equiv C \psi_{\alpha}, \quad (2.14)$$

where $C = \tau_1$ can be interpreted as the *charge conjugation operator*.¹

Due to the Majorana condition of ψ , the Hamiltonian \mathcal{H}_{BdG} enjoys particle-hole symmetry. For example, the BdG Hamiltonian is written

$$\mathcal{H}_{\text{BdG}} = \frac{1}{2} \begin{pmatrix} c^{\dagger} & c^T \end{pmatrix} \begin{pmatrix} K & \Delta \\ -\Delta^{*} & -K^{*} \end{pmatrix} \begin{pmatrix} c \\ c^{*} \end{pmatrix} = \frac{1}{2} \psi^{\dagger} H \psi. \quad (2.15)$$

¹For discussions on the Majorana spinor and the Majorana condition, see e.g. Ref. [6].

From here on, we suppress the subscripts when the symbols represent matrices and vectors. Under charge conjugation $\psi = C^\dagger \psi^*$, the Hamiltonian writes

$$\mathcal{H}_{\text{BdG}} = \frac{1}{2} \psi^T C H C^\dagger \psi^* = -\frac{1}{2} \psi^\dagger (C H C^\dagger)^T \psi = \frac{1}{2} \psi^\dagger H \psi. \quad (2.16)$$

From this the “particle-hole” symmetry for the single-particle Hamiltonian writes

$$C H C^\dagger = -H^T = -H^*. \quad (2.17)$$

The second equality follows from Hermiticity of H . This particle-hole symmetry ensures that, if Ψ is an eigenvector of H with eigenvalue e , then $C^\dagger \Psi^*$ is also an eigenvector with eigenvalue $-e$ (e is real since H is Hermitian):

$$H(C^\dagger \Psi^*) = -C^\dagger H^* \Psi^* = -C^\dagger (e \Psi)^* = -e(C^\dagger \Psi^*). \quad (2.18)$$

After diagonalizing the matrix $H = U E U^\dagger$, with a unitary matrix U and a diagonal matrix E , particle-hole symmetry guarantees that the matrix can be organized in the following form

$$E = \begin{pmatrix} E_+ & 0 \\ 0 & -E_+ \end{pmatrix}, \quad \text{with} \quad U = \begin{pmatrix} u & v^* \\ v & u^* \end{pmatrix} \quad (2.19)$$

where E_+ is a diagonal matrix with non-negative entries. We can now define a new fermion spinor $\tilde{\psi}$ as follows:

$$\tilde{\psi} \equiv \begin{pmatrix} f \\ f^* \end{pmatrix} \equiv U^\dagger \psi = \begin{pmatrix} u^\dagger c + v^T c^* \\ v^\dagger c + u^T c^* \end{pmatrix}. \quad (2.20)$$

which satisfies Fermion anticommutation $\{\tilde{\psi}_\alpha, \tilde{\psi}_\beta^*\} = \delta_{\alpha\beta}$. Then \mathcal{H}_{BdG} can be written in terms of a diagonal matrix

$$\mathcal{H}_{\text{BdG}} = \frac{1}{2} \begin{pmatrix} f^\dagger & f^T \end{pmatrix} \begin{pmatrix} E_+ & 0 \\ 0 & -E_+ \end{pmatrix} \begin{pmatrix} f \\ f^* \end{pmatrix} = f^\dagger E_+ f \quad (2.21)$$

Observe that the Hamiltonian is written in terms of non-negative energy modes. An excitation created by f^\dagger is called a *Bogoliubov quasiparticle*.

2.4 Expectation Value of an Observable

If all of E_+ are positive (i.e. no zero eigenvalues), then the system has a unique ground state defined as the *vacuum of excitation* f

$$f|\Omega\rangle_{\mathcal{H}_{\text{BdG}}}=0, \quad (2.22)$$

whereas if there are n zero eigenvalues (n needs to be even), the system has ground state degeneracy of $2^{n/2}$.

To compute an expectation value of an observable for the ground state, it is convenient to define the following equal time Green's function

$$G \equiv \langle \psi \psi^\dagger \rangle = \begin{pmatrix} \langle cc^\dagger \rangle & \langle cc^T \rangle \\ \langle c^* c^\dagger \rangle & \langle c^* c^T \rangle \end{pmatrix}. \quad (2.23)$$

Ground state expectation value (that is, “vacuum expectation value” with respect to excitation f) of any static operator quadratic in the fermion operator c and c^* can be written in terms of this correlator. For example, the fermion density at the coordinate α is $n_\alpha = \langle c_\alpha^* c_\alpha \rangle = G_{\alpha\alpha}^{11}$. Using U from previous section, we have, for the ground state,

$$\begin{aligned} G &\equiv \langle \psi \psi^\dagger \rangle = \begin{pmatrix} \langle cc^\dagger \rangle & \langle cc^T \rangle \\ \langle c^* c^\dagger \rangle & \langle c^* c^T \rangle \end{pmatrix} \\ &= \langle U^\dagger \tilde{\psi} \tilde{\psi}^\dagger U \rangle = \begin{pmatrix} u & v^* \\ v & u^* \end{pmatrix} \begin{pmatrix} \langle ff^\dagger \rangle & \langle ff^T \rangle \\ \langle f^* f^\dagger \rangle & \langle f^* f^T \rangle \end{pmatrix} \begin{pmatrix} u^\dagger & v^\dagger \\ v^T & u^T \end{pmatrix}. \end{aligned} \quad (2.24)$$

At temperature $T = 1/\beta$, the occupation number of Bogoliubov quasiparticle follows Fermi-Dirac distribution

$$\begin{pmatrix} \langle ff^\dagger \rangle & \langle ff^T \rangle \\ \langle f^* f^\dagger \rangle & \langle f^* f^T \rangle \end{pmatrix} = \begin{pmatrix} f_D(-E_+) & 0 \\ 0 & f_D(E_+) \end{pmatrix}, \quad (2.25)$$

where $f_D(E) = (1 + e^{\beta E})^{-1}$ is Fermi function. Therefore

$$G = \begin{pmatrix} u f_D(-E_+) u^\dagger + v^* f_D(E_+) v^T & u f_D(-E_+) v^\dagger + v^* f_D(E_+) u^T \\ v f_D(-E_+) u^\dagger + u^* f_D(E_+) v^T & v f_D(-E_+) v^\dagger + u^* f_D(E_+) u^T \end{pmatrix}. \quad (2.26)$$

2.5 Spin Degrees of Freedom

Electrons have spin one-half. To incorporate spin degrees of freedom into the Hamiltonian, the subscript α can be considered a multi-index with $\sigma = \uparrow, \downarrow$ spin and i all the remaining (site, orbital, etc.) degrees of freedom. Explicitly writing out the spin indices, the Hamiltonian can be written as

$$\begin{pmatrix} K_{\uparrow\uparrow} & K_{\uparrow\downarrow} & \Delta_{\uparrow\uparrow} & \Delta_{\uparrow\downarrow} \\ K_{\uparrow\downarrow}^\dagger & K_{\downarrow\downarrow} & -\Delta_{\uparrow\downarrow}^T & \Delta_{\downarrow\downarrow} \\ -\Delta_{\uparrow\uparrow}^* & -\Delta_{\uparrow\downarrow}^* & -K_{\uparrow\uparrow}^* & -K_{\uparrow\downarrow}^* \\ \Delta_{\uparrow\downarrow}^\dagger & -\Delta_{\downarrow\downarrow}^* & -K_{\downarrow\downarrow}^T & -K_{\uparrow\downarrow}^* \end{pmatrix}. \quad (2.27)$$

The gap order parameter Δ can be decomposed into spin-singlet and spin-triplet channels. For spin-singlet, $\Delta_{\uparrow\uparrow} = \Delta_{\downarrow\downarrow} = 0$ and $\Delta_{\uparrow\downarrow} = \Delta_{\downarrow\uparrow}^T$, while for spin-triplet, all $\Delta_{\sigma\sigma'}$ are antisymmetric: $\Delta_{\uparrow\uparrow} = -\Delta_{\uparrow\uparrow}^T$, $\Delta_{\downarrow\downarrow} = -\Delta_{\downarrow\downarrow}^T$, and $\Delta_{\uparrow\downarrow} = -\Delta_{\downarrow\uparrow}^T$. These can be organized in the following form

$$\Delta = (\Psi + \mathbf{d} \cdot \boldsymbol{\sigma}) i \sigma_2 \quad (2.28)$$

where Ψ is a symmetric matrix representing spin-singlet channel, while the “d-vector” \mathbf{d} is a collection of antisymmetric matrices representing pairing in spin-triplet channel.

2.6 Translational Invariance

In a solid state system, discrete lattice translation is often a good symmetry. Making use of this symmetry greatly simplifies the problem. For this, let us consider a D -dimensional lattice system whose lattice vectors are $\{\mathbf{a}_i\}_{i=1\dots D}$ with a periodic boundary condition $N_i \mathbf{a}_i \equiv \mathbf{0}$ for all $i \dots D$. A fermion annihilation operator for such a system can be indexed by the position of the lattice site \mathbf{x} (on Bravais lattice), and the rest α (which can include spin, orbital, etc.):

$$\mathcal{H}_{\text{BdG}} = \frac{1}{2} \sum_{\mathbf{xy}\alpha\beta} \begin{pmatrix} c_{\mathbf{x}\alpha}^* & c_{\mathbf{x}\alpha} \end{pmatrix} \begin{pmatrix} K_{\mathbf{x}\alpha;\mathbf{y}\beta} & \Delta_{\mathbf{x}\alpha;\mathbf{y}\beta} \\ -\Delta_{\mathbf{x}\alpha;\mathbf{y}\beta}^* & -K_{\mathbf{x}\alpha;\mathbf{y}\beta}^* \end{pmatrix} \begin{pmatrix} c_{\mathbf{y}\beta} \\ c_{\mathbf{y}\beta}^* \end{pmatrix}. \quad (2.29)$$

Translation symmetry of the Hamiltonian requires that $K_{\mathbf{x}\alpha;\mathbf{y}\beta} = K_{\alpha\beta}(\mathbf{x} - \mathbf{y})$. The condition for $\Delta_{\mathbf{x}\alpha;\mathbf{y}\beta}$ is less constraining because of gauge redundancy. Here, for simplicity, we assume $\Delta_{\mathbf{x}\alpha;\mathbf{y}\beta} = \Delta_{\alpha\beta}(\mathbf{x} - \mathbf{y})$, which corresponds to the Cooper pairs having zero crystal momentum. It is, nevertheless, possible to have translation symmetry with non-zero pair momentum, if the pair momentum lies at a high symmetry point of the Brillouin zone.

To make use of the translation symmetry, it is convenient to write the Hamiltonian in terms of the following crystal momentum basis.

$$c_{\mathbf{k}\sigma} = \frac{1}{\sqrt{N}} \sum_{\mathbf{x}} e^{-i\mathbf{k}\cdot\mathbf{x}} c_{\mathbf{x}\sigma} \quad c_{\mathbf{k}\sigma}^* = \frac{1}{\sqrt{N}} \sum_{\mathbf{x}} e^{i\mathbf{k}\cdot\mathbf{x}} c_{\mathbf{x}\sigma}^* \quad (2.30)$$

for $\mathbf{k} = \sum_{i=1}^D \frac{n_i}{N_i} \mathbf{G}_i$, with $n_i = 0, 1, \dots, N_i - 1$ and $N = \prod N_i$. \mathbf{G}_i is a reciprocal lattice vector defined by

$$\mathbf{G}_i \cdot \mathbf{a}_j = 2\pi\delta_{ij}. \quad (2.31)$$

In this basis, the Hamiltonian can be written in terms of Nambu spinor $\psi_{\mathbf{k}\alpha}^\dagger =$

$(c_{\mathbf{k}\alpha}^*, c_{-\mathbf{k}\alpha})$ as

$$\mathcal{H}_{\text{BdG}} = \frac{1}{2} \sum_{\mathbf{k}\alpha\beta} \begin{pmatrix} c_{\mathbf{k}\alpha}^* & c_{-\mathbf{k}\alpha} \end{pmatrix} \begin{pmatrix} K_{\mathbf{k},\alpha\beta} & \Delta_{\mathbf{k},\alpha\beta} \\ -\Delta_{-\mathbf{k},\alpha\beta}^* & -K_{-\mathbf{k},\alpha\beta}^* \end{pmatrix} \begin{pmatrix} c_{\mathbf{k}\beta} \\ c_{-\mathbf{k}\beta}^* \end{pmatrix} = \frac{1}{2} \sum_{\mathbf{k}\alpha\beta} \psi_{\mathbf{k}}^\dagger H_{\mathbf{k}} \psi_{\mathbf{k}} \quad (2.32)$$

where

$$K_{\mathbf{k},\alpha\beta} = \frac{1}{N} \sum_{\mathbf{r}} e^{-i\mathbf{k}\cdot\mathbf{r}} K_{\alpha\beta}(\mathbf{r}), \quad \Delta_{\mathbf{k},\alpha\beta} = \frac{1}{N} \sum_{\mathbf{r}} e^{-i\mathbf{k}\cdot\mathbf{r}} \Delta_{\alpha\beta}(\mathbf{r}). \quad (2.33)$$

The self-consistency equation also simplifies in terms of momentum states. To see this, let us consider the following form of interaction

$$\mathcal{V} = \frac{1}{4} \sum_{\mathbf{x}\mathbf{r}} \sum_{\alpha\beta\gamma\delta} V_{\alpha\beta\gamma\delta}(\mathbf{r}) c_{\mathbf{x}+\mathbf{r},\alpha}^* c_{\mathbf{x},\beta}^* c_{\mathbf{x},\delta} c_{\mathbf{x}+\mathbf{r},\gamma}, \quad (2.34)$$

which is translationally invariant, and conserves local charge density. Typical density-density or spin-spin interactions can be written in this form. Again, in the momentum basis,

$$\mathcal{V} = \frac{1}{4} \sum V_{\alpha\beta\gamma\delta}(\mathbf{q}) c_{\mathbf{k}_1-\mathbf{q},\alpha}^* c_{\mathbf{k}_2+\mathbf{q},\beta}^* c_{\mathbf{k}_2,\delta} c_{\mathbf{k}_1,\gamma} \quad (2.35)$$

Making use of the translation invariance of the Ansatz $\langle c_{\mathbf{x}\alpha} c_{\mathbf{y}\beta} \rangle = F_{\alpha\beta}(\mathbf{x}-\mathbf{y})$, the pair amplitude in momentum space is

$$\langle c_{\mathbf{k}\alpha} c_{\mathbf{p}\beta} \rangle = \langle c_{\mathbf{k}\alpha} c_{-\mathbf{k}\beta} \rangle \delta_{\mathbf{k},-\mathbf{p}}. \quad (2.36)$$

This implies that the interaction term relevant for pairing is

$$\mathcal{V}_{\text{red}} = \frac{1}{4} \sum V_{\alpha\beta\gamma\delta}(\mathbf{q}) c_{-\mathbf{k}-\mathbf{q},\alpha}^* c_{\mathbf{k}+\mathbf{q},\beta}^* c_{\mathbf{k},\delta} c_{-\mathbf{k},\gamma}, \quad (2.37)$$

and the self-consistency equation becomes

$$\Delta_{\alpha\beta}(\mathbf{k}) = -\frac{1}{2} \sum_{\gamma\delta} V_{\alpha\beta\gamma\delta}(\mathbf{q}) \langle c_{\mathbf{k}+\mathbf{q},\delta} c_{-\mathbf{k}-\mathbf{q},\gamma} \rangle. \quad (2.38)$$

BIBLIOGRAPHY

1. Tinkham, M. *Introduction to superconductivity* Second Edition (Dover Publications, 2004).
2. Bednorz, J. G. & Müller, K. A. Possible high T_c superconductivity in the Ba-La-Cu-O system. *Z. Phys. B: Condens. Matt.* **64**, 189 (1986).
3. Kamihara, Y. *et al.* Iron-based layered superconductor: LaOFeP. *J. Amer. Chem. Soc.* **128**, 10012 (2006).
4. Kamihara, Y., Watanabe, T., Hirano, M. & Hosono, H. Iron-based layered superconductor $\text{La}[\text{O}_{1-x}\text{F}_x]\text{FeAs}$ ($x = 0.05 - 0.12$) with $T_c = 26\text{ K}$. *J. Amer. Chem. Soc.* **130**, 3296 (2008).
5. de Gennes, P. G. *Superconductivity of metals and alloys* chap. 5 (Addison-Wesley, 1989).
6. Srednicki, M. *Quantum field theory* (Cambridge University Press, 2007).

CHAPTER 3

RESEARCH PAPER:

SUPERCONDUCTING PROXIMITY EFFECT IN TOPOLOGICAL METALS

Kyunghmin Lee¹, Abolhassan Vaezi¹, Mark H. Fischer^{1,2}, and Eun-Ah Kim¹

¹*Department of Physics, Cornell University, Ithaca, New York 14853, USA.*

²*Department of Condensed Matter Physics, Weizmann Institute of Science, Rehovot 76100, Israel.*

Published on Physical Review B **90**, 214510 (2014).

Abstract

Much interest in the superconducting proximity effect in three-dimensional (3D) topological insulators (TIs) has been driven by the potential to induce Majorana bound states at the interface. Most candidate materials for 3D TI, however, are bulk metals, with bulk states at the Fermi level coexisting with well-defined surface states exhibiting spin-momentum locking. In such topological metals, the proximity effect can differ qualitatively from that in TIs. By studying a model topological metal-superconductor (TM-SC) heterostructure within the Bogoliubov-de Gennes formalism, we show that the pair amplitude reaches the naked surface, unlike in a topological insulator-superconductor (TI-SC) heterostructure where it is confined to the interface. Furthermore, we predict vortex-bound-state spectra to contain a Majorana zero-mode localized at the naked surface, separated from the bulk vortex-bound-state spectra by a finite energy gap in such a TM-SC heterostructure. These naked-surface-bound modes are amenable to experimental observation and manipulation, presenting advantages of TM-SC over TI-SC.

3.1 Introduction

The potential realization of Majorana zero modes (MZMs) at the ends of a nanowire-superconductor hybrid system [1–6] has attracted broad interest to different ways of stabilizing MZMs. While there are proposals to exploit exotic statistics of MZMs within quasi-one-dimensional networks [7–10], a two dimensional setting would be desirable for observing statistical properties of MZMs. A MZM can appear as a vortex bound state of triplet superfluids [11] or superconductors [12]. Unfortunately, naturally occurring triplet superconductors are rare, and hence the proposal by Fu and Kane [13] to use the superconducting proximity effect on the topological insulator (TI) surface states raised enthusiasm as an alternative route to realizing MZMs hosted in a two dimensional space. However, most known three-dimensional (3D) TI candidate materials, such as Bi_2Se_3 and Bi_2Te_3 , have both the surface states and the bulk states at the Fermi energy [14]. Recent experimental successes in inducing superconductivity in Bi_2Se_3 thin films through proximity effect [15, 16] makes it all the more urgent to address the superconducting proximity effect in such topological *metals*, where surface states and bulk states coexist.

In the proposal by Fu and Kane [13] for realizing MZMs, superconductivity is induced to the surface states of a 3D TI by proximity to a trivial *s*-wave superconductor (SC). The argument for the existence of a MZM as a vortex bound state is based on the formal equivalence between a $p + ip$ superconducting gap of a spinless fermion and a trivial *s*-wave gap after projection to the space of surface states. However, with only the surface states available at the Fermi energy, the superconducting proximity effect is limited to the interface between the TI and the adjacent superconductor. On the other hand when the bulk band crosses the Fermi energy,

as they do in many 3D TI materials, there is a chance that the proximity effect can reach the naked surface. The key questions then would be (1) when can proximity effect reach the naked surface and (2) whether the naked surface can host MZMs. These questions are the focus of this paper.

3.2 Model Hamiltonian for Heterostructure

To be concrete, we consider a Bi_2Se_3 -SC heterostructure, where the Bi_2Se_3 takes the form of a finite thickness slab, so that we can study its naked surface (Fig. 3.1a). We first study how the proximity effect propagates differently depending on the location of the chemical potential, by solving the Bogoliubov-de Gennes (BdG) equation in the heterostructure. We then study the vortex bound state spectra with the gap structure inferred from the solution and investigate the stability of a MZM on the naked surface depending on chemical potential.

The heterostructure of interest consists of a slab of Bi_2Se_3 for $0 < z < L_{\text{TI}}$ and superconductor for $-L_{\text{SC}} < z < 0$. The electronic structure of Bi_2Se_3 is described by an effective two-orbital Hamiltonian on a simple cubic lattice with lattice constant a . Given the slab geometry with periodic boundary conditions in the x and y directions, we choose as basis $|\mathbf{k}, z, \alpha, s\rangle$, a state with momentum $\mathbf{k} = (k_x, k_y)$ within an xy plane at $z = (n_z + 1/2)a$ for $n_z = 0 \dots N_{\text{TI}} - 1$, with orbital α and spin s . As the normal-state Hamiltonian of the model we take a lattice version of the four-band continuum model for 3D TI as given in Ref. [17] consisting of two parts: intra-layer terms $\hat{H}_{\mathbf{k}}^0$ and the inter-layer hopping (from n_z to $n_z + 1$) terms $\hat{H}_{\mathbf{k}}^{(1)}$

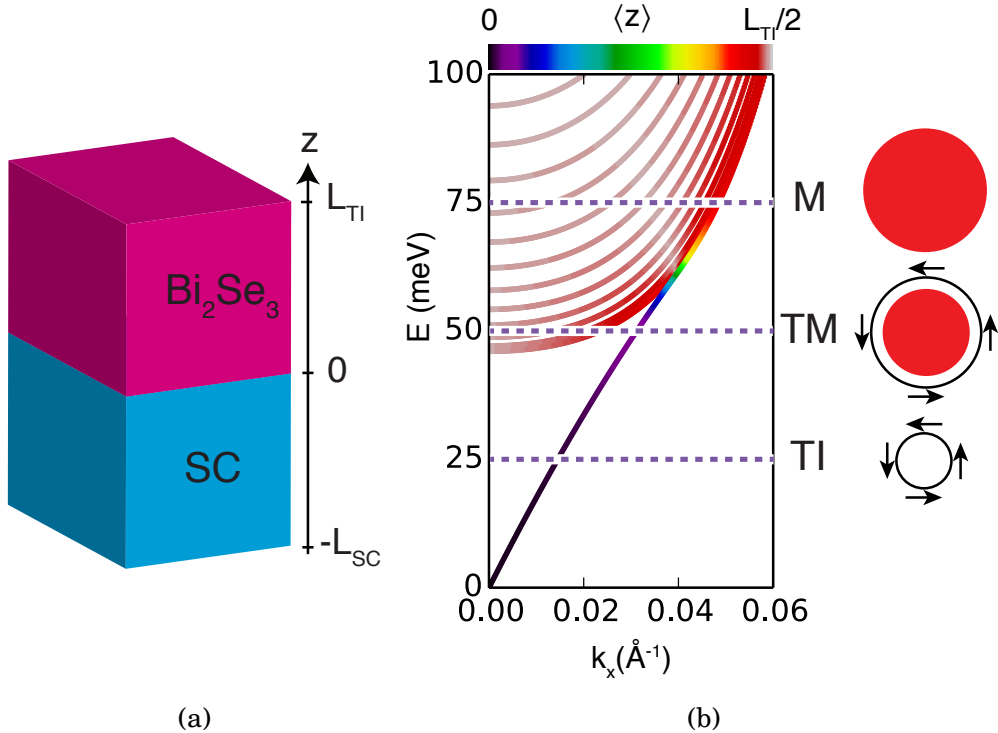


Figure 3.1: (a) Bi_2Se_3 -SC heterostructure considered in this paper. (b) Dispersion of Bi_2Se_3 on a slab of finite thickness L_{TI} . Each point is doubly degenerate, and the color scale indicates the minimum $z_{\min} = \min_{\Psi} \langle z \rangle_{\Psi}$ that can be obtained within the degenerate space $\Psi \in \text{span}\{\Psi_1, \Psi_2\}$. The dotted horizontal lines indicate representative chemical potentials associated with TI, TM, and M regimes as defined in the text. We present schematics of corresponding Fermi surfaces next to each dotted line, where red filled circles represent the bulk states and the black circles the surface states. Each arrow points along the direction of the spin of the surface state on one of the surfaces, which is locked to the momentum.

written as

$$\begin{aligned}
 \hat{H}_{\mathbf{k}}^{(0)} = & t_0 - \mu - 2t_1 \cos(k_x a) - 2t_1 \cos(k_y a) \\
 & + \left[m_0 - 2m_1 \cos(k_x a) - 2m_1 \cos(k_y a) \right] \hat{\tau}_z \\
 & + \lambda \sin(k_y a) \hat{\tau}_x \hat{\sigma}_x - \lambda \sin(k_x a) \hat{\tau}_x \hat{\sigma}_y \\
 \hat{H}_{\mathbf{k}}^{(1)} = & -t_2 - m_2 \hat{\tau}_z - i \frac{\lambda'}{2} \hat{\tau}_y
 \end{aligned} \tag{3.1}$$

where $\hat{\tau}_i(\hat{\sigma}_i)$ for $i = x, y, z$ are Pauli matrices in the orbital (spin) space. The pa-

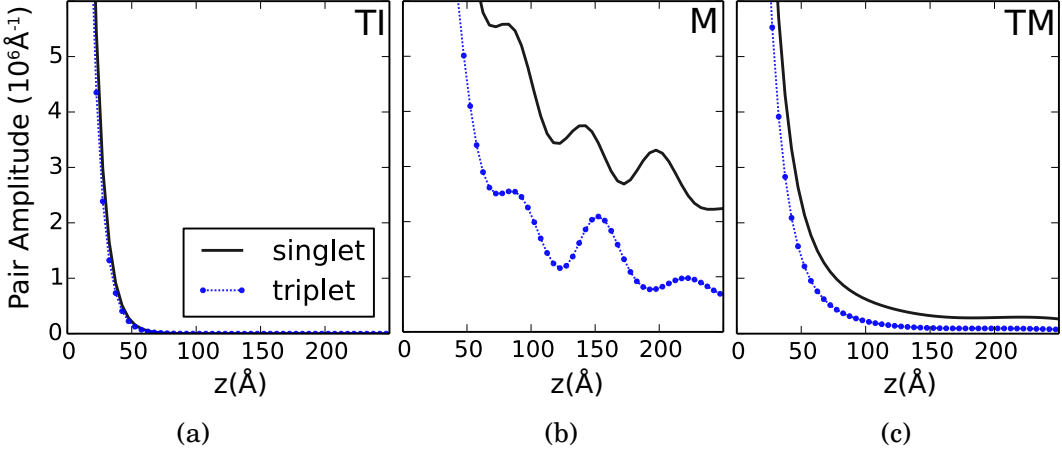


Figure 3.2: The pair amplitudes in singlet and triplet channels as a function of the distance from the interface boundary (z) in three regimes: (a) TI, (b) M, and (c) TM, with chemical potentials $\mu_{\text{TI}} = 25 \text{ meV}$, $\mu_{\text{M}} = 75 \text{ meV}$, and $\mu_{\text{TM}} = 50 \text{ meV}$, respectively. The parameters used in the calculation are $L_{\text{TI}} = 500 \text{ \AA}$, $L_{\text{SC}} = 250 \text{ \AA}$, $a = 5 \text{ \AA}$, $\Delta_0 = 5 \text{ meV}$, $\mu_{\text{SC}} = 300 \text{ meV}$, and with k points on a 100×100 grid. (One quintuple layer is roughly 10 \AA .)

rameters of the Hamiltonian in Eq. (3.1) are chosen such that the model matches the continuum model for Bi_2Se_3 from Ref. [17] up to $O(k^2)$ for $a = 5 \text{ \AA}$: $t_1 = 1.216 \text{ eV}$, $t_2 = 0.230 \text{ eV}$, $m_0 = 7.389 \text{ eV}$, $m_1 = 1.780 \text{ eV}$, $m_2 = 0.274 \text{ eV}$, $\lambda = 0.666 \text{ eV}$, and $\lambda' = 0.452 \text{ eV}$. The reference chemical potential $t_0 = 5.089 \text{ eV}$ has been chosen such that the degeneracy point of the surface state branch lies at $E = 0$ when $\mu = 0$.

To explicitly define what we mean by a topological metal (TM) it is important to recall the well-known band structure of the above model. As shown in Fig. 3.1b, the spectrum of the Hamiltonian contains a (degenerate) gapless branch in addition to the bulk states separated by a finite gap. Depending on the chemical potential, we now define three regimes: topological insulator (TI), TM, and metal (M). The TI is a bulk insulating state with the chemical potential within the bulk band gap (Fig. 3.1b, $\mu = 25 \text{ meV}$). In the TI regime, gapless states at the Fermi level are highly localized at the two surfaces of the slab. On the other hand, when

the chemical potential is well within the bulk conduction band, all the states at the Fermi level, including the ones from the branch that contains surface states in the TI regime, are extended over the entire slab (Fig. 3.1b, $\mu = 75\text{meV}$). Here, we refer to this regime as metal (M). In between these two regimes, there is a range of chemical potential where the branch that is an extension of the Dirac cone coexists with the bulk states at the Fermi level, but nevertheless it remains surface-localized and spin-momentum locked (Fig. 3.1b, $\mu = 50\text{meV}$). Experimentally, this regime can be identified through the spin-momentum locking of Dirac-cone states outside the bulk band-gap, which has been observed in Bi_2Se_3 by spin-angle-resolved photoemission spectroscopy (ARPES) [18]. We refer to this regime as topological metal [19–23]. Note that while the existence of the in-gap surface states is protected by topology, its dispersion depends on material specific details. Therefore, the exact ranges of chemical potential of the three regimes will also be material dependent. Nevertheless, the surface states and the bulk states have qualitatively different contributions to the proximity effect as we will see below, and therefore we expect the three regimes in a real material to show qualitatively the same features as the corresponding regimes in our calculation.

For the superconductor part ($z < 0$) we again use a two-orbital model of the same form as Eq. (3.1) to describe its normal state, with $z = (n_z + 1/2)a$ for $n_z = -N_{\text{SC}}, \dots, -1$. The same parameters as Bi_2Se_3 are used, except that we flip the sign of the “mass term” ($m_0 - 4m_1 - 2m_2$) and make the resulting band structure trivial, by choosing $m_0 = 7.949\text{ eV}$. Also, since the inter-layer hopping in both parts of the heterostructure is described by the same term $\hat{H}_{\mathbf{k}}^{(1)}$, we use it to describe the tunneling between the two parts.

3.3 Distance Dependence of Pair Amplitudes

In order to compare the proximity effect in the three regimes, we impose an orbital-independent s -wave superconducting gap of strength Δ_0 on the superconductor ($z < 0$) and diagonalize the BdG Hamiltonian. We then study how the resulting pair amplitude depends on the distance from the interface. Because the pair amplitude is a matrix in both the spin and the orbital basis, it is convenient to look at its projection onto different spin channels. As pointed out in Ref. [24], spin-singlet A_{1g} pairing term induces spin-singlet A_{1g} and spin-triplet A_{2u} components of the pair amplitude matrix in the presence of spin-orbit coupling of the form Eq. (3.1). The spin singlet and triplet components $\hat{F}^s(z)$ and $\hat{F}^t(z)$ are themselves 2×2 matrices in the orbital space, given by

$$\hat{F}_{\alpha\beta}^{s/t}(z) = \frac{1}{N} \sum_{\mathbf{k}s_1s_2} [\hat{S}_{\mathbf{k}}^{s/t} \cdot i\hat{\sigma}_y]_{s_1s_2} u_{\mathbf{k}zas_1} v_{\mathbf{k}z\beta s_2}^*, \quad (3.2)$$

where N is the number of k points in the xy -plane and the sum is over every positive-energy BdG eigenstate $(u_{\mathbf{k}zas}, v_{\mathbf{k}zas})$. In Eq. (3.2) $\hat{S}_{\mathbf{k}}^s$ and $\hat{S}_{\mathbf{k}}^t$ are the respective form factors for spin-singlet and triplet defined by

$$\hat{S}_{\mathbf{k}}^s = \hat{\sigma}_0, \quad (3.3)$$

$$\hat{S}_{\mathbf{k}}^t = \frac{\sin(k_y a)\hat{\sigma}_x - \sin(k_x a)\hat{\sigma}_y}{\sqrt{\sin^2(k_x a) + \sin^2(k_y a)}}, \quad (3.4)$$

with $\hat{\sigma}_0$ the (2×2) identity matrix. In the self-consistent approach with attractive interaction U in the BCS channel, the superconducting gap Δ is proportional to the pair amplitude ($\Delta \sim UF$). Here, however, no such self-consistency is imposed, and the pair amplitude inside the Bi_2Se_3 is completely due to the Andreev reflection from the interface [25, 26].

We study the z -dependence of the pair amplitudes in Bi_2Se_3 side ($z > 0$) in the three regimes: TI, M, and TM. For this purpose, we pick for each z in each spin

channel the largest eigenvalue $F_+^{s/t}(z)$ of the 2×2 matrix $\hat{F}^{s/t}(z)$, which indicates the leading instability in the given spin channel. In all three regimes, both spin-singlet and spin-triplet pair amplitudes are expected to be non-zero because of the spin-orbit coupling term in the Hamiltonian (3.1).

In Fig. 3.2, we plot $F_+^{s/t}(z)$ as a function of z . In the TI regime (Fig. 3.2a), we find that the pair amplitude is confined to the buried interface with exponential decay, since it is carried entirely by the surface states with such spatial profile. In addition, singlet and triplet components of the pair amplitude have the same magnitude as a result of spin-momentum locking of the surface states. In the M regime (Fig. 3.2b), on the other hand, the pair amplitudes show Friedel oscillations with an envelop that decays algebraically as a function of z . (See the Supplemental Material for an analytic understanding of the z dependence of the pair amplitudes in the M regime.¹) In addition, the singlet channel dominates over the triplet channel in the M regime.

The results in the TM regime (Fig. 3.2b) can be understood by combining the two pictures of the TI and the M regimes. In the TM regime, the pair amplitude consists of two components: the surface-states contribution and the bulk-states contribution, each of which should be qualitatively the same as the pair amplitude in the TI and the M regimes, respectively. At large distances where the bulk-states contribution is dominant, the pair amplitude should show a power-law-like decay. Friedel oscillation should also be present in principle, but in Fig. 3.2c, the large wavelength of the oscillation makes it difficult to identify the oscillation. With the power-law decay of the pair amplitude at large distances, superconductivity can be induced on the naked surface by proximity effect in the TM. This induced

¹See Supplemental Material for an analytic derivation of the pair amplitude in a one-dimensional example model.

pairing on the naked surface is a mixture of singlet and triplet components. The two components, however, lead to the identical effective BdG Hamiltonian for the surface states, as the surface states are fully spin-momentum locked.

3.4 Majorana Vortex Bound State on the Naked Surface

Next, we ask whether the naked surface of a TM with proximity-induced superconductivity can host MZMs. Formally related to the system of our interest is the 3D bulk superconducting Cu-doped Bi_2Se_3 . For this system Hosur *et al.* [27] predicted a vortex parallel to the c -axis to host a surface MZM even when the chemical potential is within the bulk conduction band, as long as it is below a critical value of ~ 0.24 eV from the bottom of the band. The chemical potential of an undoped Bi_2Se_3 falls within this range [28], and so does our definition of TM in our model. Hence a vortex in a TM proximity-coupled to a superconductor is likely to host a protected MZM at the naked surface. However, the effect of z -axis-dependent proximity-induced pairing strength on the naked surface and energetic stability of the MZM are not known *a priori*.

For concreteness, we solve the BdG equation on a cylindrical slab of Bi_2Se_3 with thickness L and radius R , with chemical potential in the TI and TM regimes. With the axis of the cylinder aligned along the z axis, we take the xy -coordinates to be continuous, while keeping the z coordinate discrete. The normal state Hamiltonian is then described by Eq. (3.1), with $\sin(k_i a) \rightarrow -ia\partial_i$ and $\cos(k_i a) \rightarrow 1 + \frac{1}{2}a^2\partial_i^2$ for $i = x, y$. Informed by our proximity effect calculation above, we impose an s -

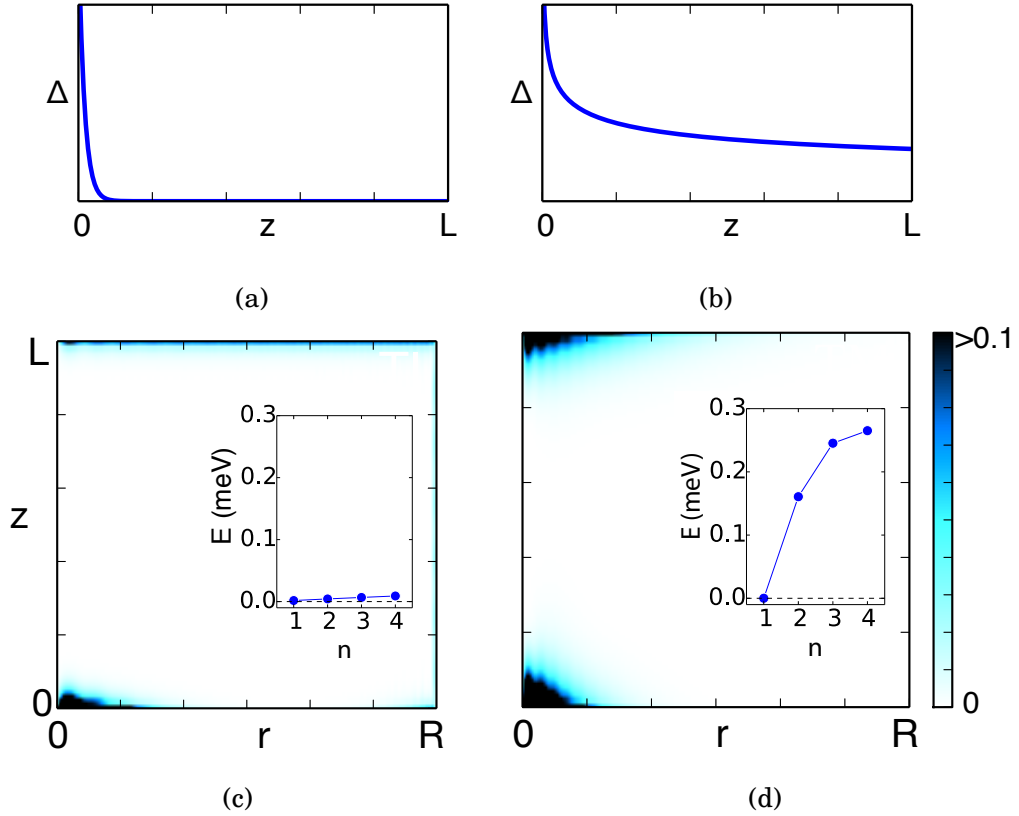


Figure 3.3: Panels (a) and (b) show the z dependence of the gap profile used to compute vortex-bound-state spectra for TI ($\mu = 25$ meV) and TM ($\mu = 50$ meV) regimes, respectively. Panels (c) and (d) show the spatial probability density profile $\rho_n(r,z)$, as defined in Eq. (3.8), of the lowest lying vortex bound state in two regimes. $\rho_n(r,z)$ has been normalized such that the maximum value is unity. The parameters used in the calculation are $a = 5 \text{ \AA}$, $R = 3000 \text{ \AA}$, $L = 500 \text{ \AA}$, $\Delta_0 = 5 \text{ meV}$, $z_0 = a/2$, $\xi_R = 100 \text{ \AA}$, and $\xi_L = 8 \text{ \AA}$ for TI and $\gamma = 1/4$ for TM. The inset in each case shows the vortex bound state spectrum, i.e. the energy E_n of the n th excitation.

wave superconducting gap of the following respective profiles for TI and TM:

$$\Delta_{\text{TI}}(r, \theta, z) = \Delta_0 \tanh(r/\xi_R) e^{i\theta} e^{-(z-z_0)/\xi_z}, \quad (3.5)$$

$$\Delta_{\text{TM}}(r, \theta, z) = \Delta_0 \tanh(r/\xi_R) e^{i\theta} (z/z_0)^{-\gamma}, \quad (3.6)$$

where (r, θ, z) is the cylindrical coordinate of the system. ξ_R and ξ_z are superconducting correlation lengths in the radial and the axial directions, respectively. We chose z_0 such that the bottom-most layer ($z = z_0$) of the TI/TM has a gap of magnitude Δ_0 , and a positive exponent γ is used for the gap profile to decay as z increases.

Because of the rotation symmetry of the system, it is convenient to use as basis the circular harmonics

$$\varphi_{vm}(r, \theta) = \frac{1}{\sqrt{\pi}R} \frac{J_v(\alpha_{vm} r/R)}{J_{v+1}(\alpha_{vm})} e^{iv\theta}, \quad (3.7)$$

where J_v is the Bessel function of the first kind of order v and α_{vm} is its m th zero. Expressed in terms of $\{\varphi_{vm}\}$, the Hamiltonian can be block diagonalized into different sectors of $L_z + S_z + Q/2$, where L_z and S_z are orbital angular momentum and spin of a quasiparticle in the z direction, and Q is its charge in units of $|e|$ (-1 for electron).

One can then diagonalize each block of the Hamiltonian, and find the low energy eigenstates. Each eigenstate $(u_{\alpha\sigma}^n(r, \theta, z), v_{\alpha\sigma}^n(r, \theta, z))$ can be identified using its spatial probability density defined as

$$\rho_n(r, z) \equiv r \sum_{\alpha, \sigma} \int \frac{d\theta}{2\pi} |u_{\alpha\sigma}^n(r, \theta, z)|^2 + |v_{\alpha\sigma}^n(r, \theta, z)|^2. \quad (3.8)$$

Figures 3.3c and 3.3d show $\rho_n(r, z)$ of the lowest excitation in the TI and TM regimes. In the TI regime, the superconducting gap decays exponentially away from the bottom surface, becoming negligible on the top surface. As a result a

zero-energy vortex bound state appears only on the bottom surface, and the top surface remains metallic (Fig. 3.3c). The resulting spectrum is shown in the inset of Fig. 3.3c. In the TM regime, on the other hand, the superconducting gap at the top surface is sizable, and a well-defined Majorana vortex bound state exists on both the top and the bottom surfaces. Hence the TM regime brings the best of both worlds: a stable zero mode on the experimentally accessible top surface.²

3.5 Conclusions

In summary, we studied the proximity effect in *topological metals*, i.e., topological insulators with bulk states at the Fermi level coexisting with well-defined surface states exhibiting spin-momentum locking. Against the common belief that ideal topological insulators should be bulk insulating, we showed that the existence of bulk carriers can be a feature for the proximity effect as the induced gap will be observable at the naked surface. Most importantly, we showed that a vortex line in a TM-SC structure will host an energetically stable Majorana bound state at the naked surface.

Although we focused on the proximity effect due to an *s*-wave superconductor for concreteness, our results are applicable to the proximity effect due to a *d*-wave superconductor such as the high- T_c cuprates as long as the induced gap is dominantly *s*-wave. In fact Wang *et al.* [16] observed an isotropic gap opening on the Dirac branch on a thin film of Bi_2Se_3 on a $\text{Bi}_2\text{Sr}_2\text{CaCu}_2\text{O}_{8+\delta}$ substrate below the superconducting transition temperature. While the mechanism for the larger value of the inferred surface-state gap compared to the bulk gap in Ref. [16]

²The same calculation in the M regime with gap function given by Eq. (3.6) trivially yields no zero mode, as expected.

remains unknown [29] and the results of Ref. [16] have not been reproduced to date [30], our results should apply as long as the induced isotropic gap is dominantly *s*-wave.

The setup of Bi_2Se_3 proximity coupled to superconducting NbSe_2 recently studied using ARPES and point-contact transport in Ref. [31] actually satisfy the condition of TM-SC structure as defined in this paper, according to their spin-momentum locking observations. Our results imply that the same system can support Majorana bound states at vortex cores with spatial separation between the top (naked) surface Majorana and the bottom (buried) surface Majorana. So far little attention has been given to experimentally distinguishing the two surfaces of TI in such a heterostructure, although Ref. [31] showed how the spectral gap at the Dirac point depends on the film thickness presumably due to varying degrees of coupling between the two surfaces. One way to experimentally identify the surface would be to use ARPES and look for the normal-state Fermi surface of the substrate. The Dirac state signal probed simultaneously with the substrate will be coming from both the top surface and the interface. When the film is thick enough to not show the substrate Fermi surface, the Dirac state signal will be coming from the naked top surface. In order to test our predictions we propose in-field STM measurements looking for Majorana bound states in a TM-SC setup like that of Ref. [31] in which spin-momentum locking is confirmed, with further attention given to distinguishing signals from each surface.

BIBLIOGRAPHY

1. Mourik, V. *et al.* Signatures of Majorana fermions in hybrid superconductor-semiconductor nanowire devices. *Science* **336**, 1003 (2012).
2. Das, A. *et al.* Zero-bias peaks and splitting in an Al-InAs nanowire topological superconductor as a signature of Majorana fermions. *Nat. Phys.* **8**, 887 (2012).
3. Rokhinson, L. P., Liu, X. & Furdyna, J. K. The fractional a.c. Josephson effect in a semiconductor-superconductor nanowire as a signature of Majorana particles. *Nat. Phys.* **8**, 795 (2012).
4. Deng, M. T. *et al.* Anomalous zero-bias conductance peak in a Nb-InSb nanowire-Nb hybrid device. *Nano Lett.* **12**. PMID: 23181691, 6414 (2012).
5. Chang, W., Manucharyan, V. E., Jespersen, T. S., Nygård, J. & Marcus, C. M. Tunneling spectroscopy of quasiparticle bound states in a spinful Josephson junction. *Phys. Rev. Lett.* **110**, 217005 (2013).
6. Finck, A. D. K., Van Harlingen, D. J., Mohseni, P. K., Jung, K. & Li, X. Anomalous modulation of a zero-bias peak in a hybrid nanowire-superconductor device. *Phys. Rev. Lett.* **110**, 126406 (2013).
7. Sau, J. D., Tewari, S., Lutchyn, R. M., Stanescu, T. D. & Das Sarma, S. Non-Abelian quantum order in spin-orbit-coupled semiconductors: Search for topological Majorana particles in solid-state systems. *Phys. Rev. B* **82**, 214509 (2010).
8. Lutchyn, R. M., Sau, J. D. & Das Sarma, S. Majorana fermions and a topological phase transition in semiconductor-superconductor heterostructures. *Phys. Rev. Lett.* **105**, 077001 (2010).

9. Oreg, Y., Refael, G. & von Oppen, F. Helical liquids and Majorana bound states in quantum wires. *Phys. Rev. Lett.* **105**, 177002 (2010).
10. Qi, X.-L., Hughes, T. L. & Zhang, S.-C. Topological invariants for the Fermi surface of a time-reversal-invariant superconductor. *Phys. Rev. B* **81**, 134508 (2010).
11. Kopnin, N. B. & Salomaa, M. M. Mutual friction in superfluid ^3He : Effects of bound states in the vortex core. *Phys. Rev. B* **44**, 9667 (1991).
12. Rice, T. M. & Sigrist, M. Sr_2RuO_4 : An electronic analogue of ^3He ? *J. Phys.: Condens. Matt.* **7**, L643 (1995).
13. Fu, L. & Kane, C. L. Superconducting proximity effect and Majorana fermions at the surface of a topological insulator. *Phys. Rev. Lett.* **100**, 096407 (2008).
14. Wray, L. A. *et al.* Observation of topological order in a superconducting doped topological insulator. *Nat. Phys.* **6**, 855 (2010).
15. Wang, M.-X. *et al.* The coexistence of superconductivity and topological order in the Bi_2Se_3 thin films. *Science* **336**, 52 (2012).
16. Wang, E. *et al.* Fully gapped topological surface states in Bi_2Se_3 films induced by a d-wave high-temperature superconductor. *Nat. Phys.* **9**, 621 (2013).
17. Liu, C.-X. *et al.* Model Hamiltonian for topological insulators. *Phys. Rev. B* **82**, 045122 (2010).
18. Hsieh, D. *et al.* A tunable topological insulator in the spin helical Dirac transport regime. *Nature* **460**, 1101 (2009).
19. Karch, A. Surface plasmons and topological insulators. *Phys. Rev. B* **83**, 245432 (2011).

20. Brahlek, M. *et al.* Topological-metal to band-insulator transition in $(\text{Bi}_{1-x}\text{In}_x)_2\text{Se}_3$ thin films. *Phys. Rev. Lett.* **109**, 186403 (2012).
21. Meyer, J. S. & Refael, G. Disordered topological metals. *Phys. Rev. B* **87**, 104202 (2013).
22. Junck, A., Kim, K. W., Bergman, D. L., Pereg-Barnea, T. & Refael, G. Transport through a disordered topological-metal strip. *Phys. Rev. B* **87**, 235114 (2013).
23. Hsu, Y.-T., Fischer, M. H., Hughes, T. L., Park, K. & Kim, E.-A. Effects of surface-bulk hybridization in three-dimensional topological metals. *Phys. Rev. B* **89**, 205438 (2014).
24. Black-Schaffer, A. M. & Balatsky, A. V. Proximity-induced unconventional superconductivity in topological insulators. *Phys. Rev. B* **87**, 220506 (2013).
25. Andreev, A. F. The thermal conductivity of the intermediate state in superconductors. *Sov. Phys. JETP* **19**, 1228 (1963).
26. Blonder, G. E., Tinkham, M. & Klapwijk, T. M. Transition from metallic to tunneling regimes in superconducting microconstrictions: Excess current, charge imbalance, and supercurrent conversion. *Phys. Rev. B* **25**, 4515 (1982).
27. Hosur, P., Ghaemi, P., Mong, R. S. K. & Vishwanath, A. Majorana modes at the ends of superconductor vortices in doped topological insulators. *Phys. Rev. Lett.* **107**, 097001 (2011).
28. Xia, Y. *et al.* Observation of a large-gap topological-insulator class with a single Dirac cone on the surface. *Nat. Phys.* **5**, 398 (2009).
29. Li, Z.-X., Chan, C. & Yao, H. Realizing Majorana zero modes by proximity effect between topological insulators and *d*-wave high-temperature superconductors. *Phys. Rev. B* **91**, 235143 (2015).

30. Yilmaz, T. *et al.* Absence of a proximity effect for a thin-films of a Bi_2Se_3 topological insulator grown on top of a $\text{Bi}_2\text{Sr}_2\text{CaCu}_2\text{O}_{8+\delta}$ cuprate superconductor. *Phys. Rev. Lett.* **113**, 067003 (2014).
31. Xu, S.-Y. *et al.* Momentum-space imaging of Cooper pairing in a half-Dirac-gas topological superconductor. *Nat. Phys.* **10**, 943 (2014).

CHAPTER 4

**SCANNING TUNNELING SPECTROSCOPY AND
QUASIPARTICLE INTERFERENCE**

Scanning tunneling spectroscopy (STS) is a technique which measures real-space electronic structure. A scanning tunneling microscope consists of an atomically sharp tip which is brought very close to a sample surface. As the tip scans across the surface, voltage is applied between tip and sample, and the resulting current flow is measured as a function of location.

By design an STM is a surface probe, with two-dimensional spatial resolution. Fortunately, electronic structures of many unconventional superconductors – especially cuprates but also many iron-based superconductors and also strontium ruthenates – have highly two-dimensional character, and STS has played a crucial role. In this chapter, we review basic theory behind the STS technique. We then discuss the quasiparticle interference (QPI) technique, which reveals momentum space information of the electronic structure of the sample.

4.1 Tunneling of Electron

The tunneling process of electron from tip to sample (and vice versa) can be understood using time-dependent perturbation theory. For simplicity, let us first consider a one-dimensional tunneling between a “tip” and a “sample”. The rate of tunneling from a state at the tip $|\Psi_t\rangle$ with energy E_t to a state at the surface $|\Psi_s\rangle$ with energy E_s is

$$R_{st} = 2\pi |M_{st}|^2 \delta(E_t - E_s) \quad (4.1)$$

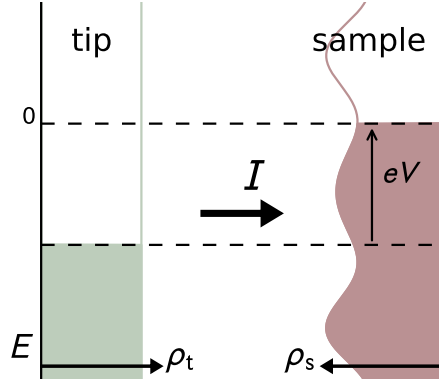


Figure 4.1: Schematic diagram describing tunneling of electron from tip to sample.

where the tunneling matrix element M_{st} is given by

$$M_{st} \approx \frac{1}{2m} \left(\left\langle \Psi_s \left| \frac{\partial}{\partial z} \right| \Psi_t \right\rangle - \left\langle \Psi_t \left| \frac{\partial}{\partial z} \right| \Psi_s \right\rangle \right) \quad (4.2)$$

Then the tunneling current from tip to sample which tunnels from tip to sample, is given by

$$I = 2\pi e \int dE |M_{st}|^2 \rho_t(E - eV) \rho_s(E) (f_D(E - eV) - f_D(E)), \quad (4.3)$$

where $f_D(E) = (1 + e^{\beta E})^{-1}$ is the Fermi-Dirac distribution function. At zero temperature the current becomes

$$I = 2\pi e \int_0^{eV} dE |M_{st}|^2 \rho_t(E - eV) \rho_s(E) \quad (4.4)$$

The tip is typically made of a metallic material with nearly constant density of states near the Fermi energy. Then,

$$I \approx 2\pi e \rho_t(0) \int_0^{eV} dE |M_{st}|^2 \rho_s(E) \quad (4.5)$$

Taking derivative, we find

$$\frac{dI}{dV} = 2\pi e^2 |M_{st}|^2 \rho_t(0) \rho_s(eV) \propto \rho_s(eV). \quad (4.6)$$

The “differential conductivity” dI/dV can therefore be used as a measure of density of states. The data acquired by STM has two-dimensional spatial resolution: as the tip scans across the surface, and the measured differential conductivity changes as a function of position. Therefore, the $dI/dV(\mathbf{x})$ is often referred to as “local” density of states (LDOS).

4.2 Quasiparticle Interference

By definition, local density of states picks up spatial variation of electronic structure. It is, nevertheless, possible to extract momentum space information about the electronic structure, by making use of impurity scattering. Since impurity breaks translation symmetry and mixes states with different (crystal) momenta, creating standing wave interference pattern near an impurity known as Friedel oscillation. In STM, Friedel oscillation was first observed in two-dimensional electron gas [1]: The wavelength of the oscillation allowed the measurement of Fermi wavevector. Similar idea, often referred to as quasiparticle interference (QPI), has been applied to study unconventional superconductors such as cuprates, iron-pnictides, as well as topological insulators/superconductors.

The quasiparticle interference pattern can be calculated using time-dependent Green’s function. Let us first consider a spinless fermion system. Local density of states at position \mathbf{x} and energy ω can be expressed in terms of retarded Green’s function \mathcal{G} :

$$\rho(\mathbf{x}, \omega) = -\frac{1}{\pi} \text{Im} \mathcal{G}(\mathbf{x}, \mathbf{x}; \omega). \quad (4.7)$$

In a clean system without impurities, the Green’s function $\mathcal{G}(\mathbf{x}, \mathbf{y}; \omega)$ is transla-

tionally invariant, and thus can be written as

$$\mathcal{G}(\mathbf{x}, \mathbf{y}; \omega) = G(\mathbf{x} - \mathbf{y}; \omega). \quad (4.8)$$

This is consistent with the fact that $\rho(\mathbf{x}, \omega)$ need to be uniform. After introducing a single “ δ function” scatterer to the system at $\mathbf{x} = 0$, the leading order variation of local density of states is

$$\delta\rho(\mathbf{x}; \omega) = -\frac{1}{\pi}\text{Im}[G(\mathbf{x}; \omega)VG(-\mathbf{x}; \omega)]. \quad (4.9)$$

whose Fourier transform

$$\rho(\mathbf{q}, \omega) = -\frac{1}{2\pi}\sum_{\mathbf{k}}\text{Im}[G(\mathbf{k}, \omega)VG(\mathbf{k} + \mathbf{q}, \omega) + G(\mathbf{k}, \omega)VG(\mathbf{k} - \mathbf{q}, \omega)] \quad (4.10)$$

is often referred to as *quasiparticle interference pattern*.

The expression Eq. (4.10) can be generalized to a system with spin or orbital degrees of freedom. Local density of states in a spinful/multi-orbital system can be expressed as

$$\rho(\mathbf{x}, \omega) = -\frac{1}{\pi}\sum_{\alpha}\text{Im}\mathcal{G}_{\alpha\alpha}(\mathbf{x}, \mathbf{x}; \omega) \quad (4.11)$$

This gives the Fourier transform of LDOS as

$$\rho(\mathbf{q}, \omega) = -\frac{1}{2\pi}\sum_{\mathbf{k}}\sum_{\alpha\beta\gamma}\left[G_{\alpha\beta}(\mathbf{k}, \omega)V_{\beta\gamma}G_{\gamma\alpha}(\mathbf{k} + \mathbf{q}, \omega) + G_{\alpha\beta}(\mathbf{k}, \omega)V_{\beta\gamma}G_{\gamma\alpha}(\mathbf{k} - \mathbf{q}, \omega)\right] \quad (4.12)$$

where $V_{\alpha\beta}$ is the scattering amplitude between orbitals α and β .

Generalization of the above discussion to superconducting state is straight forward. The Green's function in a superconductor can be written in Nambu basis as

$$\widehat{\mathcal{G}}(\mathbf{x}, \mathbf{y}, \omega) = \begin{pmatrix} \mathcal{G}^{ee}(\mathbf{x}, \mathbf{y}, \omega) & \mathcal{G}^{eh}(\mathbf{x}, \mathbf{y}, \omega) \\ \mathcal{G}^{he}(\mathbf{x}, \mathbf{y}, \omega) & \mathcal{G}^{hh}(\mathbf{x}, \mathbf{y}, \omega) \end{pmatrix} \quad (4.13)$$

where \mathcal{G}^{ee} , \mathcal{G}^{eh} , \mathcal{G}^{he} , and \mathcal{G}^{hh} can themselves be matrices. The off-diagonal terms \mathcal{G}^{eh} and \mathcal{G}^{he} are often called *anomalous Green's function*. Since the local density of states $\rho(\mathbf{x}, \omega)$ measures the density of “electronic” states at energy ω (or equivalently, hole states at energy $-\omega$), only \mathcal{G}^{ee} contributes:

$$\rho(\mathbf{x}, \omega) = -\frac{1}{\pi} \sum_{\alpha} \text{Im} \mathcal{G}_{\alpha\alpha}^{ee}(\mathbf{x}, \mathbf{x}, \omega) \quad (4.14)$$

which, following the same steps as the normal-state Green's function, becomes

$$\rho(\mathbf{q}, \omega) = -\frac{1}{2\pi} \sum_{\mathbf{k}} \sum_{\alpha} \left[\hat{G}(\mathbf{k}, \omega) \cdot \hat{V} \cdot \hat{G}(\mathbf{k} + \mathbf{q}, \omega) + \hat{G}(\mathbf{k}, \omega) \cdot \hat{V} \cdot \hat{G}(\mathbf{k} - \mathbf{q}, \omega) \right]_{\alpha\alpha}^{ee} \quad (4.15)$$

where \hat{V} is the scattering potential in Nambu basis. For example, a scatter with scattering amplitude $V_{\alpha\beta}$ between spin α and β ,

$$\hat{V}_{\alpha\beta} = \begin{pmatrix} V_{\alpha\beta} & 0 \\ 0 & -V_{\beta\alpha} \end{pmatrix}. \quad (4.16)$$

BIBLIOGRAPHY

1. Crommie, M. F., Lutz, C. P. & Eigler, D. M. Imaging standing waves in a two-dimensional electron gas. *Nature* **363**, 524 (1993).

CHAPTER 5

RESEARCH PAPER:

**IDENTIFYING THE ‘FINGERPRINT’ OF ANTIFERROMAGNETIC
SPIN-FLUCTUATIONS IN IRON-PNICTIDE COOPER PAIRING**

M. P. Allan^{1,2†}, Kyungmin Lee^{1†}, A. W. Rost^{1,3,4†}, M. H. Fischer¹, F. Massee^{1,2},
K. Kihou^{5,6}, C-H. Lee^{5,6}, A. Iyo^{5,6}, H. Eisaki^{5,6}, T-M. Chuang⁷, J. C. Davis^{1,2,3,8},
and Eun-Ah Kim¹

¹*LASSP, Department of Physics, Cornell University, Ithaca, New York 14853, USA.*

²*CMPMS Department, Brookhaven National Laboratory, Upton, New York 11973, USA.*

³*School of Physics and Astronomy, University of St. Andrews, St. Andrews, Fife KY16
9SS, Scotland.*

⁴*Department of Physics, The University of Tokyo, Bunkyo-ku, Tokyo 113-0033, Japan.*

⁵*Institute of Advanced Industrial Science and Technology, Tsukuba, Ibaraki 305-8568,
Japan.*

⁶*JST, Transformative Research-Project on Iron Pnictides (TRIP), Tokyo 102-0075, Japan.*

⁷*Institute of Physics, Academia Sinica, Nankang, Taipei 11529, Taiwan.*

⁸*Kavli Institute at Cornell for Nanoscale Science, Cornell University, Ithaca, New York
14853, USA.*

[†]*These authors contributed equally to this work.*

Published on Nature Physics **11**, 177-182 (2015).

Abstract

Cooper pairing in the iron-based high-T_c superconductors [1–3] is often conjectured to involve bosonic fluctuations. Among the candidates are antiferromagnetic spin fluctuations [1, 4, 5] and d-orbital fluctuations amplified by phonons [6, 7]. Any such electron–boson interaction should alter the electron’s ‘self-energy’, and then become detectable through consequent modifications in the energy dependence of the electron’s momentum and lifetime [8–10]. Here we introduce a novel theoretical/experimental approach aimed at uniquely identifying the relevant fluctuations of iron-based superconductors by measuring effects of their self-energy. We use innovative quasiparticle interference (QPI) imaging [11] techniques in LiFeAs to reveal strongly momentum-space anisotropic self-energy signatures that are focused along the Fe–Fe (interband scattering) direction, where the spin fluctuations of LiFeAs are concentrated. These effects coincide in energy with perturbations to the density of states $N(\omega)$ usually associated with the Cooper pairing interaction. We show that all the measured phenomena comprise the predicted QPI ‘fingerprint’ of a self-energy due to antiferromagnetic spin fluctuations, thereby distinguishing them as the predominant electron–boson interaction.

The microscopic mechanism for Cooper pairing in iron-based high-temperature superconductors has not been identified definitively [1–3]. Among the complicating features in these superconductors is the multiband electronic structure (Fig. 5.1a). However, it is believed widely that the proximity to spin order [1–5] and/or orbital order [6, 7] plays a key role in the Cooper pairing. In particular, two leading proposals for fluctuation-exchange-pairing mechanisms focus on two distinct bosonic modes associated with specific broken-symmetry states: antiferromagnetic spin fluctuations carrying momentum $\mathbf{Q} = (\pi, \pi)/a_0$, and d -orbital fluctuations amplified by E_g -phonon lattice vibrations of the Fe ions. No conclusive evidence that either fluctuation couples strongly to electrons and is thus relevant to Fe-based superconductivity has been achieved within the plethora of proposals about the existing data [12–18].

Each type of electron–boson interaction should produce a characteristic electronic ‘self-energy’ $\hat{\Sigma}(\mathbf{k}, \omega)$ representing its effect on every non-interacting electronic state $|\mathbf{k}\rangle$ fence with momentum $\hbar\mathbf{k}$ and energy $\hbar\omega$. Thus, the interacting Green’s function $\hat{G}(\mathbf{k}, \omega)$ is given by

$$[\hat{G}(\mathbf{k}, \omega)]^{-1} = [\hat{G}^0(\mathbf{k}, \omega)]^{-1} - \hat{\Sigma}(\mathbf{k}, \omega) \quad (5.1)$$

where $\hat{G}^0(\mathbf{k}, \omega)$ represents non-interacting electrons and the detailed structure of $\hat{\Sigma}(\mathbf{k}, \omega)$ encapsulates the Cooper pairing process. Here, a hat ($\hat{}$) denotes a matrix in particle–hole space (Nambu space) for Bogoliubov quasiparticles in the superconducting state. The real part $\text{Re}\hat{\Sigma}(\mathbf{k}, \omega)$ then describes changes in the electron’s dispersion $\mathbf{k}(\omega)$ and the imaginary part $\text{Im}\hat{\Sigma}(\mathbf{k}, \omega)$ describes changes in its inverse lifetime $\tau^{-1}(\mathbf{k}, \omega)$. The simplest diagrammatic representation of this electron–boson interaction is shown in Fig. 5.1b. One way to detect the experimen-

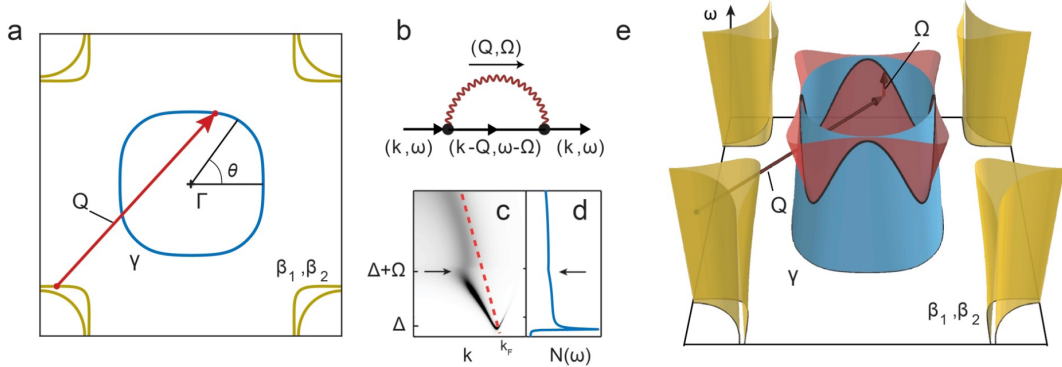


Figure 5.1: Electronic self-energy due to coupling to bosonic fluctuations. (a) Electronic structure of the first Brillouin zone of FeAs superconductors; here shown using parameters specific to LiFeAs (the inner hole pockets are omitted for clarity). The γ band surrounds the Γ point, the β_1 and β_2 bands are hybridized surrounding the M point at the corner. The AFSF with $\mathbf{Q} = (\pi, \pi)/a_0$ (red arrow) can connect the hole-like bands surrounding the Γ point with the electron-like bands surrounding the M point. (b) Diagram of the lowest order self-energy contribution from electron–boson interactions. (c) Spectral function $A(\mathbf{k}, \omega) \propto \text{Im}G(\mathbf{k}, \omega)$ of a superconducting hole-like band (with unrenormalized normal-state dispersion shown as a red dashed line) with the superconducting gap Δ and the dispersion renormalization at energy $\Delta + \Omega$ (arrow) due to coupling to a phonon of frequency Ω . (d) Density of electronic states spectrum $N(\omega)$ associated with (c), showing a kink at energy $\Delta + \Omega$. (e) Schematic view of the kinematic constraint in (\mathbf{k}, ω) -space. We find that the self-energy features on the γ band can only appear at $(\mathbf{k}, \omega_{\mathbf{k}}^{\gamma})$ if there exists a partner point $(\mathbf{k} - \mathbf{Q}, \omega_{\mathbf{k}-\mathbf{Q}}^m)$ with $\omega_{\mathbf{k}-\mathbf{Q}}^m = \omega_{\mathbf{k}}^{\gamma} - \Omega \geq \Delta$ to satisfy the kinematic constraint. The blue surface at the centre and the yellow surfaces at the corners of the Brillouin zone are defined by the hole-band and the outer-electron-band dispersion. The red surface indicates the hole band displaced by the AFSF momentum $\mathbf{Q} = (\pi, \pi)/a_0$ (dark red arrow) and energy Ω (light red arrow). The points that satisfy the kinematic constraint (Eq. (5.1)) are defined by the intersection of the red and blue surfaces, and indicated with a solid black line. These points are expected to exhibit the strongest self-energy effects due to coupling to AFSF. The anisotropy of the black line demonstrates directly how the AFSF self-energy effects must exist at different ω in different \mathbf{k} -space directions around a particular Fermi pocket (for example, the γ band in a).

tal signature of such a self-energy is to use angle-resolved photoemission spectroscopy (ARPES) to measure the spectral function $A(\mathbf{k}, \omega) \propto \text{Im}G(\mathbf{k}, \omega)$ of the states with $\omega < 0$. However, it has recently been realized that quasiparticle interference imaging, which can access momentum-resolved information of both filled and empty states with excellent energy resolution ($\delta\omega < 0.35\text{meV}$ at $T = 1.2\text{ K}$), might prove especially advantageous for detecting self-energy effects [19]. Our QPI data are obtained by first visualizing scattering interference patterns in real-space (\mathbf{r} -space) images of the tip–sample differential tunnelling conductance $dI/dV(\mathbf{r}, \omega = e\text{V}) \equiv g(\mathbf{r}, \omega)$ using spectroscopic-imaging scanning tunnelling microscopy, and then Fourier transforming $g(r, \omega)$ to obtain the power spectral density $g(\mathbf{r}, \omega)$ (Ref. [11]). The $g(\mathbf{r}, \omega)$ can then be used to reveal the electron dispersion $\mathbf{k}(\omega)$ because elastic scattering of electrons from $-\mathbf{k}(\omega)$ to $+\mathbf{k}(\omega)$ results in high intensity at $\mathbf{q}(\omega) = 2\mathbf{k}(\omega)$ in $g(\mathbf{q}, \omega)$. Sudden changes in the energy evolution $\mathbf{k}(\omega)$ due to $\Sigma(\mathbf{k}, \omega)$ can then be determined, in principle [19], using such data.

In a conventional single-band s -wave superconductor with isotropic energy gap magnitude Δ , it has been well established that coupling to an optical phonon with frequency Ω can lead to a renormalization of the electronic spectra at energy $\Delta + \Omega$ ($\hbar = 1$) due to a singularity in the momentum-independent self-energy $\Sigma(\mathbf{k}, \omega) = \Sigma(\omega)$ at $\omega = \Delta + \Omega$ (Ref. [20]). This classic case is illustrated in Fig. 5.1(c,d) through a model spectral function $A(\mathbf{k}, \omega) \propto \text{Im}G(\mathbf{k}, \omega)$ and the associated density of states $N(\omega) = \int d\mathbf{k}A(\mathbf{k}, \omega)$. In Fig. 5.1c, the ‘free’ dispersion of a hole-like band is represented by the red dashed line, while the renormalized dispersion $\mathbf{k}(\omega)$ due to $\Sigma(\omega)$ is highlighted by the locus of maxima in $A(\mathbf{k}, \omega)$. These effects can be understood from the conservation of energy and momentum during scattering processes (Fig. 5.1b), where the flat dispersion of an optical phonon presents constraints only on energy, without any momentum dependence.

In developing our new approach to ‘fingerprinting’ different electron–boson interactions using QPI, we use the realization that the kinematic constraints for a multiband electronic system coupled to resonant AFSF with a sharp momentum structure should result in a strongly momentum-dependent (anisotropic) self-energy. This is because, given a fermionic dispersion $(\mathbf{k}, \omega_{\mathbf{k}}^n)$ for different bands n and a spectrum of spin fluctuations whose intensity is strongly concentrated at (\mathbf{Q}, Ω) , the renormalization due to the self-energy at a point $(\mathbf{k}, \omega_{\mathbf{k}}^n)$ will be most intense when that point can be connected to another point $(\mathbf{k} - \mathbf{Q}, \omega_{\mathbf{k}-\mathbf{Q}}^m)$ on a different band m , such that

$$\omega_{\mathbf{k}}^n = \omega_{\mathbf{k}-\mathbf{Q}}^m - \Omega \quad (5.2)$$

This is the constraint from conservation of both energy and momentum in the electron–AFSF interaction and its consequence is shown schematically in Fig. 5.1e. Here the blue (yellow) surfaces represent the hole (electron) bands. The transfer of momentum $\mathbf{Q} = (\pi, \pi)/a_0$ and energy Ω necessary for the resonant anti-ferromagnetic fluctuation to couple these bands can be analysed by shifting the electron-pocket-dispersion surface (horizontally) by \mathbf{Q} and (vertically) by Ω in the \mathbf{k} – ω space, to obtain the transparent red surface. The black curve, showing the intersection of this red surface with the central γ -band dispersion (blue), is where the kinematic constraint of Eq. (5.1) can be satisfied and thus where the strongest self-energy effect due to coupling to AFSF is predicted. The resulting strongly anisotropic renormalization due to electron–AFSF coupling is in strong contrast to what is expected as a consequence of the electron–phonon coupling case discussed in the previous paragraph.

Here we study the representative iron-based superconductor LiFeAs as a concrete example for which it should be possible to make a clear theoretical distinction between the self-energy effects driven by different types of bosonic fluctu-

ations. We assume that BCS theory adequately describes the superconductor deep in the superconducting phase. Hence, the non-interacting Green's function is given by

$$\left[\hat{G}^0(\mathbf{k}, \omega) \right]^{-1} = \omega \hat{\tau}_0 - \Delta_{\mathbf{k}} \hat{\tau}_1 - H_{\mathbf{k}}^0 \hat{\tau}_3 \quad (5.3)$$

where $\hat{\tau}_0$ and $\hat{\tau}_i$ are the identity and the Pauli matrices in Nambu space, respectively. The superconducting gap structure $\Delta_{\mathbf{k}}$ and the band structure $H_{\mathbf{k}}^0$ are taken from experiments [11, 12, 17] and *ab-initio* calculations [21]. We then study the lowest order self-energy due to the coupling between Bogoliubov quasiparticles and two bosonic modes: a resonant AFSF (Ref. [22, 23]) and an optical phonon of the type driving orbital fluctuations due to in-plane lattice vibrations of the Fe ions with E_g symmetry (Fe- E_g phonon). It is the coupling of this Fe- E_g phonon to electrons that is proposed to enhance the d-orbital fluctuations which mediate Cooper pairing in the orbital fluctuation mechanism [6, 7]. We take a perturbative approach of computing the self-energy to the lowest order [9]:

$$\hat{\Sigma}_{mn}^{(1)}(\mathbf{k}, \omega) = \int d\mathbf{q} dv D(\mathbf{q}, v) \hat{g}_{ml} \hat{G}_{ll'}^0(\mathbf{k} - \mathbf{q}, \omega - v) \hat{g}_{l'n} \quad (5.4)$$

where the repeated indices are summed over. Given independent quantitative knowledge of the gap structure, such a perturbative treatment can accurately capture the salient features of renormalization due to electron–boson coupling. In Eq. (5.2), the bosonic Green's function $D(\mathbf{q}, v)$ is sharply peaked around $\mathbf{Q} = (\pi, \pi)/a_0$ with the characteristic energy of $\Omega \approx 6\text{meV}$ to model the resonant AFSF of LiFeAs (Ref. [22, 23]), whereas it is nearly momentum-independent for the optical E_g phonon [20]. We focus on the self-energy effects on the γ band (Fig. 5.1a, e) in the rest of this paper as its nearly uniform orbital character (d_{xy}) greatly simplifies the theoretical study while at the same time being readily accessible to QPI studies [11]. Given the geometry of the Fermi surfaces, the kinematic constraint for coupling to resonant AFSF with momentum \mathbf{Q} and energy Ω

(red arrows in Fig. 5.1e) connects a given $(\mathbf{k}, \omega_{\mathbf{k}}^{\gamma})$ on the γ band (blue surface in Fig. 5.1e) to a point with momentum $\mathbf{k} - \mathbf{Q}$ on one of the two electron-like bands (yellow surfaces in Fig. 5.1e). Thus, the distinct anisotropic dispersions of each band mean that resonant AFSF should result in self-energy effects with a strong directional dependence (black curve on the γ band in Fig. 5.1e). Similarly, for the Fe-E_g phonons with a weak momentum dependence [7], the self-energy effect for the γ band (which consists almost entirely of d_{xy} orbitals [24]) is predicted to be angle-independent.

In Fig. 5.2a–d we present the predictions from Eq. (5.2) for $g(\mathbf{q}, \omega)$ in LiFeAs, in the presence of self-energy effects due to coupling to AFSF. Just below the maximum gap value on the γ band of 3 meV (Fig. 5.2a), the high-intensity region around $\mathbf{q} \approx 2\mathbf{k}_F^{\gamma}$ shows an anisotropy dictated by the gap anisotropy [11, 17, 25], with the QPI intensity suppressed along the gap maximum (Fe–As) direction. At energies exceeding the maximum gap values, the predicted $g(\mathbf{q}, \omega)$ at first becomes isotropic (Fig. 5.2b) as one might expect from the fact that the Bogoliubov energy is dominated by the kinetic energy over the gap at high energies. However, at energies $\omega \geq 12$ meV the predicted self-energy effects for the AFSF self-energy (Fig. 5.2c, d) are seen and, in fact, strongly suppress the $g(\mathbf{q}, \omega)$ intensity in the Fe–Fe direction relative to the Fe–As direction. The complete predicted evolution of $g(\mathbf{q}, \omega)$, from being dominated by the anisotropic gap structure [11] to the new effects of the AFSF-driven $\Sigma(\mathbf{k}, \omega)$ introduced here, is shown in the left panels of the Supplementary Movie 1.

The experimental search for such signatures of $\Sigma(\mathbf{k}, \omega)$ in QPI data consists of imaging $g(\mathbf{r}, \omega)$ at $T = 1.2$ K with 0.35 meV energy resolution on LiFeAs samples exhibiting $T_c \approx 15$ K and with the superconducting energy gap maxi-

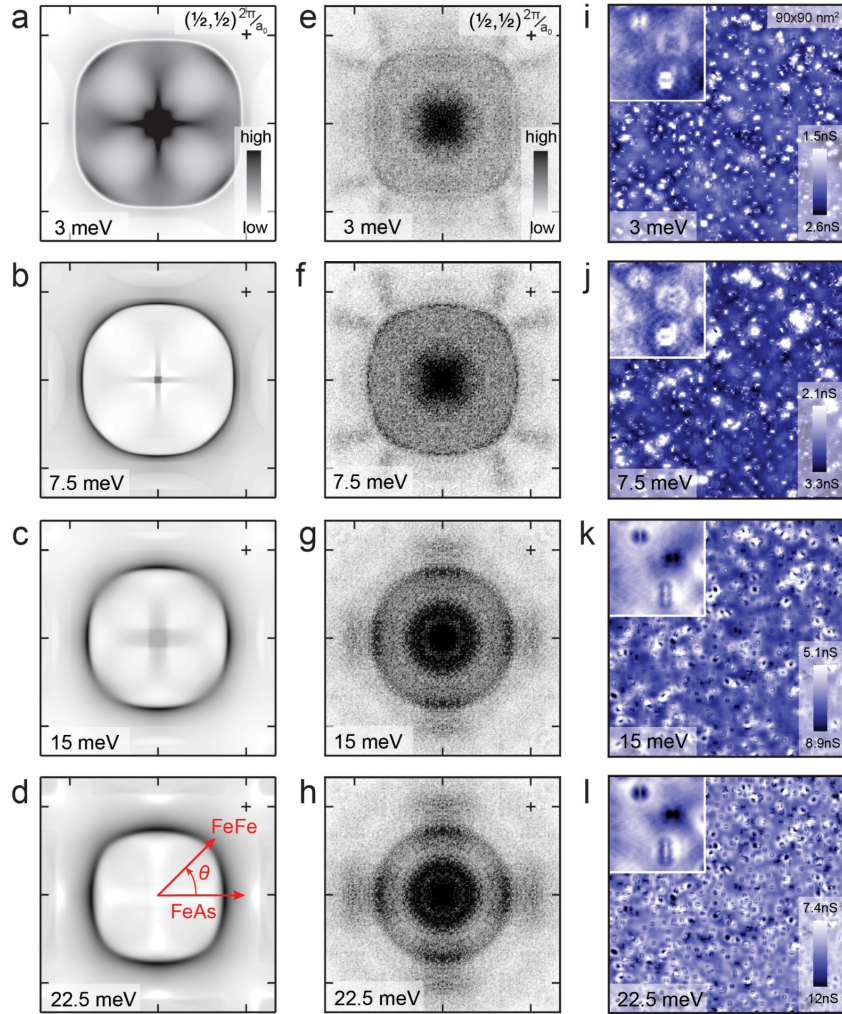


Figure 5.2: Comparison between scattering interference theory with AFSF-driven self-energy effects and the experiments. (a–d) Theoretically predicted QPI patterns $g(\mathbf{q}, \omega)$ for LiFeAs with Green's function including the self-energy effect due to the coupling between electrons and resonant AFSF fluctuations. In these simulations, we suppressed the interband scattering visible in the data to highlight the QPI of the γ band that are the focus of this study. Note, in (c,d) the strong anisotropy induced by the kinematic constraint (Eq. (5.1)) with clear suppression of $g(\mathbf{q}, \omega)$ for \mathbf{q} along the Fe–Fe direction, which is strikingly different from the strong gap anisotropy that dictates the pattern in (a). (e–h) Measured QPI patterns $g(\mathbf{q}, \omega)$ (obtained from $g(\mathbf{r}, \omega)$ of LiFeAs). (e) QPI signature of anisotropic energy gaps. (f) Expected isotropic signature of the complete Fermi surface of the γ band. (g,h) Transition to a strongly anisotropic $g(\mathbf{q}, \omega)$. Note the suppression of $g(\mathbf{q}, \omega)$ occurring along the Fe–Fe direction. (i–l) Real-space images of $g(\mathbf{r}, \omega)$ from which (e–h) were obtained. The insets show a zoom-in onto a particular impurity, revealing the real-space standing waves from QPI.

mum $|\Delta_{\max}| = 6.5(1)\text{meV}$. Clean and flat Li-termination surfaces (Li–Li unit cell $a_0 = 0.38\text{ nm}$) allowed our atomic resolution/register $g(\mathbf{r}, \omega)$ measurements to be carried out over the energy range $|\omega| < 30\text{ meV}$. We then derive the $g(\mathbf{q}, \omega)$ in Fig. 5.2e–h from the measured $g(\mathbf{r}, \omega)$ at each energy, as shown in Fig. 5.2i–l. In Fig. 5.2e we see the expected QPI signature of the anisotropic energy gaps on multiple bands (compare Fig. 5.2a). Figure 5.2f shows the characteristic signature of the complete Fermi surface of the γ band of LiFeAs at ω just outside the superconducting gap edge on that band (compare Fig. 5.2b). If none of the electron–boson self-energy phenomena intervened one would expect this closed contour (Fig. 5.2f) to evolve continuously to smaller and smaller q -radius with increasing ω until the top of this hole-like band is reached. Instead, Fig. 5.2g shows the beginning of a very different evolution. Above $\omega \sim 12\text{ meV}$, the q -space features become strongly anisotropic in a fashion highly unexpected for unrenormalized states. Indeed, the strongly suppressed $g(\mathbf{q}, \omega)$ intensity in the Fe–Fe direction relative to the Fe–As direction is very similar to the predictions for $\Sigma(\mathbf{k}, \omega)$ due to AFSF (Fe–Fe direction Fig. 5.2d).

We compare these results to the predicted $g(\mathbf{q}, \omega)$ signatures of a self-energy $\Sigma(\mathbf{k}, \omega)$ due to phonons whose strong coupling to electrons is a central premise for the orbital fluctuation scenario. Clearly, comparison of predictions due to the two different boson couplings presented in Fig. 5.3 through the ω and $|\mathbf{q}|$ dependence of $g(\mathbf{q}, \omega)$ for the Fe–E_g phonon (Fig. 5.3a–c) and AFSF (Fig. 5.3d–f) can provide a distinguishing ‘fingerprint’ of AFSF-driven effects. The AFSF cause maximum renormalization (peaks of the blue curve) in relatively narrow ‘beams’ in the Fe–Fe directions, precisely where the resonant spin fluctuations are concentrated owing to interband scattering (see Fig. 5.3g). By contrast the electron–E_g-phonon interaction is predicted to yield isotropic self-energy signatures (red curve) in QPI

data.

In Fig. 5.4a we show a complete representation of our measured data using a combined \mathbf{q} - ω presentation of $g(\mathbf{q}, \omega)$ for $0 < \omega < 30$ meV (Γ -X and Γ -M \mathbf{k} -space directions are shown in \mathbf{q} -space); these data are most clearly demonstrated in Supplementary Movie 1. Most striking in the $g(\mathbf{q}, \omega)$ are the anisotropic ‘kinks’ in $\mathbf{q}(\omega)$ indicated by red arrows. Figure 5.4b shows the simultaneously measured normalized conductance (\sim density of states $N(\omega)$), with the characteristic features of pairing interactions indicated by red arrows; these occur within the energy range of the ‘kinks’ in $\mathbf{q}(\omega)$. Figure 5.4c–e show plots of $g(\mathbf{q}, \omega)$ data along different directions. Figure 5.4f shows the measured dispersion of the maxima of these $g(\mathbf{q}, \omega)$. The inflection points of the $g(\mathbf{q}, \omega)$ dispersion seen in Fig. 5.4a, f, which are directly related to the band renormalization from $\text{Re}\Sigma(\mathbf{k}, \omega)$, are obviously strongly anisotropic in \mathbf{q} -space and strongest in the Fe–Fe direction. Finally, Fig. 5.4g shows measured values of ΔE , the departure of the dispersion of the maxima in $g(\mathbf{q}, \omega)$ from a model with no self-energy effect, versus the angle θ around the γ band. This is to be compared with the theoretical prediction in Fig. 5.3g. The good correspondences between our theoretical prediction for $\text{Re}\Sigma(\mathbf{k}, \omega)$ effects from coupling to AFSF (Fig. 5.3g) and the QPI measurements (Fig. 5.2e–h) are evident. If the optical phonon conjectured to exist in the same energy range is strongly coupling to electrons, a far more isotropic dependence would be expected.

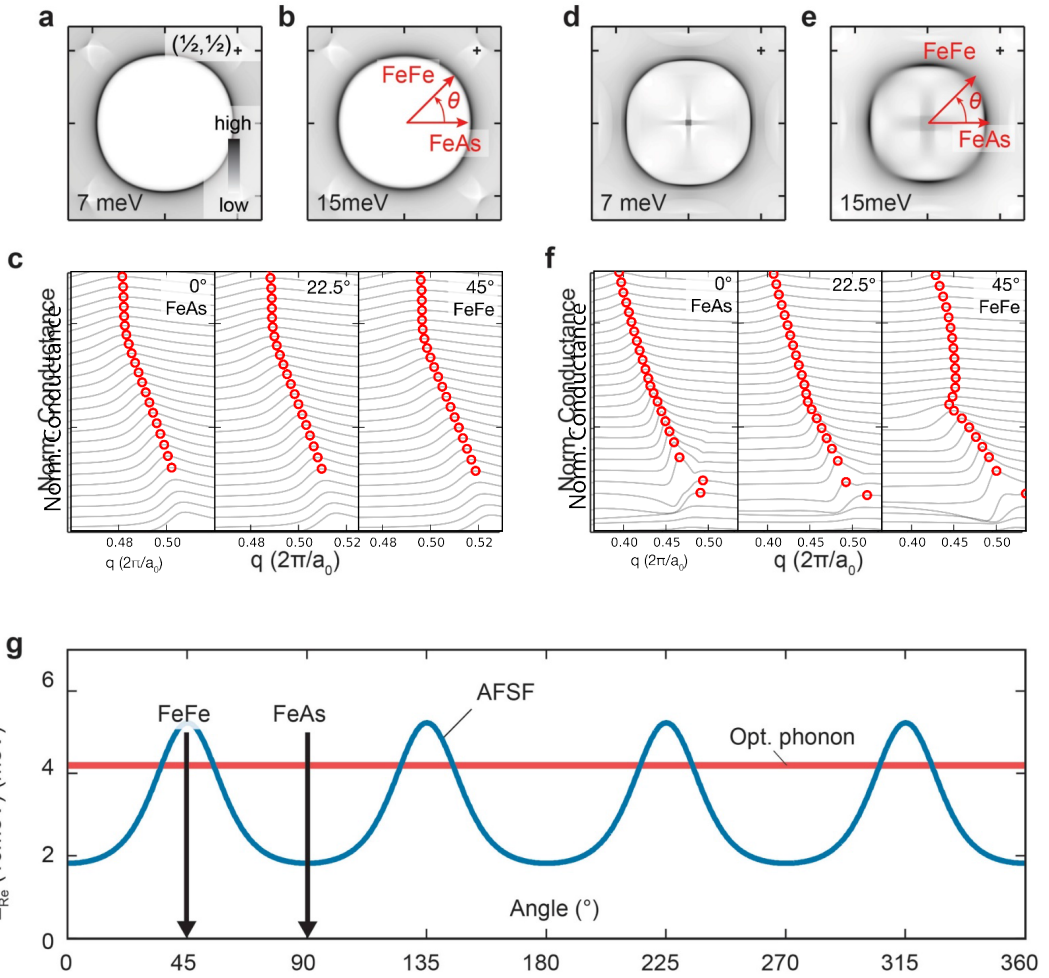


Figure 5.3: 'Fingerprint' distinguishing antiferromagnetic spin fluctuations from phonon generated orbital fluctuations in LiFeAs. (a-c) Predicted QPI response calculated with self-energy driven by the Fe- E_g phonon. (a,b) Sequential images of $g(\mathbf{q}, \omega)$ for two different ω , one below and one near the coupling energy. (c) Predicted $g(\mathbf{q}, \omega)$ in three different directions in \mathbf{q} -space, corresponding to the Fe–As direction (left), the Fe–Fe direction (right) and an intermediate direction (center). Different grey lines correspond to different ω , with a 1 meV increase between each neighbouring pair, starting from the lowest bias $\omega = 0$ at the bottom. The plots are offset for clarity, and the red dots indicate the maxima. The $g(\mathbf{q}, \omega)$ on the γ band remains virtually isotropic, despite the momentum dependence of the electron–phonon coupling in our simulations. (d-f) Predicted QPI response calculated with self-energy driven by resonant AFSF. (d,e) Predicted $g(\mathbf{q}, \omega)$ for the same energies as in a,b. (f) Predicted $g(\mathbf{q}, \omega)$ in three different directions in \mathbf{q} -space, as in c. $g(\mathbf{q}, \omega)$ on the γ band is predicted to be highly anisotropic. (g) Predicted $\text{Re}\Sigma(\mathbf{k}(\omega, \theta), \omega)$ at fixed energy $\omega = 10$ meV calculated with self-energy driven by resonant AFSF (blue) and the Fe- E_g phonon (red) as a function of the angle θ (as defined in b,e) around the γ band.

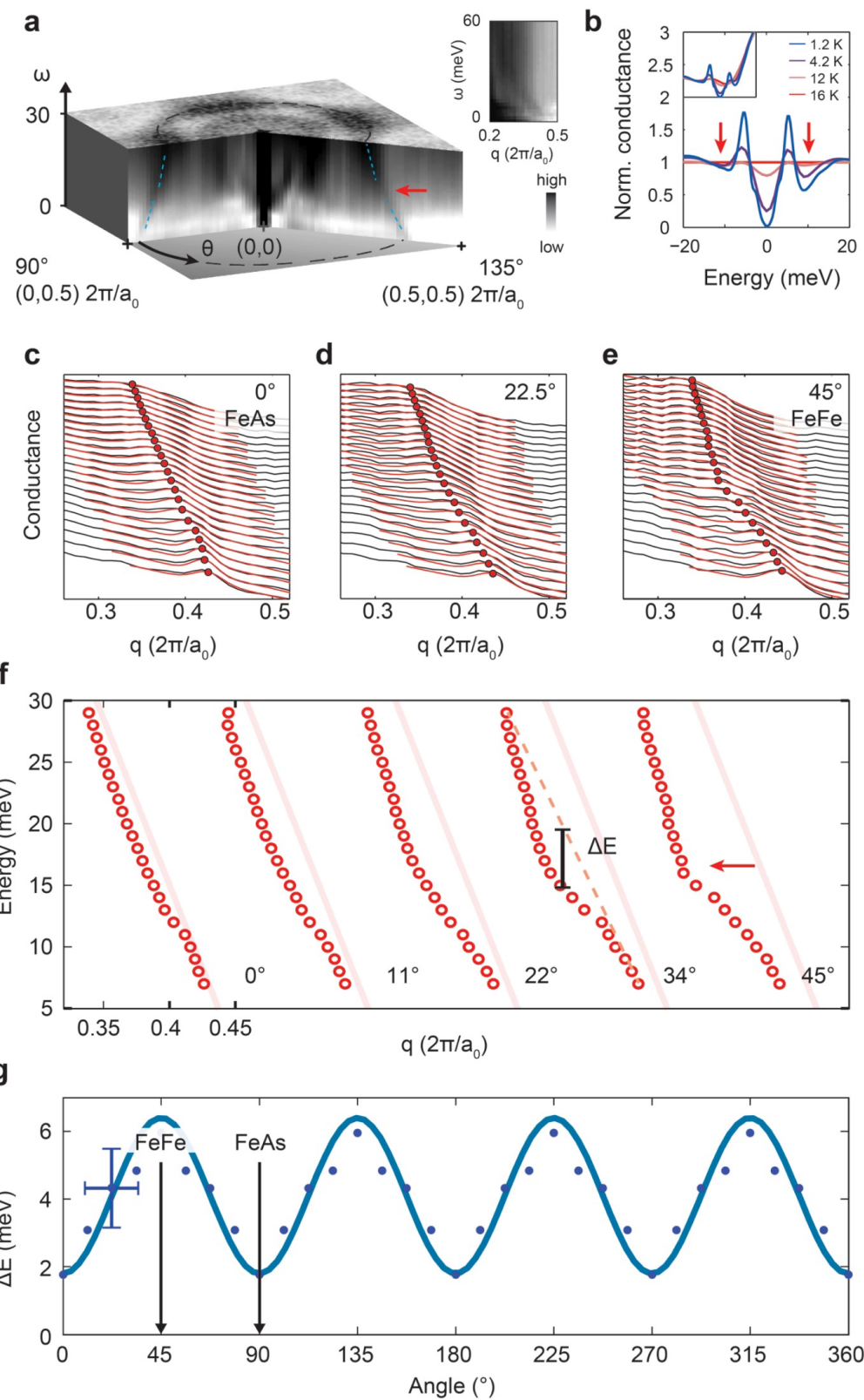


Figure 5.4: QPI measurements of anisotropic renormalization of dispersion due to self-energy in LiFeAs. (a) Measured $g(\mathbf{q}, \omega)$ represented in $\mathbf{q}-\omega$ space for $0 < \omega < 30$ meV, with the $(0, 1)$ and $(1, 1)$ directions highlighted. The inset shows the measured data up to $\omega = 60$ meV. Red arrow indicates the energy $\omega \sim 12$ meV at which sudden changes in dispersion and isotropy of $g(\mathbf{q}, \omega)$ are observed. See Supplementary Movie 1, in which this effect is vivid. (b) The $N(\omega)$ measured simultaneously with $g(\mathbf{q}, \omega)$ and normalized by $N(\omega)$ at $T = 16$ K. Vertical red arrows indicate the energy $\omega \sim 12$ meV at which features associated with Cooper pairing are observed. The inset shows the original $N(\omega) \sim dI/dV(\omega)$. (c–e) Lineplots of measured $g(\mathbf{q}, \omega)$ data for different energies ω along the Fe–As direction (left), the Fe–Fe direction (right) and an intermediate direction (centre). The data at different ω are offset vertically for clarity. The angle indicated is θ measured from the Fe–As direction. (f) Dispersion of the maxima in $g(\mathbf{q}, \omega)$ extracted from line cuts as in (c–e). The angle indicated is θ measured from the Fe–As direction. These dispersions are to be compared with the predictions in Fig. 5.3a–c or Fig. 5.3d–f. (g) Measured ΔE , the departure of the dispersion of the maxima in $g(\mathbf{q}, \omega)$ from a model with no self-energy effect, as a function of the angle θ around the γ band of LiFeAs. This is to be compared with the theoretical prediction in Fig. 5.3g.

Although evidence that self-energy effects due to electron–boson-coupling phenomena are occurring in iron-based materials abounds [18, 26–32], a direct comparison between a theoretical prediction with realistic band/gap structure that distinguishes effects of coupling to AFSF from those due to coupling to E_g -phonons generating the orbital fluctuations, has not been achieved. Here, by combining new theoretical insight into QPI discrimination between $\Sigma(\mathbf{k}, \omega)$ from resonant AFSF and $\Sigma(\mathbf{k}, \omega)$ due to alternative scenarios, together with novel QPI techniques designed to visualize the $\Sigma(\mathbf{k}, \omega)$ signatures [19], we demonstrate that scattering interference at $\omega > \Delta_{\max}$ on the γ band of LiFeAs is highly consistent with expected effects due to AFSF-driven $\Sigma(\mathbf{k}, \omega)$. Crucially the apparent changes in the dispersion (Fig. 5.2 and 5.4) show a strong directional dependence, being focused along

the Fe–Fe direction where the spin fluctuations of LiFeAs are concentrated [23, 33]. This is in excellent qualitative agreement with our predictions based on measured band/gap structures of LiFeAs for resonant-AFSF-driven $\Sigma(\mathbf{k}, \omega)$ effects (Fig. 5.2a–d and 5.3). Further, we demonstrate that such anisotropic $\Sigma(\mathbf{k}, \omega)$ effects studied here cannot be caused by a Fe-E_g phonon (Fig. 5.3a–c). Thus, our combined theoretical/experimental approach to ‘fingerprinting’ the electronic self-energy $\Sigma(\mathbf{k}, \omega)$ discriminates directly between different types of bosonic fluctuations proposed to mediate pairing. In analogy to phonon-based superconductors, this novel approach may lead to a definite identification of the Cooper pairing mechanism of iron-based superconductivity—with the present result pointing strongly to antiferromagnetic spin fluctuations.

BIBLIOGRAPHY

1. Wang, F. & Lee, D.-H. The electron-pairing mechanism of iron-based superconductors. *Science* **332**, 200 (2011).
2. Hirschfeld, P. J., Korshunov, M. M. & Mazin, I. I. Gap symmetry and structure of Fe-based superconductors. *Rep. Prog. Phys.* **74**, 124508 (2011).
3. Scalapino, D. J. A common thread: The pairing interaction for unconventional superconductors. *Rev. Mod. Phys.* **84**, 1383 (2012).
4. Mazin, I. I., Singh, D. J., Johannes, M. D. & Du, M. H. Unconventional superconductivity with a sign reversal in the order parameter of $\text{LaFeAsO}_{1-x}\text{F}_x$. *Phys. Rev. Lett.* **101**, 057003 (2008).
5. Kuroki, K. *et al.* Unconventional pairing originating from the disconnected Fermi surfaces of superconducting $\text{LaFeAsO}_{1-x}\text{F}_x$. *Phys. Rev. Lett.* **101**, 087004 (2008).
6. Stanescu, T. D., Galitski, V. & Das Sarma, S. Orbital fluctuation mechanism for superconductivity in iron-based compounds. *Phys. Rev. B* **78**, 195114 (2008).
7. Kontani, H. & Onari, S. Orbital-fluctuation-mediated superconductivity in iron pnictides: Analysis of the five-orbital Hubbard-Holstein model. *Phys. Rev. Lett.* **104**, 157001 (2010).
8. Zhang, J., Sknepnek, R. & Schmalian, J. Spectral analysis for the iron-based superconductors: Anisotropic spin fluctuations and fully gapped s^\pm -wave superconductivity. *Phys. Rev. B* **82**, 134527 (2010).
9. Heimes, A., Grein, R. & Eschrig, M. Electronic dispersion anomalies in iron pnictide superconductors. *Phys. Rev. Lett.* **106**, 047003 (2011).

10. Heimes, A., Grein, R. & Eschrig, M. Effect of spin fluctuations on the electronic structure in iron-based superconductors. *Phys. Rev. B* **86**, 064528 (2012).
11. Allan, M. P. *et al.* Anisotropic energy gaps of iron-based superconductivity from intraband quasiparticle interference in LiFeAs. *Science* **336**, 563 (2012).
12. Knolle, J. *et al.* Incommensurate magnetic fluctuations and Fermi surface topology in LiFeAs. *Phys. Rev. B* **86**, 174519 (2012).
13. Wray, L. *et al.* Momentum dependence of superconducting gap, strong-coupling dispersion kink, and tightly bound Cooper pairs in the high- T_c $(\text{Sr}, \text{Ba})_{1-x}(\text{K}, \text{Na})_x\text{Fe}_2\text{As}_2$ superconductors. *Phys. Rev. B* **78**, 184508 (2008).
14. Koitzsch, A. *et al.* Temperature and doping-dependent renormalization effects of the low energy electronic structure of $\text{Ba}_{1-x}\text{K}_x\text{Fe}_2\text{As}_2$ single crystals. *Phys. Rev. Lett.* **102**, 167001 (2009).
15. Richard, P. *et al.* Angle-resolved photoemission spectroscopy of the Fe-based $\text{Ba}_{0.6}\text{K}_{0.4}\text{Fe}_2\text{As}_2$ high temperature superconductor: evidence for an orbital selective electron-mode coupling. *Phys. Rev. Lett.* **102**, 047003 (2009).
16. Kordyuk, A. A. *et al.* Angle-resolved photoemission spectroscopy of superconducting LiFeAs: Evidence for strong electron-phonon coupling. *Phys. Rev. B* **83**, 134513 (2011).
17. Borisenko, S. V. *et al.* One-sign order parameter in iron based superconductor. *Symmetry* **4**, 251 (2012).
18. Chi, S. *et al.* Scanning tunneling spectroscopy of superconducting LiFeAs single crystals: Evidence for two nodeless energy gaps and coupling to a bosonic mode. *Phys. Rev. Lett.* **109**, 087002 (2012).

19. Dahm, T. & Scalapino, D. J. Quasi-particle interference probe of the self-energy. *New J. Phys.* **16**, 023003 (2014).
20. Marsiglio, F. & Carbotte, J. P. in *Superconductivity* (eds Bennemann, K. H. & Ketterson, J. B.) chap. 3 (Springer, 2008).
21. Eschrig, H. & Koepernik, K. Tight-binding models for the iron-based superconductors. *Phys. Rev. B* **80**, 104503 (2009).
22. Taylor, A. E. *et al.* Antiferromagnetic spin fluctuations in LiFeAs observed by neutron scattering. *Phys. Rev. B* **83**, 220514 (2011).
23. Qureshi, N. *et al.* Inelastic neutron-scattering measurements of incommensurate magnetic excitations on superconducting LiFeAs single crystals. *Phys. Rev. Lett.* **108**, 117001 (2012).
24. Hajiri, T. *et al.* Three-dimensional electronic structure and interband nesting in the stoichiometric superconductor LiFeAs. *Phys. Rev. B* **85**, 094509 (2012).
25. Umezawa, K. *et al.* Unconventional anisotropic *s*-Wave superconducting gaps of the LiFeAs iron-pnictide superconductor. *Phys. Rev. Lett.* **108**, 037002 (2012).
26. Yang, J. *et al.* Optical spectroscopy of superconducting $\text{Ba}_{0.55}\text{K}_{0.45}\text{Fe}_2\text{As}_2$: Evidence for strong coupling to low-energy bosons. *Phys. Rev. Lett.* **102**, 187003 (2009).
27. Fasano, Y. *et al.* Local quasiparticle density of states of superconducting $\text{SmFeAsO}_{1-x}\text{F}_x$ single crystals: Evidence for spin-mediated pairing. *Phys. Rev. Lett.* **105**, 167005 (2010).
28. Wu, D. *et al.* Eliashberg analysis of optical spectra reveals a strong coupling of charge carriers to spin fluctuations in doped iron-pnictide BaFe_2As_2 superconductors. *Phys. Rev. B* **82**, 144519 (2010).

29. Choi, K.-Y. *et al.* Self-energy effects and electron-phonon coupling in Fe-As superconductors. *J. Phys.: Condens. Matt.* **22**, 115802 (2010).
30. Shamoto, S.-i. *et al.* Inelastic neutron scattering study of the resonance mode in the optimally doped pnictide superconductor LaFeAsO_{0.92}F_{0.08}. *Phys. Rev. B* **82**, 172508 (2010).
31. Shan, L. *et al.* Evidence of a spin resonance mode in the iron-based superconductor Ba_{0.6}K_{0.4}Fe₂As₂ from scanning tunneling spectroscopy. *Phys. Rev. Lett.* **108**, 227002 (2012).
32. Cai, P. *et al.* Visualizing the microscopic coexistence of spin density wave and superconductivity in underdoped NaFe_{1-x}Co_xAs. *Nat. Commun.* **4**, 1596 (2013).
33. Wang, M. *et al.* Antiferromagnetic spin excitations in single crystals of non-superconducting Li_{1-x}FeAs. *Phys. Rev. B* **83**, 220515 (2011).

CHAPTER 6

RESPONSE TO GAUGE FIELD

One of the defining properties of a superconductor is its zero resistivity, i.e., non-zero current flow ($\mathbf{J} \neq 0$) without voltage drop ($\mathbf{E} = 0$). Such *perfect conductivity* is well captured by the equation written down by London [1]

$$\mathbf{J} = -\frac{1}{\Lambda c} \mathbf{A}. \quad (6.1)$$

This non-gauge-invariant equation incorporates the rigidity of the condensate wavefunction. It is not too difficult to show that the BCS paired state satisfies Eq. (6.1) using field theoretical methods [2].

For heterogeneous systems, however, analytical solutions are often not accessible, and one needs to rely on numerical techniques. On discrete lattice models, however, current and gauge field need careful redefinition, since differential operators used in the definition of these cannot be directly applied to a lattice. In this chapter, we discuss how to incorporate gauge field to a lattice Hamiltonian, and also discuss current operators and optical conductivity.

6.1 Peierls Phase

In continuous space, the effect of gauge field \mathbf{A} on a particle with charge q and mass m can be treated through *minimal coupling*

$$\mathcal{K} = \frac{1}{2m} (\mathbf{p} - q\mathbf{A})^2 \quad (6.2)$$

On a lattice system, however, differential operators are not defined. The “minimal coupling” on a lattice which is analogous to that of continuum is through *Peierls*

phase [3], which is in the phase of hoppings

$$t_{\mathbf{x}\mathbf{y}} \rightarrow t_{\mathbf{x}\mathbf{y}} e^{-i\varphi(\mathbf{x},\mathbf{y})} \quad (6.3)$$

The phase $\varphi(\mathbf{x},\mathbf{y})$ can be related to the “physical” gauge field \mathbf{A} of continuum as

$$\varphi(\mathbf{x},\mathbf{y}) = q \int_{\mathbf{y}}^{\mathbf{x}} \mathbf{A} \cdot d\mathbf{r} \quad (6.4)$$

6.2 Current and Superfluid Stiffness

In continuum, the “current density” of a single particle of mass m with wavefunction Ψ is

$$\mathbf{J} = \frac{1}{2mi} [\Psi^* \nabla \Psi - \Psi \nabla \Psi^*] \quad (6.5)$$

On a lattice model, however, this definition of current is not directly applicable. We can nevertheless find the definition of current consistent with the discreteness of the lattice system, using the Peierls phase. Let us consider the case when \mathbf{A} is uniform in space. Given the following non-interacting Hamiltonian

$$\mathcal{H} = \sum_{\alpha\beta} c_{\alpha}^* K_{\alpha\beta} c_{\beta}, \quad \text{where} \quad K_{\alpha\beta} = t_{\alpha\beta} e^{-iq\mathbf{l}_{\alpha\beta} \cdot \mathbf{A}} \quad \text{and} \quad \mathbf{l}_{\alpha\beta} = \int_{\mathbf{x}_{\beta}}^{\mathbf{x}_{\alpha}} d\mathbf{r}. \quad (6.6)$$

Then from the derivative of Hamiltonian with respect to gauge field, we find a definition of current for a lattice model

$$\mathcal{J}^{\mu} = -\frac{1}{\Omega} \frac{\partial \mathcal{H}}{\partial A^{\mu}} = \frac{iq}{\Omega} \sum_{\alpha\beta} c_{\alpha}^* K_{\alpha\beta} \ell_{\alpha\beta}^{\mu} c_{\beta} \quad (6.7)$$

where $\mu = 1, \dots, D$ is an index for spatial dimension.

It is worthwhile to note that this definition of current is consistent with the idea of charge conservation. Since the number (or equivalently, charge) operator

on site α is $n_\alpha = c_\alpha^* c_\alpha$, its equation of motion

$$\frac{dn_\alpha}{dt} = i[\mathcal{H}, n_\alpha] \quad (6.8)$$

gives the following “continuity” equation

$$\frac{dn_\alpha}{dt} = \sum_\beta \mathcal{J}_{\alpha\beta} \quad (6.9)$$

where

$$\mathcal{J}_{\alpha\beta} \equiv -i [c_\alpha^* K_{\alpha\beta} c_\beta - c_\beta^* K_{\beta\alpha} c_\alpha] \quad (6.10)$$

The expression for \mathcal{J}^μ defined from the gauge coupling is related to $\mathcal{J}_{\alpha\beta}$ as follows:

$$\mathcal{J}^\mu = \frac{q}{\Omega} \sum_{\alpha\beta} \mathcal{J}_{\alpha\beta} \ell_{\alpha\beta}^\mu \quad (6.11)$$

In Nambu basis, the normal state Hamiltonian and the current write

$$\mathcal{H} = \frac{1}{2} \sum_{\alpha\beta} \begin{pmatrix} c_\alpha^* & c_\alpha \end{pmatrix} \begin{pmatrix} K_{\alpha\beta} & 0 \\ 0 & -K_{\alpha\beta}^* \end{pmatrix} \begin{pmatrix} c_\beta \\ c_\beta^* \end{pmatrix} \equiv \frac{1}{2} \sum_{\alpha\beta} \psi_\alpha^\dagger H_{\alpha\beta} c_\beta \quad (6.12)$$

$$\mathcal{J}^\mu = \frac{iq}{2\Omega} \sum_{\alpha\beta} \begin{pmatrix} c_\alpha^* & c_\alpha \end{pmatrix} \begin{pmatrix} K_{\alpha\beta} \ell_{\alpha\beta}^\mu & 0 \\ 0 & K_{\alpha\beta}^* \ell_{\alpha\beta}^\mu \end{pmatrix} \begin{pmatrix} c_\beta \\ c_\beta^* \end{pmatrix} \equiv \frac{1}{2} \sum_{\alpha\beta} \psi_\alpha^\dagger J_{\alpha\beta}^\mu c_\beta \quad (6.13)$$

In the superconducting state, pairing term ($\Delta c^* c^*$) in BCS Hamiltonian nominally breaks the charge conservation, the notion of “current” presented above also breaks down. Noted earlier as the “gauge invariance problem,” which results in unphysical longitudinal current in the BCS paired state, this problem was studied by Bardeen [4], Anderson [5, 6], and Rickayzen [7]. While there are various ways to solve this problem using field theoretical techniques [2], one way to resolve this issue is to remember that the pairing term is a mean-field approximation to the interacting Hamiltonian which indeed conserve charge. Therefore, while using

the definition of current in Eq. (6.13), by self-consistently determining Δ for every given \mathbf{A} , one is able to get around the gauge invariance problem.

In numerical calculation, therefore, we can simply introduce a small but nonzero A^μ to the system, and measure the current \mathcal{J}^μ . From this we can extract the *superfluid stiffness* ρ_s as

$$\langle \mathcal{J}^\mu \rangle = - \sum_v [\rho_s]_{\mu v} A^v \quad (6.14)$$

6.3 Optical Conductivity

In addition to superfluid density, which is a “static” response of a superconductor, optical conductivity, which is a “dynamical” response, can also be measured through time-dependent electric field. The retarded current-current correlator, following Appendix A, is

$$\chi_{\mu\nu}^R(\omega) = -\frac{q^2}{4\Omega} \sum_{nm} \langle n | \mathcal{J}^\mu | m \rangle \langle m | \mathcal{J}^\nu | n \rangle \frac{f_D(E_m) - f_D(E_n)}{\omega + i\eta + E_m - E_n} \quad (6.15)$$

and therefore the relationship between current and gauge field is

$$\mathcal{J}^\mu(\omega) = \sum_v \chi_{\mu v}^R(\omega) A^v(\omega) \quad (6.16)$$

The (optical) conductivity, however, is defined as the system’s response to electric field $\mathbf{E} = -\partial\mathbf{A}/\partial t$. Therefore, for $\mathbf{A}(t) = \mathbf{A}_0 e^{-i\omega t}$,

$$\mathcal{J}^\mu(\omega) = \sum_v \frac{\chi_{\mu v}^R(\omega)}{i\omega} E^v(\omega) \quad (6.17)$$

Therefore, the optical conductivity σ can be written in spectral representation as

$$\sigma_{\mu\nu}^R(\omega) = i \frac{q^2}{4\Omega\omega} \sum_{nm} \langle n | \mathcal{J}^\mu | m \rangle \langle m | \mathcal{J}^\nu | n \rangle \frac{f_D(E_m) - f_D(E_n)}{\omega + i\eta + E_m - E_n}. \quad (6.18)$$

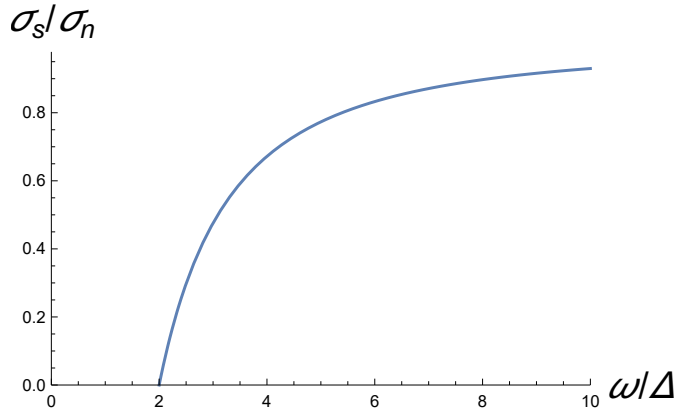


Figure 6.1: The ratio between the real part of optical conductivity in the superconducting state ($\sigma_s(\omega)$) and normal state ($\sigma_n(\omega)$), calculated within Mattis-Bardeen theory at zero temperature.

Especially, the real part of optical conductivity can be written as Fermi-golden-rule-like form:

$$\text{Re}\sigma_{\mu\nu}^R = \frac{\pi q^2}{4\Omega\omega} \sum_{nm} \langle n | \mathcal{J}^\mu | m \rangle \langle m | \mathcal{J}^\nu | n \rangle [f_D(E_m) - f_D(E_n)] \delta(\omega + E_m - E_n). \quad (6.19)$$

Equation 6.18 can be used to derive the Mattis-Bardeen expression for optical conductivity, which was first proposed to explain the anomalous skin effect of superconducting metals [8]. Within Mattis-Bardeen theory, the ratio between optical conductivities in the superconducting and normal states can be written as

$$\begin{aligned} \frac{\text{Re}\sigma_s}{\text{Re}\sigma_n} &= \frac{2}{\omega} \int_{\Delta}^{\infty} dE \frac{|E(E+\omega) + \Delta^2| [f(E) - f(E+\omega)]}{(E^2 - \Delta^2)^{1/2} [(E+\omega)^2 - \Delta^2]^{1/2}} \\ &\quad + \frac{1}{\omega} \int_{-\Delta}^{-\Delta} dE \frac{|E(E+\omega) + \Delta^2| [1 - 2f(E+\omega)]}{(E^2 - \Delta^2)^{1/2} [(E+\omega)^2 - \Delta^2]^{1/2}} \end{aligned} \quad (6.20)$$

Note that the above expression is valid for moderate disorder strength, i.e. $\Delta \ll 1/\tau$, where τ is the lifetime of quasiparticles in the normal state. At zero temperature, the optical conductivity shows a gap below 2Δ (Fig. 6.1), indicating the lack of excitonic excitations with energy less than 2Δ . This is a direct consequence of the superconducting gap Δ .

BIBLIOGRAPHY

1. London, F. On the problem of the molecular theory of superconductivity. *Phys. Rev.* **74**, 562 (1948).
2. Schrieffer, J. R. *Theory of superconductivity* Revised ed. (Perseus Books, 1999).
3. Peierls, R. Zur Theorie des Diamagnetismus von Leitungselektronen. *Z. Phys.* **80**, 763 (1933).
4. Bardeen, J. Gauge invariance and the energy gap model of superconductivity. *Il Nuovo Cimento* **5**, 1766 (1957).
5. Anderson, P. W. Coherent excited states in the theory of superconductivity: Gauge invariance and the Meissner effect. *Phys. Rev.* **110**, 827 (1958).
6. Anderson, P. W. Random-phase approximation in the theory of superconductivity. *Phys. Rev.* **112**, 1900 (1958).
7. Rickayzen, G. Collective excitations in the theory of superconductivity. *Phys. Rev.* **115**, 795 (1959).
8. Mattis, D. C. & Bardeen, J. Theory of the anomalous skin effect in normal and superconducting metals. *Phys. Rev.* **111**, 412 (1958).

CHAPTER 7

RESEARCH PAPER:

COLD-SPOTS AND GLASSY NEMATICITY IN UNDERDOPED CUPRATES

Kyungmin Lee¹, Steven A. Kivelson², and Eun-Ah Kim¹

¹*Department of Physics, Cornell University, Ithaca, New York 14853, USA.*

²*Department of Physics, Stanford University, Stanford, California 94305, USA.*

Published on Physical Review B **94**, 014204 (2016).

Abstract

There is now copious direct experimental evidence of various forms of (short-range) charge order in underdoped cuprate high temperature superconductors, and spectroscopic signatures of a nodal-antinodal dichotomy in the structure of the single-particle spectral functions. In this context, we analyze the Bogoliubov quasiparticle spectrum in a superconducting nematic glass. The coincidence of the superconducting “nodal points” and the nematic “cold-spots” on the Fermi surface naturally accounts for many of the most salient features of the measured spectral functions (from angle-resolved photoemission) and the local density of states (from scanning tunneling microscopy).

7.1 Introduction

The existence of glassy charge order in the pseudogap phase of cuprates is now well established: Both momentum space and real space probes find charge-density-wave (CDW) order with moderate (but never infinite) correlation lengths [1–11]. Evidence of a tendency to nematic order has been adduced from local probes [12–14], diffraction [15, 16], and transport [17, 18]. Much of the associated theory literature has focused on either uniform long-range ordered states, or dynamically fluctuating order. In contrast, glassy order implies strong static heterogeneities, which complicate any theoretical analysis.

The basic superconducting state is thought to be reasonably well described by a simple mean-field theory with a d -wave superconducting gap. Nevertheless, when the superconductivity coexists with glassy charge order, spectroscopic measurements reveal a number of “anomalous” features that are not simply related to any long-range order. It is thus worth asking whether some or all of these anomalous features are a consequence of glassy charge order. Heterogeneous order parameters have been studied previously in the context of cuprates [19–26]. But most of these works have focused on the effects of quenched randomness (e.g., impurities) on the ordering tendencies themselves. Here instead we study how the heterogeneity associated with glassy order affects various spectroscopic properties.

Technically, our approach is similar to that employed in earlier works on the effects of point-like impurities [27–32]. However, because the glassy order is assumed to reflect (in part) the system’s tendency toward symmetry breaking, in the present study the effective scattering (“disorder”) potential is taken to have two properties not present in earlier studies: (1) a moderate correlation length, and (2)

a non-trivial form factor. Although we do consider various forms of CDW order, our most extensive and most significant results are associated with a nematic glass, which by symmetry has a *d*-wave form factor. While the lack of translation symmetry destroys the long range coherence of the quasiparticles, the *d*-wave form factor gives rise [33–35] to cold-spots [36], near which the quasiparticles are increasingly weakly coupled to the glassy order. Because these cold-spots coincide with the nodal points in a *d*-wave superconductor, the lowest energy quasiparticles are also the most weakly affected by the nematic glass.

In comparing our results to experiment, we consider features from three different experiments: angle-resolved photomission spectroscopy (ARPES), scanning tunneling microscopy (STM), and optical measurements:

(1) The most salient feature of ARPES that we address is the “nodal-antinodal” dichotomy. The energy distribution curves (EDCs) for momenta along a cut across the Fermi surface [Fig. 7.1(b)] in the nodal region consist of a single dispersing feature which at least roughly resembles that expected of a quasiparticle with a finite lifetime. Conversely, along a similar cut perpendicular to the antinodal segment of the Fermi surface [Fig. 7.1(c)], the EDC is complex, exhibiting at least two distinct features with apparent dispersion relations (if that notion applies at all) that appear almost discontinuous. Nevertheless, moving along the Fermi surface from the nodal to the antinodal point, the EDC curves evolve smoothly and monotonically [Fig. 7.1(d)] with no sign of any sharp boundary, or of the non-monotonic behavior one would expect if there were “hot-spots” on the Fermi surface corresponding to the spanning vectors associated with incipient density-wave order.

(2) Much thought has gone into the analysis of the rich structural and spectroscopic information encoded in the variations of the local density of states (LDOS)

measured by STM, especially on BSCCO. Here we focus exclusively on a clear “dichotomy” [Fig. 7.4(a)] that has been apparent since the earliest studies [37–39]: At relatively low energies, the LDOS is remarkably homogeneous and has the V-shaped energy dependence expected for a uniform d -wave superconductor, while at energies comparable to the gap (or pseudo-gap), there are order one variations of the LDOS as a function of position. Note that the “dispersing features” in the Fourier transform of the LDOS which have been identified with quasiparticle interference effects are more or less confined to the “low energy” range in which the LDOS is relatively homogeneous.

(3) The low T optical conductivity rises roughly linearly with increasing frequency ω to a peak at $\omega \sim 100 - 200\text{meV}$ that (at least in the more recent data on Hg-1201) is larger than any reasonable estimate of the superconducting gap, and then drops slowly at larger ω [Fig. 7.6(a) and 7.6(b)]. All of these features are somewhat anomalous, as is the T dependence of $\sigma(\omega)$.

As we shall show, these salient features of the ARPES and STM experiments are naturally explained by the coincidence of the nematic cold-spots and the superconducting nodes in a superconducting nematic glass. This is illustrated in Figs. 7.2 and 7.4(b), respectively. We also find that the optical conductivity computed in the simplest model of such a glass looks remarkably like the experiments [Fig. 7.6(c)]. However, concerning the thermal evolution of σ , there are aspects of the solution that are slightly problematic, since in making the comparison at the higher temperatures, we are comparing experimental results at $T > T_c$ with theoretical results at $T < T_c$.

The notion that various phenomena in the cuprates may be associated with the existence of cold-spots on the Fermi surface is not new. Notably, a number of

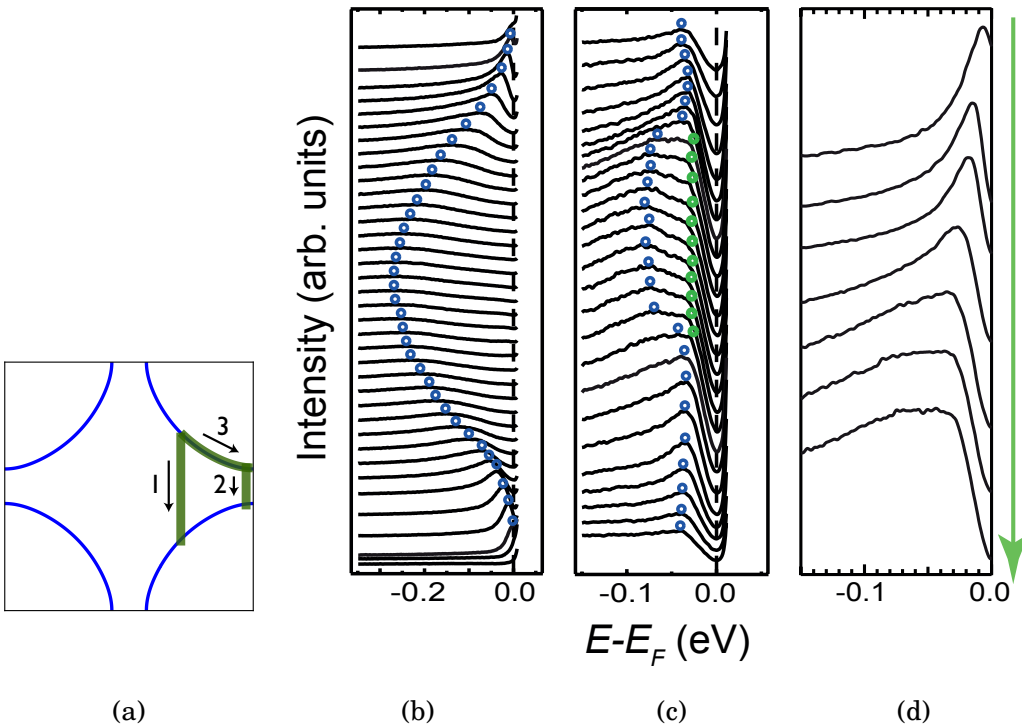


Figure 7.1: Energy distribution curves (EDCs) from ARPES measurements reproduced from He et al. [40](Bi-2201). (b)–(d) Different paths in \mathbf{k} -space as shown in (a): (b) is a “nodal” cut through the Fermi surface [path 1 of (a)], (c) is an antinodal cut through the Fermi surface [path 2 of (a)], and (d) is a path along the Fermi surface starting at the nodal point and ending at the antinodal [path 3 of (a)]. The measured spectral weight has been divided by the Fermi function.

earlier studies [36, 41–46] have suggested that salient features of the transport properties of the “normal” (“bad metal” or “strange metal”) state can be interpreted as evidence of a strongly anisotropic scattering rate on the Fermi surface, with cold-spots along the zone diagonal. Anisotropic scattering rates inferred from ARPES data supports the case [47]. In contrast, in the present study, the focus is primarily on the low temperature properties of the system where superconductivity and pseudo-gap signatures coexist. In this regime, glassy nematicity provides a plausible microscopic origin of anisotropic scattering rates. To the extent that there is a relation to the cold-spots of the earlier proposals, it is more likely that at higher doping and larger temperature they are associated with quantum or ther-

mal nematic fluctuations [48–50], rather than with frozen, glassy nematic order.

7.2 The Model

As our primary focus is on the quasiparticle properties deep in the superconducting state and far from any quantum phase transition, where neither thermal nor quantum fluctuations are expected to be significant, we assume that it is sufficient to study the solutions of an appropriate mean-field Bogoliubov-de Gennes Hamiltonian,

$$H_{\text{BdG}} = \sum_{\mathbf{xy}} \begin{pmatrix} c_{\mathbf{x}\uparrow}^\dagger & c_{\mathbf{x}\downarrow} \end{pmatrix} \begin{pmatrix} t_{\mathbf{xy}} & \Delta_{\mathbf{xy}} \\ \Delta_{\mathbf{yx}}^* & -t_{\mathbf{yx}} \end{pmatrix} \begin{pmatrix} c_{\mathbf{y}\uparrow} \\ c_{\mathbf{y}\downarrow}^\dagger \end{pmatrix}, \quad (7.1)$$

where $c_{\mathbf{x}\sigma}$ annihilates an electron at site \mathbf{x} with spin σ . The “normal” part of the Hamiltonian is assumed to be of the form

$$t_{\mathbf{xy}} = t_{\mathbf{xy}}^{(0)} + V(\mathbf{x}, \mathbf{y}), \quad (7.2)$$

where the first term represents the underlying band-structure, $t_{\mathbf{xy}}^{(0)} = -\mu\delta_{\mathbf{xy}} - t\delta_{\langle\mathbf{x}, \mathbf{y}\rangle} - t'\delta_{\langle\langle\mathbf{x}, \mathbf{y}\rangle\rangle}$, with $t = 1$, $t' = -0.3$, and chemical potential $\mu = -0.8$, and the term V represents the effective potential due to the presence of (glassy) charge order. The anomalous term $\Delta_{\mathbf{xy}}$ on each pair of nearest-neighbor sites $\langle\mathbf{x}, \mathbf{y}\rangle$ is determined self-consistently from the gap equation

$$\Delta_{\mathbf{xy}} = \frac{U}{2} \left\langle c_{\mathbf{y}\uparrow} c_{\mathbf{x}\downarrow} + c_{\mathbf{x}\uparrow} c_{\mathbf{y}\downarrow} \right\rangle, \quad (7.3)$$

with $\Delta_{\mathbf{xy}} = 0$ otherwise. A value of $U = 0.732t$ is chosen so that in the clean limit [$V(\mathbf{x}, \mathbf{y}) = 0$], the transition to the d -wave superconducting state occurs at $T_c^0 = 0.05t$, and the resulting uniform d -wave BCS ground state has a gap-function in \mathbf{k} space: $\Delta_{\mathbf{k}} = \Delta_0(\cos k_x - \cos k_y)$ with $\Delta_0 = 0.055t$. [Note that this unrealistic pairing

strength was chosen such that the antinodal gap ($\sim 0.1t$) is larger than the energy resolution set by $v_F^{\max}\Delta k \sim 0.06t$, where v_F^{\max} is the maximum Fermi velocity, and $\Delta k = 2\pi/N$ is the momentum resolution, for system size $N = 256$ used in most calculations, and yet reasonably smaller than the energy difference between the Fermi level and van Hove singularity ($\Delta E_{vH} = 0.4t$).]

Finally, the effect of any (glassy) charge order is represented by a local order parameter, $\varphi(\mathbf{x})$, (taken to be real under the assumption that time-reversal symmetry is unbroken), which couples to the quasiparticles with a “form factor” $f(\mathbf{r})$:

$$V(\mathbf{x}, \mathbf{y}) = \frac{1}{2}f(\mathbf{x} - \mathbf{y})[\varphi(\mathbf{x}) + \varphi(\mathbf{y})]. \quad (7.4)$$

For typical random disorder, or for the simplest forms of charge-density-wave (CDW) order, $f(\mathbf{r}) \approx \delta_{\mathbf{r}, \mathbf{0}}$, corresponding to a position-dependent single-site energy. In contrast, for nematic order, $f(\mathbf{r})$ must flip sign under 90° rotation by symmetry; to be explicit we choose the shortest-range form factor compatible with nematic symmetry, $f(\mathbf{r}) = \delta_{\mathbf{r}, \pm \hat{x}} - \delta_{\mathbf{r}, \pm \hat{y}}$, corresponding to a position dependent modulation of the nearest-neighbor hopping matrix elements. We assume $\varphi(\mathbf{x})$ are random variables chosen from an ensemble defined by the configuration average of the two-point correlator, $\overline{\varphi(\mathbf{x})\varphi(\mathbf{x} + \mathbf{r})} = \Gamma(\mathbf{r})$. The spatial range of the assumed correlations, as well as any tendency to ordering with non-zero period (as in a CDW with a finite ordering vector \mathbf{Q}) are encoded in $\Gamma(\mathbf{r})$. In the case of a nematic glass, we take $\Gamma(\mathbf{r}) = \Gamma_{\text{nem}} \exp(-r^2/2\xi_{\text{nem}}^2)$, where Γ_{nem} is a measure of the mean-square magnitude of the nematic order, and ξ_{nem} is the nematic correlation length. For a CDW glass, $\Gamma(\mathbf{r}) = (\Gamma_{\text{cdw}}/2)[\cos(\mathbf{Q} \cdot \mathbf{r}) + \cos(\mathbf{Q}' \cdot \mathbf{r})]\exp(-r^2/2\xi_{\text{cdw}}^2)$ where \mathbf{Q} and \mathbf{Q}' are the two symmetry related ordering vectors.

We can already see how a glassy nematic will generate cold-spots by simply

Fourier transforming Eq. (7.4) to yield

$$\tilde{V}(\mathbf{k}, \mathbf{p}) = \frac{1}{2} [\tilde{f}(\mathbf{k}) + \tilde{f}(\mathbf{p})] \tilde{\varphi}(\mathbf{k} - \mathbf{p}), \quad (7.5)$$

where $\tilde{f}(\mathbf{k})$ and $\tilde{\varphi}(\mathbf{q})$ are respective Fourier transforms of $f(\mathbf{r})$ and $\varphi(\mathbf{x})$. For nematic order, $\tilde{f}(\mathbf{k}) = 2(\cos k_x - \cos k_y)$. When $\varphi(\mathbf{x})$ is uniform, $\tilde{\varphi}(\mathbf{q})$ is a delta function peaked at $\mathbf{q} = 0$, in which case \tilde{V} simply leads to distortion of Fermi surface [dashed line in Fig. 7.3(a)]. When $\varphi(\mathbf{x})$ is non-uniform, on the other hand, $\tilde{\varphi}(\mathbf{q})$ is no longer a delta function, and momentum states acquire lifetimes by scattering off of $\tilde{\varphi}(\mathbf{q})$. The form factor $\tilde{f}(\mathbf{k})$ gives rise to strong anisotropy of the quasiparticle lifetimes: While the antinodal quasiparticles are strongly scattered, the “nodal quasiparticles” at the cold-spots ($|k_x| = |k_y|$) are largely unaffected. The cold-spots arise solely as a result of the symmetry of the (local) nematic order.

7.3 Method of Solution

To achieve sufficiently fine \mathbf{k} -space resolution for present purposes, we work with a system with periodic boundary conditions of size $N \times N$ with $N = 128$ or where needed $N = 256$ or 512 . However, because it is computationally intensive to solve the self-consistency equations for such a large system, we have chosen the disorder potential $V(\mathbf{x}, \mathbf{y})$ (and correspondingly $\Delta_{\mathbf{xy}}$) to be periodically repeated in blocks of size $L \times L$ with $L = 32$. This compromise allows us to study real-space heterogeneity, while at the same time reducing the finite size effect through fine \mathbf{k} -space (and hence energy) resolution.

We generate a configuration of the quenched variables by choosing $\{\varphi(\mathbf{x})\}$ from a distribution with a Gaussian two-point correlator $\Gamma(\mathbf{r})$. To avoid long-range correlation of $\varphi(\mathbf{x})$, we choose ξ_{nem} to be small relative to the size of the repeated

blocks. Specifically, we require $|\Gamma(\mathbf{r})/\Gamma(0)| < 1\%$ at $|\mathbf{r}| = La/2$, where a is the lattice constant, which means we are limited to $\xi_{\text{nem}} \leq 5a$. To be concrete, we will present results primarily for $\xi_{\text{nem}} = 2a$; although this is shorter than typical correlation lengths of glassy order measured in experiments (as defined in Ref. [20] for example), we chose it for two reasons: (1) As we will find in our spectral function analyses, $\xi_{\text{nem}} = 2a$ results show qualitatively no difference with $\xi_{\text{nem}} = 4a$. (2) Obviously, results for short correlation lengths suffer less from finite size effect than longer correlation lengths. For each configuration of $\{\varphi(\mathbf{x})\}$, we determine the values of $\Delta_{\mathbf{xy}}$ from the solution of the self-consistency equation Eq. (7.3). For example, a typical configuration of $\varphi(\mathbf{x})$ is shown in Fig. 7.5(a) generated from an ensemble with $\sqrt{\Gamma_{\text{nem}}} = 0.1t$ and $\xi_{\text{nem}} = 2a$; the corresponding self-consistently determined gap function $\Delta_{\mathbf{xy}}$ is shown in Fig. 7.5(b). While there are clearly significant variations in the magnitude of the pair-fields from place to place, the *d*-wave character of the sign structure is universally preserved; it is positive on all *x*-directed and negative on all *y*-directed bonds.

Finally, once self-consistency is achieved, we calculate three spectroscopic observables: (1) the ARPES spectral function $A(\mathbf{k}, E)$, (2) the local density of states $n(\mathbf{x}, E)$, and (3) the optical conductivity $\sigma(\omega)$. The spectroscopic observables we study are self-averaging properties. Although here we present results from a single configuration, we have confirmed that different configurations of $\{\varphi(\mathbf{x})\}$ generated probabilistically from the same distribution result in minor quantitative changes in the calculated spectra, with no significant qualitative difference.

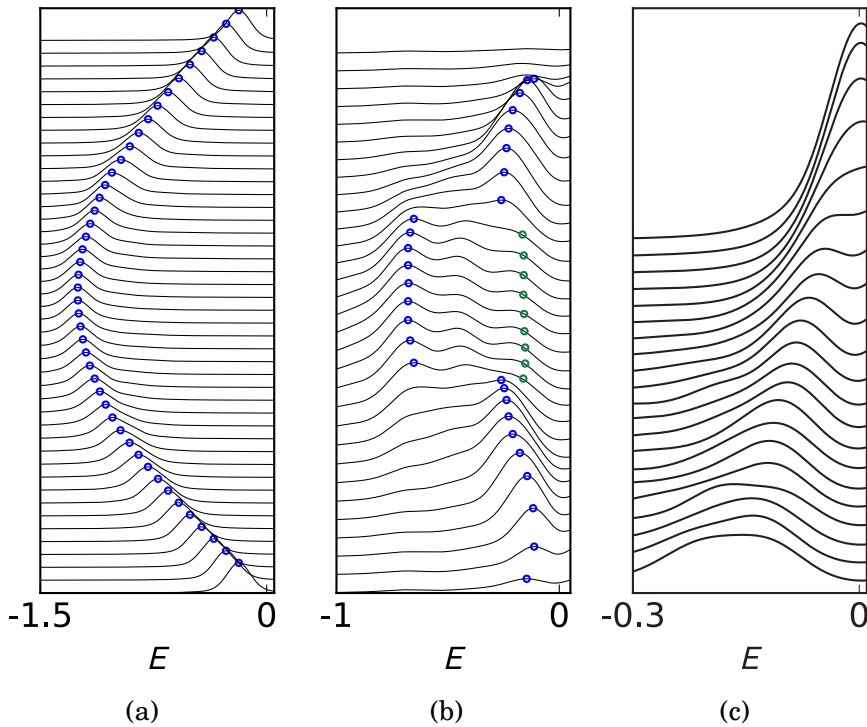


Figure 7.2: EDC's computed along the same paths in \mathbf{k} -space as shown in Fig. 1a for a superconducting nematic glass with $\Delta_0 = 0.055t$, $\sqrt{\Gamma_{\text{nem}}} = 0.1t$, and $\xi_{\text{nem}} = 2a$: (a) is a “nodal” cut through the Fermi surface [path 1 of Fig. 7.1(a)], and (b) is an antinodal cut through the Fermi surface [path 2 of Fig. 7.1(a)]. A blue circle marks the maximum of each curve, and a green circle marks the position of a “shoulder”. (c) is a path along the Fermi surface starting at the nodal point and ending at the antinodal point [path 3 of Fig. 7.1(a)].

7.4 Results for the superconducting nematic glass

Among various forms of glassy charge order that we have considered, the nematic glass best reproduces the nodal-antinodal dichotomy as observed in ARPES (Fig. 7.1). We have carried out calculations for various choices of the strength and correlation length of the nematic order, but to be concrete we present representative data corresponding to $\sqrt{\Gamma_{\text{nem}}} = 0.1t$ and $\xi_{\text{nem}} = 2a$. In Fig. 7.2 we show our results for the spectral function, such as would be measured in ARPES. In Fig. 7.2a, the EDCs (i.e. the energy dependence of $A(\mathbf{k}, E)$ at fixed \mathbf{k}) for \mathbf{k} 's along

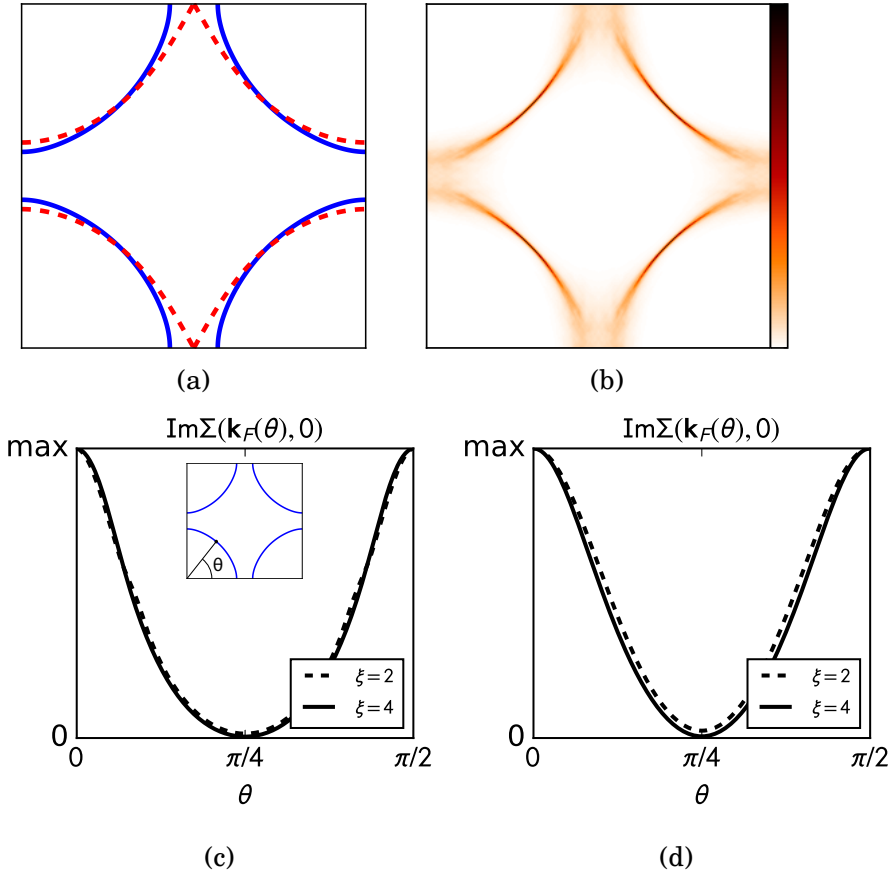


Figure 7.3: (a) Fermi surface of the model system in the normal state ($\Delta_{xy} = 0$). Solid lines are computed in the symmetric phase ($\varphi(\mathbf{x}) = 0$) and the dashed lines in a uniform nematic phase ($\varphi(\mathbf{x}) = 0.05t$.) (b) $A(\mathbf{k}, E)$ of the superconducting nematic glass at a fixed energy $|E| = -0.2t > 2\Delta_0 = 0.11t$ showing the nodal antinodal dichotomy. Color intensity indicates the magnitude. (c) Imaginary part of normal state electronic $\omega = 0$ self-energy on the Fermi surface coupled to nematic order extracted from real space simulation as a function of angle around the Fermi surface θ as defined in the inset, and (d) calculated in the Born approximation.

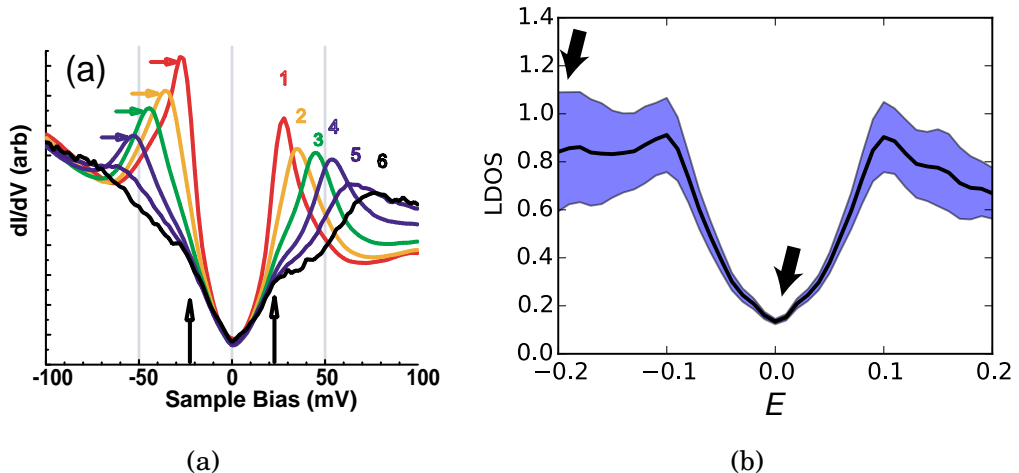


Figure 7.4: Local density of states as a function of energy measured at multiple locations on the surface: (a) Results of STM measurements on Bi-2212 reproduced from Ref. [51]. Different curves represent tunneling spectra measured at different locations of the sample. (b) Computed for a superconducting nematic glass with $\Delta_0 = 0.055t$, $\sqrt{\Gamma_{\text{nem}}} = 0.1t$, and $\xi_{\text{nem}} = 2a$; the solid black curve and the shaded region indicate the spatially averaged DOS and spatial standard deviation of LDOS, respectively. The spatial maps of LDOS at energies marked by the two arrows are shown in Figs. 7.5(c) and 7.5(d).

a cut through the nodal point on the Fermi surface shows a quasiparticle-like dispersion that is otherwise featureless, as in ARPES measurements [Fig. 7.1(b)]. On the other hand, the EDCs in the antinodal region, shown in Fig. 7.2(b), have two branches which are almost discontinuous, a quasiparticle dispersion and a shoulder fixed at the superconducting gap scale, reminiscent of Fig. 7.1(c). EDCs along the Fermi surface from node to antinode [Fig. 7.2(c)] also qualitatively agree with the ARPES measurements [Fig. 7.1(d)]; a sharp peak smoothly and monotonically evolves to a broader peak, albeit this broadening is more pronounced in the theoretical curves than in experiment.

In a long-range ordered nematic phase, the Fermi surface is increasingly deformed as one moves away from the nodes towards the antinodes [see Fig. 7.3(a)]. A related anisotropy characterizes the glassy nematic state, even in the presence

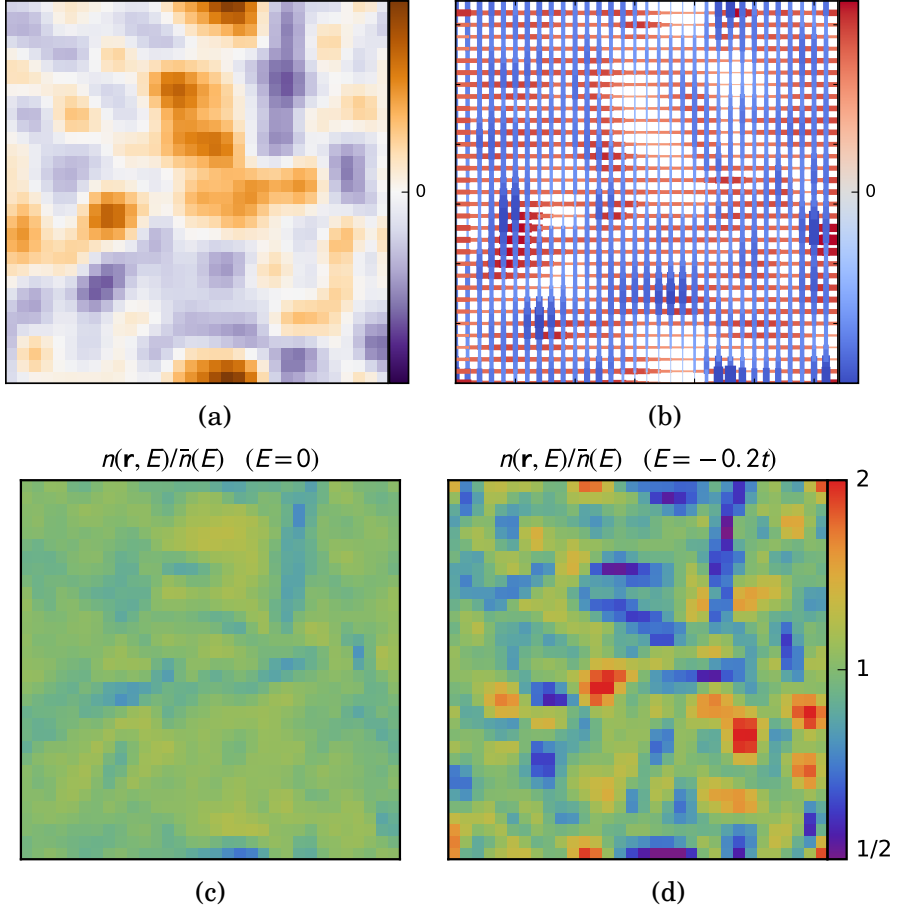


Figure 7.5: (a) A representative configuration of $\varphi(\mathbf{x})$ representing a nematic glass with $\xi_{\text{nem}} = 2a$ in a system of size 32×32 unit cells. (b) The gap parameter, $\Delta_{\mathbf{xy}}$, at $T = 0$ determined self-consistently with $\varphi(\mathbf{x})$ shown in Fig. 7.5(a) when the root-mean-square magnitude $\sqrt{\Gamma_{\text{nem}}} = 0.1t$. The sign of $\Delta_{\mathbf{xy}}$ on each bond is represented by the color (red is positive blue is negative) with the magnitude represented by the thickness of the line as well as opacity. Manifestly, the local symmetry of the pairing is uniformly d -wave. The associated normalized LDOS $n(\mathbf{x}, E)/\bar{n}(E)$, is shown for (c) $E = 0$ and (d) $E = -0.2t$.

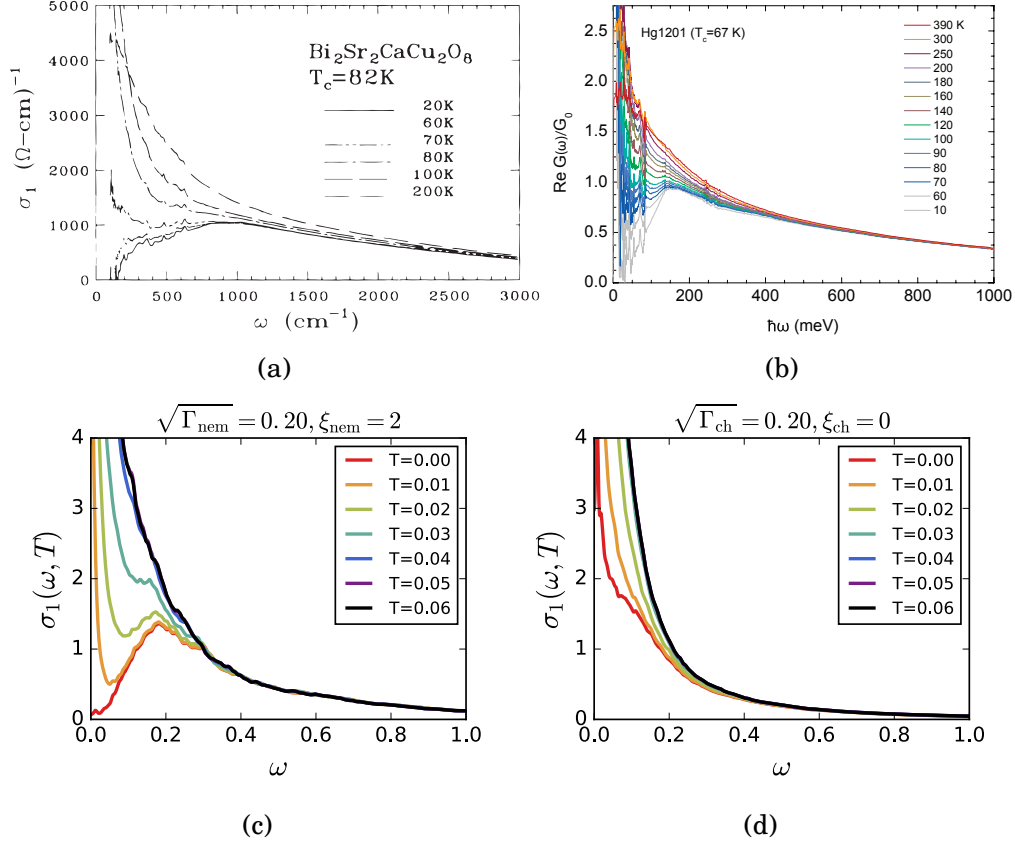


Figure 7.6: Optical conductivity (a) from experiment (Ref. [52]) on Bi-2212 with $T_c = 82\text{K}$, (b) from experiment (Ref. [53]) on Hg-1201 with $T_c = 67\text{K}$, (c) calculated for the superconducting nematic glass with $\xi_{\text{nem}} = 2a$ and $\sqrt{\Gamma_{\text{nem}}} = 0.2t$, and (d) calculated for a disordered superconductor, where the disorder is assumed to have an on-site s -wave form factor with $\xi_{\text{ch}} = 0$ and $\sqrt{\Gamma_{\text{ch}}} = 0.2t$. In both (c) and (d), $\Delta_{\mathbf{xy}}$ is self-consistently determined by Eq. 7.3 with $U = 0.732t$.

of a superconducting gap. Constant-energy cuts of $A(\mathbf{k}, E)$ for a fixed E well above the superconducting gap scale ($E = -0.2t \approx -4\Delta_0$) shown in Fig. 7.3(b) vividly capture the contrast between the nodal and antinodal regions. The spectral function is relatively sharp in the nodal region and significantly broadened in the antinodal region.

The corresponding anisotropy is clearly reflected in the imaginary part of the electron self-energy, i.e. the inverse lifetime of the quasiparticles, extracted from

the calculated spectral function in the normal (non-superconducting) state of the nematic glass, as shown in Fig. 7.3(c). Moreover, results for two different correlation lengths $\xi_{\text{nem}} = 2a$ and $4a$ appear almost identical in their angular dependence; this confirms that our principal qualitative results are robust, despite the short correlation lengths we have assumed for computational simplicity. Indeed, we find that the exact self-energy extracted from our simulation is qualitatively similar to the self-energy computed in Born approximation:

$$\Sigma(\mathbf{k}, \omega) = \int \frac{d^2 p}{(2\pi)^2} |g(\mathbf{k}, \mathbf{p})|^2 G(\mathbf{p}, \omega) \Gamma(\mathbf{p} - \mathbf{k}) \quad (7.6)$$

where $g(\mathbf{k}, \mathbf{p}) \equiv [\tilde{f}(\mathbf{k}) + \tilde{f}(\mathbf{p})]/2$, as shown in Fig. 7.3d.

The energy dependence of the LDOS calculated for the glassy nematic configuration Figs. 7.5(a) and 7.5(b) is shown in Fig. 7.4(b); it exhibits qualitative resemblance to the corresponding experimental data shown in Fig. 7.4(a). The spatial average $\bar{n}(E)$ indicated as the black line in Fig. 7.4(b) has a V shape expected of a uniform d -wave superconductor. However, the standard deviation $\Delta n(E)$ represented by the shaded region in the same figure grows with energy, and is large at energies larger than and comparable to $\Delta_0 = 0.055t$. Another way to appreciate the “low energy and high energy” dichotomy is to look at the spatial map of the normalized LDOS $n(\mathbf{x}, E)/\bar{n}(E)$ at different energies. There is a clear contrast between the relative homogeneity evident in the map at low energy shown in Fig. 7.5(c) ($E = 0$), and the inhomogeneity of the same map at a higher energy shown in Fig. 7.5(d) ($E = -0.2t \sim -4\Delta_0$). [Note that quantitative comparison between the experimental results in Fig. 7.4(a) and theory requires some care; for computational purposes (as discussed previously) we have taken a value of $\Delta_0 = 0.055t$ that is larger than the observed value in experiment.]

We now turn to the optical conductivity, whose temperature and frequency

dependences show trends that are shared across different material families of underdoped cuprates [see Figs. 7.6(a) and (b)]. Well above T_c , the real part of the complex conductivity $\sigma_1(\omega)$ is a monotonically decreasing function of ω , as expected of a metallic state. As the temperature is lowered, the response at ω below a certain frequency ω_{peak} is increasingly suppressed, and $\sigma_1(\omega)$ evolves into a superposition of a sharp peak at $\omega = 0$ and a broad peak at $\omega \sim \omega_{\text{peak}}$. Remarkably, the optical conductivity calculated within our model shows similar qualitative behavior. In the model, the persistence of an increasingly sharp peak at a non-zero energy is a consequence of pair formation. More importantly, the remaining sharp Drude-like peak with width that tends to zero as $T \rightarrow 0$ at small ω is a manifestation of the coherence of the near-nodal quasiparticles that are largely unscattered in the glassy nematic.

The role of the nematic cold-spot in the optical response can best be seen by comparing the case of the nematic glass in Fig. 7.6(c) with the case of point-like scattering in Fig. 7.6(d). When the nodal quasiparticles are scattered by the random potential, there remains a residual density of states at $\omega = 0$ even deep in the superconducting phase. As a result, a finite width Drude-like peak persists even as $T \rightarrow 0$.

The observed evolution of σ_1 from a “Drude-like” form at high temperatures to a superposition of a sharp peak at $\omega = 0$ and a broad peak at $\omega \sim \omega_{\text{peak}}$ is remarkably reproduced by the glassy nematic model. However, in the experiments, the crossover between the two forms onsets at the pseudogap temperature scale $\sim T^*$ well above superconducting T_c while the corresponding crossover onsets at the calculated (mean-field) superconducting T_c in our model. Notably, the experimental $\sigma_1(\omega)$ marches through T_c without much notice of it. It is as if d-wave gap

with nodes onsets at T^* , with nodal quasiparticles that are largely unscattered as they would be in the presence of glassy nematic order. We will further discuss constraints on models for $\sigma_1(\omega)$ at temperatures $T_c < T < T^*$ in the next section. The qualitative similarity between the measured spectra and those calculated from our glassy nematic model in the superconducting state at $T < T_c$ is not subject to this caveat; it is a robust result of the cold-spots, although the energy scale of the broader peak in experiment is larger than $2\Delta_0$.

7.5 Other forms of glassy order

We have carried out similar (although less extensive) calculations for various other forms of assumed glassy order. We comment here briefly on certain aspects of these results.

7.5.1 Superconducting d -form factor CDW glass

While the d -wave form factor in the case of a nematic glass is dictated by symmetry, for a CDW in which the ordering vector itself breaks the C_4 symmetry of the underlying crystal, the d -wave form factor is not symmetry dictated. Any CDW will thus necessarily have both s -wave and d -wave components; conversely, a dominantly d -wave form factor presumably reflects some feature of the microscopic physics (the “mechanism”) which produces the CDW. Not surprisingly, results obtained for a CDW glass with an assumed d -wave form factor share many qualitative features with those obtained for a nematic glass, as these arise from the assumed form factor directly. The major differences between the two situa-

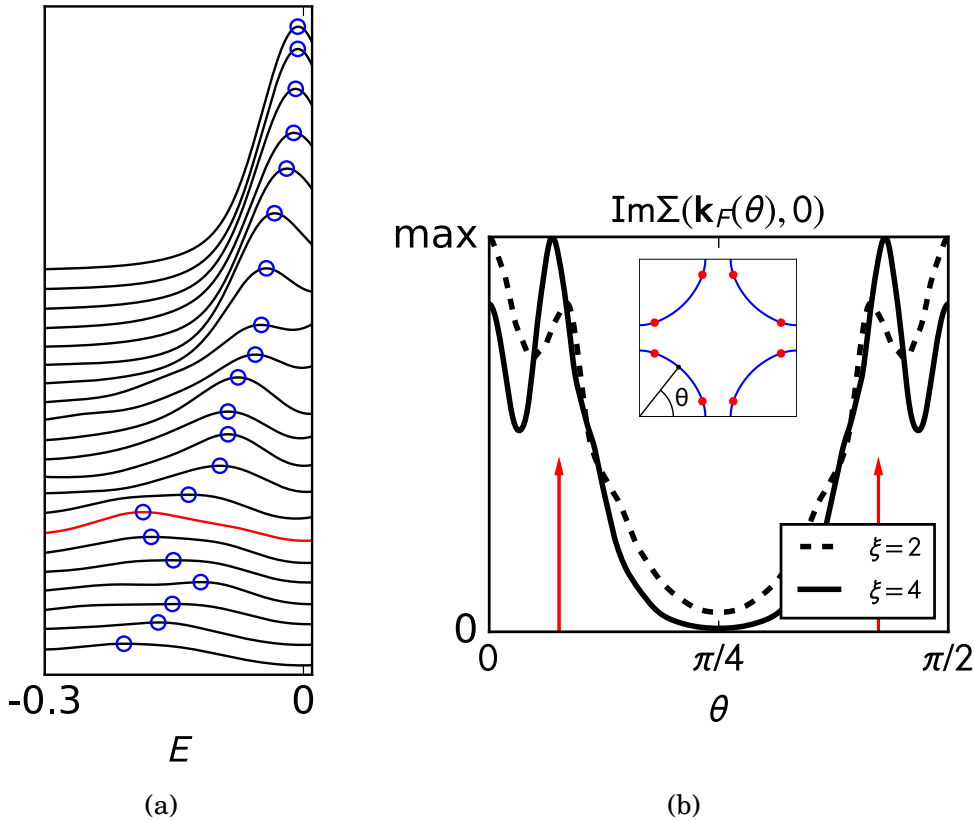


Figure 7.7: (a) EDCs along the Fermi surface [path 3 of Fig. 7.1(a)], calculated in the superconducting state in the presence of glassy charge-density-wave with a d -wave form factor and $\sqrt{\Gamma_{\text{cdw}}} = 0.2t$ and $\xi_{\text{cdw}} = 4a$, multiplied by Fermi function. The wavevector $\mathbf{Q} = (2\pi/a)(0.196, 0)$ is chosen to be a shortest vector connecting the intersection of Fermi surface and the magnetic Brillouin zone boundary, ($|k_x \pm k_y| = \pi$). Blue circles mark the maxima of each curve, and the red curve indicates the location of a hot-spot momentum. The angular dependence of the self-energy in the normal state with various values of ξ_{cdw} is shown in (b). The hot-spot momenta are indicated by red arrows (red dots in the inset).

tions concern the existence of “hot-spots” on the Fermi surface in the case of the d -form-factor CDW glass. Hot spots refer to the points on the pristine Fermi surface which are spanned by the CDW ordering vector – these are the points where, in a weak coupling analysis of CDW order, the effects of the CDW are expected to be most vivid.

The EDC of a d -form-factor CDW glass as a function of position along the Fermi surface is shown in Fig. 7.7(a) to be compared to Figs. 7.1(d) and 7.2(c). Although we have taken the CDW correlation length in our calculations to be quite short, $\xi_{\text{cdw}} = 4a$, (comparable to the CDW wavelength) the existence of a hot-spot is clearly seen in the non-monotonic evolution of the spectral function along the Fermi surface. This is in sharp contrast with the lack of any such feature in Fig. 7.1(d). The hot-spots are also visible in the electron self-energy of the normal state along the Fermi surface, as shown in Fig. 7.7(b); the hot-spot appears more sharply for longer ξ_{cdw} .

We have not explicitly explored the effects of glassy [26] “ d -density-wave (DDW) order” [54], because time-reversal-symmetry-breaking required for DDW brings with it additional issues of modeling. Nevertheless, since it also has a d -wave form factor, we expect that much of the nodal-antinodal dichotomy we have found would also apply to this form of ordering in the superconducting phase.

7.5.2 Optical conductivity for other models of antinodal gap

The fact that the “two-peak” structure (a sharp peak at $\omega = 0$ and a broad peak at $\omega = \omega_{\text{peak}}$) that is well-captured by our superconducting glassy nematic model below T_c persists above T_c in experiments is troublesome. Our result relies on two

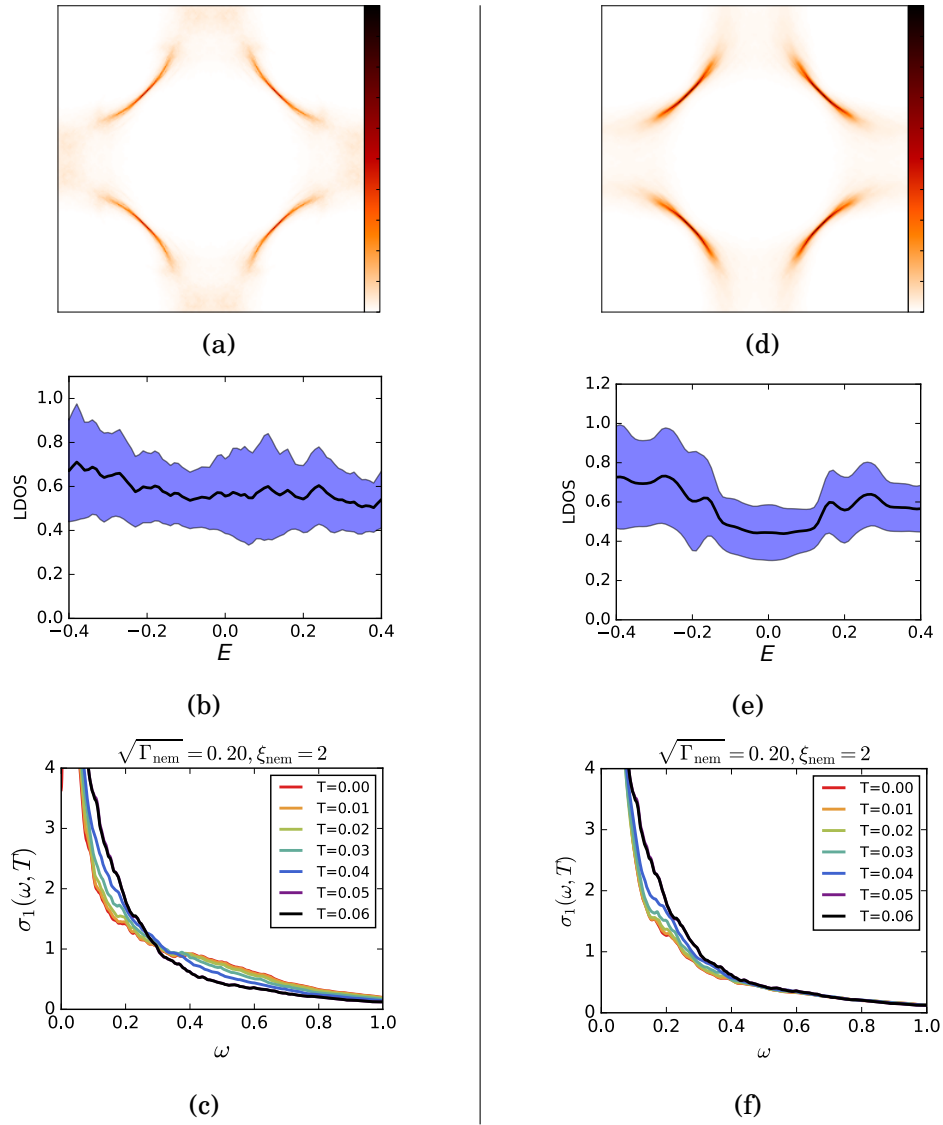


Figure 7.8: Various spectroscopic observables for a nematic glass with coexisting uniform d -density-wave order (DDW) (a-c) and with phase disordered (locally d -wave) superconductivity (PDdSC) (d-f). The DDW and PDdSC are set non-self-consistently by Eqs. (7.7) and (7.9), with no additional superconducting order. In the PDdSC, phase disordering of the superconducting state is represented by incorporating two pinned vortices and two anti-vortices. (a-c) Spectral function at the Fermi level, local density of states, and optical conductivity with DDW. (d-f) Spectral function at the Fermi level, local density of states, and optical conductivity with PDdSC.

essential ingredients of the model to obtain the “two-peak” structure: (1) a d-wave superconducting gap and (2) a d-wave form factor scattering. Given the apparent absurdity of assuming the persistence of a superconducting gap far above T_c , we consider two additional scenarios of a nematic glass with antinodal gaps to seek alternative explanations of the “two-peak” structure above T_c .

First we consider an ordered *d*-density-wave (DDW) [54–59] coexisting with glassy nematicity. We represent the DDW as a contribution to V with

$$\varphi(x, y) = i\Delta_{\text{ddw}}(-1)^{x+y} \quad (7.7)$$

with Eq. (7.4) extended to complex field:

$$V(\mathbf{x}, \mathbf{y}) = \frac{1}{2}f(\mathbf{x} - \mathbf{y})[\varphi(\mathbf{x}) + \varphi^*(\mathbf{y})] \quad (7.8)$$

where $f(\mathbf{r})$ is a *d*-wave form factor. Δ_{ddw} is chosen to be $\Delta_{\text{ddw}} = \Delta_{\text{ddw}}^0 \sqrt{1 - (T/T_c^0)^2}$ non-self-consistently. To compare with the superconducting state, we chose $T_c^0 = 0.05t$, and also $\Delta_{\text{ddw}}^0 = 0.05t$. This opens a gap at the antinodes, as the Fermi level spectral function in Fig. 7.8a shows. Nevertheless, the density of states remains finite [as indicated by the finite length of “arc” in Fig. 7.8(a), and also Fig. 7.8(b)], leading to the Drude-like peak at $T = 0$ in Fig. 7.8(c). Not surprisingly, DDW order alone is insufficient to account for the nature of the experimentally observed gapping below T_c ; even above T_c , it does not give as good an account of the structure of the optical conductivity as does the (apparently absurd) assumption of a persistent superconducting gap.

Another way to introduce an antinodal gap is in a model of a “phase-disordered” *d*-wave superconductor (PDdSC) with broken time-reversal symmetry. We introduce minimal phase disorder by incorporating vortices at positions $(0, 0)$ and $(L_x/2, L_y/2)$ and antivortices at positions $(L_x/2, 0)$ and $(0, L_y/2)$. We thus

non-self-consistently choose $\Delta_{\mathbf{xy}} = f(\mathbf{x} - \mathbf{y})\Delta(\frac{\mathbf{x} + \mathbf{y}}{2})$ to be a product of d -wave form factor $f(\mathbf{r}) = \delta_{\mathbf{r}, \pm \hat{x}} - \delta_{\mathbf{r}, \pm \hat{y}}$ and Jacobi theta functions:

$$\begin{aligned}\Delta(\mathbf{x}) &= \Delta_0 \sqrt{1 - \left(\frac{T}{T_c^0}\right)^2} \hat{\sigma}_W(z; 0) \hat{\sigma}_W\left(z; \frac{\pi}{2}(1+i)\right) \\ &\quad \times \hat{\sigma}_W^*\left(z; \frac{\pi}{2}\right) \hat{\sigma}_W^*\left(z; i\frac{\pi}{2}\right)\end{aligned}\quad (7.9)$$

where $z \equiv \frac{x}{L_x} + i\frac{y}{L_y}$, and $\hat{\sigma}_W$ is defined as

$$\hat{\sigma}_W(z; z_0) \equiv \sigma_W(z; z_0)/|\sigma_W(z; z_0)| \quad (7.10)$$

$$\sigma_W(z; z_0) \equiv e^{-\frac{\pi}{2}((z-z_0)^2 - 2z_0^*z)} \vartheta_3(z - z_0 | i). \quad (7.11)$$

Again we choose $T_c^0 = 0.05t$, and $\Delta_0 = 0.05t$. Figures 7.8(d)–7.8(f) show the resulting spectra. The spectral function shows that, while the antinodal excitations become gapped, a large portion of the Fermi surface still survives as noted by Berg and Altman [60]. This Fermi arc leads to a finite density of states in the limit $\omega \rightarrow 0$. In fact the density of states at low energies has a rather flat energy dependence with a suppressed but finite magnitude [Fig. 7.8(e)]. Correspondingly, we find that the optical conductivity does not show any suppression of the low energy spectral weight [Fig. 7.8(f)]. Again, this does not greatly resemble the experimental results for $T > T_c$. Instead, as with the DDW, the finite density of states at the Fermi level leads to a Drude-like peak at $\omega = 0$. Among the possibilities that we have considered, only the model with d -wave superconductivity on top of d -form-factor scattering with cold-spots qualitatively reproduce the experimentally measured $\sigma_1(\omega)$ for temperatures $T < T^*$.

7.6 Conclusion

In summary, we showed that the consonance between the cold-spots of a glassy nematic and the gap nodes of a d -wave superconductor can account for the most salient “anomalous” features of the spectroscopic measurements on the cuprates we have studied. It is natural in a glassy nematic superconductor that the nodal quasiparticles are long-lived, while away from the nodes, the quasiparticles are strongly perturbed by the local nematic order. This provides a simple explanation for the nodal-antinodal dichotomy observed by ARPES, and the strongly energy dependent heterogeneity observed by STM. Furthermore we found striking similarity between the temperature evolution and low temperature form of optical conductivities between our model and experiments. Nevertheless, the fact the “two-peak” structure of the optical response only occurs below T_c within our model, while it persists up to T^* in experiments, implies that fluctuational effects beyond those we have considered must be included in a complete theory of the pseudogap state.

Implicit in the above is the assumption that other sources of quasiparticle scattering – those associated with point-like (s form factor) disorder or with CDW ordering (either with s or d form factor) – are relatively weak. Specifically, as was pointed out previously [61], substantial scattering by point-like disorder can be ruled out directly from the experimentally observed sharp V-shape and relative homogeneity of the lowest energy portion of the LDOS. Above, we have further shown that significant scattering by a CDW with a substantial correlation length – even one with a d form factor – can be ruled out on the basis of the lack of any “hot-spot” in the observed ARPES spectrum. Since both point-like disorder potentials and short-range CDW order have been directly imaged in the same sort

of BSCCO samples we have used as the basis of these inferences, this raises the issue of why they are so weakly coupled to the low energy quasiparticles [29].

Our results point to interesting future directions. Firstly, a smoking-gun test of our conclusions would be to repeat the spectroscopic measurements on samples under uniaxial strain. We would predict the “anomalous features” to diminish as uniaxial strain detwines nematic domains. It is also plausible that the response of glassy nematicity to in-field magnetic field may introduce field-dependence of the anisotropic life-time.

BIBLIOGRAPHY

1. Tranquada, J. M., Sternlieb, B. J., Axe, J. D., Nakamura, Y. & Uchida, S. Evidence for stripe correlations of spins and holes in copper oxide superconductors. *Nature* **375**, 561 (1995).
2. v Zimmermann, M. *et al.* Hard X-ray diffraction study of charge stripe order in $\text{La}_{1.48}\text{Nd}_{0.4}\text{Sr}_{0.12}\text{CuO}_4$. *Europhys. Lett.* **41**, 629 (1998).
3. Abbamonte, P. *et al.* Spatially modulated 'Mottness' in $\text{La}_{2-x}\text{Ba}_x\text{CuO}_4$. *Nat. Phys.* **1**, 155 (2005).
4. Ghiringhelli, G. *et al.* Long-range incommensurate charge fluctuations in $(\text{Y}, \text{Nd})\text{Ba}_2\text{Cu}_3\text{O}_{6+x}$. *Science* **337**, 821 (2012).
5. Blackburn, E. *et al.* X-ray diffraction observations of a charge-density-wave order in superconducting ortho-II $\text{YBa}_2\text{Cu}_3\text{O}_{6.54}$ single crystals in zero magnetic field. *Phys. Rev. Lett.* **110**, 137004 (2013).
6. Comin, R. *et al.* Charge order driven by Fermi-arc instability in $\text{Bi}_2\text{Sr}_{2-x}\text{La}_x\text{CuO}_{6+\delta}$. *Science* **343**, 390 (2014).
7. Neto, E. H. d. S. *et al.* Ubiquitous interplay between charge ordering and high-temperature superconductivity in cuprates. *Science* **343**, 393 (2014).
8. Fujita, K. *et al.* Direct phase-sensitive identification of a d -form factor density wave in underdoped cuprates. *PNAS* **111**, E3026 (2014).
9. Chang, J. *et al.* Magnetic field controlled charge density wave coupling in underdoped $\text{YBa}_2\text{Cu}_3\text{O}_{6+x}$. *Nat. Commun.* **7**, 11494 (2016).
10. Gerber, S. *et al.* Three-dimensional charge density wave order in $\text{YBa}_2\text{Cu}_3\text{O}_{6.67}$ at high magnetic fields. *Science* **350**, 949 (2015).

11. Fradkin, E., Kivelson, S. A. & Tranquada, J. M. Colloquium: Theory of intertwined orders in high temperature superconductors. *Rev. Mod. Phys.* **87**, 457 (2015).
12. Howald, C., Eisaki, H., Kaneko, N., Greven, M. & Kapitulnik, A. Periodic density-of-states modulations in superconducting $\text{Bi}_2\text{Sr}_2\text{CaCu}_2\text{O}_{8+\delta}$. *Phys. Rev. B* **67**, 014533 (2003).
13. Lawler, M. J. *et al.* Intra-unit-cell electronic nematicity of the high- T_c copper-oxide pseudogap states. *Nature* **466**, 347 (2010).
14. Wu, T. *et al.* Incipient charge order observed by NMR in the normal state of $\text{YBa}_2\text{Cu}_3\text{O}_y$. *Nat. Commun.* **6**, 6438 (2015).
15. Hinkov, V. *et al.* Electronic liquid crystal state in the high-temperature superconductor $\text{YBa}_2\text{Cu}_3\text{O}_{6.45}$. *Science* **319**, 597 (2008).
16. Achkar, A. J. *et al.* Nematicity in stripe-ordered cuprates probed via resonant x-ray scattering. *Science* **351**, 576 (2016).
17. Ando, Y., Segawa, K., Komiya, S. & Lavrov, A. N. Electrical resistivity anisotropy from self-organized one dimensionality in high-temperature superconductors. *Phys. Rev. Lett.* **88**, 137005 (2002).
18. Daou, R. *et al.* Broken rotational symmetry in the pseudogap phase of a high- T_c superconductor. *Nature* **463**, 519 (2010).
19. Carlson, E. W., Dahmen, K. A., Fradkin, E. & Kivelson, S. A. Hysteresis and noise from electronic nematicity in high-temperature superconductors. *Phys. Rev. Lett.* **96**, 097003 (2006).
20. Robertson, J. A., Kivelson, S. A., Fradkin, E., Fang, A. C. & Kapitulnik, A. Distinguishing patterns of charge order: Stripes or checkerboards. *Phys. Rev. B* **74**, 134507 (2006).

21. Del Maestro, A., Rosenow, B. & Sachdev, S. From stripe to checkerboard ordering of charge-density waves on the square lattice in the presence of quenched disorder. *Phys. Rev. B* **74**, 024520 (2006).
22. Kim, E.-A. *et al.* Theory of the nodal nematic quantum phase transition in superconductors. *Phys. Rev. B* **77**, 184514 (2008).
23. Kaul, R. K., Melko, R. G., Metlitski, M. A. & Sachdev, S. Imaging bond order near nonmagnetic impurities in square-lattice antiferromagnets. *Phys. Rev. Lett.* **101**, 187206 (2008).
24. Phillabaum, B., Carlson, E. W. & Dahmen, K. A. Spatial complexity due to bulk electronic nematicity in a superconducting underdoped cuprate. *Nat. Commun.* **3**, 915 (2012).
25. Nie, L., Tarjus, G. & Kivelson, S. A. Quenched disorder and vestigial nematicity in the pseudogap regime of the cuprates. *PNAS* **111**, 7980 (2014).
26. Russo, A. & Chakravarty, S. Random field disorder and charge order driven quantum oscillations in cuprates. *Phys. Rev. B* **93**, 094504 (2016).
27. Trivedi, N., Scalettar, R. T. & Randeria, M. Superconductor-insulator transition in a disordered electronic system. *Phys. Rev. B* **54**, R3756 (1996).
28. Wang, Q.-H. & Lee, D.-H. Quasiparticle scattering interference in high-temperature superconductors. *Phys. Rev. B* **67**, 020511 (2003).
29. Garg, A., Randeria, M. & Trivedi, N. Strong correlations make high-temperature superconductors robust against disorder. *Nat. Phys.* **4**, 762 (2008).
30. Kim, E.-A. & Lawler, M. J. Interference of nematic quantum critical quasi-particles: A route to the octet model. *Phys. Rev. B* **81**, 132501 (2010).

31. Bouadim, K., Loh, Y. L., Randeria, M. & Trivedi, N. Single- and two-particle energy gaps across the disorder-driven superconductor-insulator transition. *Nat. Phys.* **7**, 884 (2011).
32. Balatsky, A. V., Vekhter, I. & Zhu, J.-X. Impurity-induced states in conventional and unconventional superconductors. *Rev. Mod. Phys.* **78**, 373 (2006).
33. Metzner, W., Rohe, D. & Andergassen, S. Soft Fermi surfaces and breakdown of Fermi-liquid behavior. *Phys. Rev. Lett.* **91**, 066402 (2003).
34. Yamase, H. & Metzner, W. Fermi-surface truncation from thermal nematic fluctuations. *Phys. Rev. Lett.* **108**, 186405 (2012).
35. Okamoto, S. & Furukawa, N. Spontaneous fourfold-symmetry breaking driven by electron-lattice coupling and strong correlations in high- T_c cuprates. *Phys. Rev. B* **86**, 094522 (2012).
36. Ioffe, L. B. & Millis, A. J. Zone-diagonal-dominated transport in high- T_c cuprates. *Phys. Rev. B* **58**, 11631 (1998).
37. Howald, C., Fournier, P. & Kapitulnik, A. Inherent inhomogeneities in tunneling spectra of $\text{Bi}_2\text{Sr}_2\text{CaCu}_2\text{O}_{8-x}$ crystals in the superconducting state. *Phys. Rev. B* **64**, 100504 (2001).
38. Pan, S. H. *et al.* Microscopic electronic inhomogeneity in the high- T_c superconductor $\text{Bi}_2\text{Sr}_2\text{CaCu}_2\text{O}_{8+x}$. *Nature* **413**, 282 (2001).
39. Pasupathy, A. N. *et al.* Electronic origin of the inhomogeneous pairing interaction in the high- T_c superconductor $\text{Bi}_2\text{Sr}_2\text{CaCu}_2\text{O}_{8+\delta}$. *Science* **320**, 196 (2008).
40. He, R.-H. *et al.* From a single-band metal to a high-temperature superconductor via two thermal phase transitions. *Science* **331**, 1579 (2011).

41. Hussey, N. E. *et al.* Angular dependence of the *c*-axis normal state magnetoresistance in single crystal $Tl_2Ba_2CuO_6$. *Phys. Rev. Lett.* **76**, 122 (1996).
42. Zheleznyak, A. T., Yakovenko, V. M., Drew, H. D. & Mazin, I. I. Phenomenological interpretations of the ac Hall effect in the normal state of $YBa_2Cu_3O_7$. *Phys. Rev. B* **57**, 3089 (1998).
43. Abdel-Jawad, M. *et al.* Anisotropic scattering and anomalous normal-state transport in a high-temperature superconductor. *Nat. Phys.* **2**, 821 (2006).
44. Abdel-Jawad, M. *et al.* Correlation between the superconducting transition temperature and anisotropic quasiparticle scattering in $Tl_2Ba_2CuO_{6+\delta}$. *Phys. Rev. Lett.* **99**, 107002 (2007).
45. Hussey, N. E. Phenomenology of the normal state in-plane transport properties of high- T_c cuprates. *J. Phys.: Condens. Matt.* **20**, 123201 (2008).
46. French, M. M. J., Analytis, J. G., Carrington, A., Balicas, L. & Hussey, N. E. Tracking anisotropic scattering in overdoped $Tl_2Ba_2CuO_{6+\delta}$ above 100 K. *New J. Phys.* **11**, 055057 (2009).
47. Kaminski, A. *et al.* Momentum anisotropy of the scattering rate in cuprate superconductors. *Phys. Rev. B* **71**, 014517 (2005).
48. Dell'Anna, L. & Metzner, W. Electrical resistivity near Pomeranchuk instability in two dimensions. *Phys. Rev. Lett.* **98**, 136402 (2007).
49. Schattner, Y., Lederer, S., Kivelson, S. A. & Berg, E. Ising nematic quantum critical point in a metal: a Monte Carlo study. arXiv: 1511.03282.
50. Lederer, S., Shattner, Y., Berg, E. & Kivelson, S. A. unpublished. *unpublished*.

51. McElroy, K. *et al.* Coincidence of checkerboard charge order and antinodal state decoherence in strongly underdoped superconducting $\text{Bi}_2\text{Sr}_2\text{CaCu}_2\text{O}_{8+\delta}$. *Phys. Rev. Lett.* **94**, 197005 (2005).
52. Romero, D. B. *et al.* Quasiparticle damping in $\text{Bi}_2\text{Sr}_2\text{CaCu}_2\text{O}_8$ and $\text{Bi}_2\text{Sr}_2\text{CuO}_6$. *Phys. Rev. Lett.* **68**, 1590 (1992).
53. Mirzaei, S. I. *et al.* Spectroscopic evidence for Fermi liquid-like energy and temperature dependence of the relaxation rate in the pseudogap phase of the cuprates. *PNAS* **110**, 5774 (2013).
54. Chakravarty, S., Laughlin, R. B., Morr, D. K. & Nayak, C. Hidden order in the cuprates. *Phys. Rev. B* **63**, 094503 (2001).
55. Schulz, H. J. Fermi-surface instabilities of a generalized two-dimensional Hubbard model. *Phys. Rev. B* **39**, 2940 (1989).
56. Affleck, I. & Marston, J. B. Large- n limit of the Heisenberg-Hubbard model: Implications for high- T_c superconductors. *Phys. Rev. B* **37**, 3774 (1988).
57. Kotliar, G. Resonating valence bonds and d -wave superconductivity. *Phys. Rev. B* **37**, 3664 (1988).
58. Ivanov, D. A., Lee, P. A. & Wen, X.-G. Staggered-vorticity correlation in a lightly doped t - J model: A variational approach. *Phys. Rev. Lett.* **84**, 3958 (2000).
59. Nayak, C. Density-wave states of nonzero angular momentum. *Phys. Rev. B* **62**, 4880 (2000).
60. Berg, E. & Altman, E. Evolution of the Fermi surface of d -Wave superconductors in the presence of thermal phase fluctuations. *Phys. Rev. Lett.* **99**, 247001 (2007).

61. Jamei, R. *et al.* Inferring effective interactions from the local density of states: Application to STM data from $\text{Bi}_2\text{Sr}_2\text{CaCu}_2\text{O}_{8+\delta}$. *Phys. Rev. B* **74**, 174521 (2006).

CHAPTER 8

SUPERCONDUCTOR UNDER MAGNETIC FIELD

In addition to zero electrical resistivity, response to external magnetic field is also a defining property of a superconductor. First discovered by Meissner and Ochsenfeld in 1933 [1], superconductors exhibit perfect diamagnetism, i.e., the magnetic field is completely excluded from the bulk of superconductor. In 1935, a new phase of superconductivity is discovered between Meissner phase and normal phase [2]. In this phase, known as Shubnikov phase or vortex phase, magnetic field penetrates the bulk of superconductor by creating vortices. Superconductors with a direct transition between Meissner phase and normal phase are called type-I superconductors (Fig. 8.1a), while superconductors which exhibit Shubnikov phase are called type-II superconductors (Fig. 8.1b).

In this chapter, we discuss how to include magnetic field in the BdG Hamiltonian, and how vortices are introduced.

8.1 Magnetic Translation Operator

Under magnetic field, ordinary translation operator no longer commutes with the Hamiltonian: The full (lattice) translation group is replaced by a *magnetic translation group*. In this section we will derive magnetic translation operators under constant magnetic field, and discuss how they can be used to simplify the Hamiltonian.

Ordinary translation operator in the absence of magnetic field which is defined

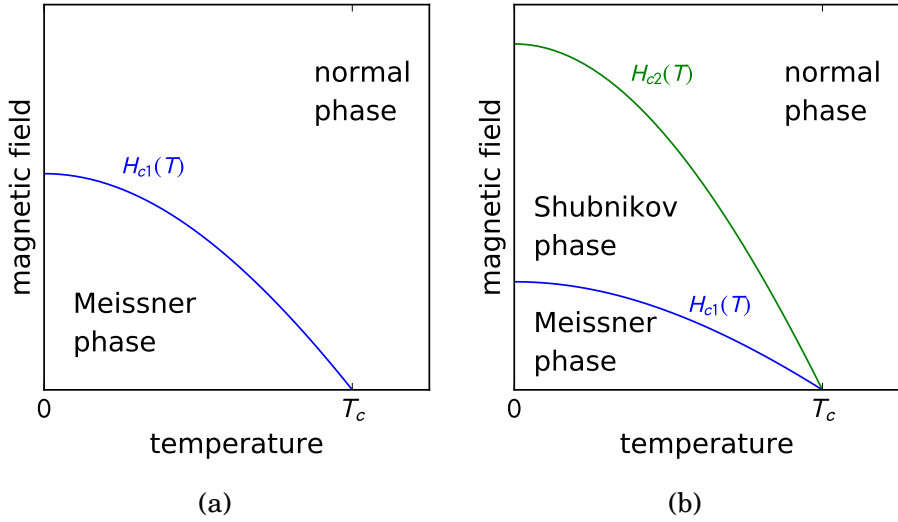


Figure 8.1: (a) Phase diagram of type-I superconductor. (b) Phase diagram of type-II superconductor.

for a single particle state by $T_{\mathbf{a}}|\mathbf{x}\rangle = |\mathbf{x} + \mathbf{a}\rangle$, i.e.,

$$\langle \mathbf{x}|T_{\mathbf{a}}|\psi\rangle = \int d^d y (T_{\mathbf{a}}^\dagger|\mathbf{x}\rangle)^\dagger \psi(\mathbf{y})|\mathbf{y}\rangle = \int d^d y \langle \mathbf{x} - \mathbf{a}|\psi(\mathbf{y})|\mathbf{y}\rangle = \psi(\mathbf{x} - \mathbf{a}), \quad (8.1)$$

can be written as

$$T_{\mathbf{a}} = e^{-i\mathbf{a}\cdot\mathbf{p}}. \quad (8.2)$$

It is easily shown how $T_{\mathbf{a}}$ affects the position operator \mathbf{x} : Using the commutation relation $[x_\mu, p_\nu] = i\delta_{\mu\nu}$ and Hadamard lemma, we get

$$T_{\mathbf{a}}x_\mu T_{\mathbf{a}}^{-1} = e^{-i\mathbf{a}\cdot\mathbf{p}}x_\mu = x_\mu + [-i\mathbf{a}\cdot\mathbf{p}, x_\mu] + \dots = x_\mu - a_\mu \quad (8.3)$$

Under magnetic field $\mathbf{B} = \nabla \times \mathbf{A}$, the kinetic energy of a particle with charge q is

$$\mathcal{K} = \mathcal{K}(\mathbf{p}) \rightarrow \mathcal{K}(\mathbf{p} - q\mathbf{A}). \quad (8.4)$$

Choosing $\tilde{\mathbf{A}}(\mathbf{x})$ which satisfies following commutation

$$[p_\mu - qA_\mu(x), p_\nu - q\tilde{A}_\nu] = 0 \quad (8.5)$$

which implies

$$\partial_\mu A_\nu(\mathbf{x}) = \partial_\nu \tilde{A}_\mu(\mathbf{x}), \quad (8.6)$$

we can define the following *magnetic translation operator*

$$\tilde{T}_{\mathbf{X}} \equiv e^{-i\mathbf{X}\cdot(\mathbf{p}-q\tilde{\mathbf{A}})} \quad (8.7)$$

which commutes with the kinetic energy. Under constant magnetic field (and thus $\mathbf{A}(\mathbf{x})$ linear in \mathbf{x}), $\tilde{T}_{\mathbf{X}}$ can be shown to be identical to the following operator up to a constant phase using Baker-Campbell-Hausdorff formula¹:

$$\hat{T}_{\mathbf{X}} \equiv e^{iq\mathbf{X}\cdot\tilde{\mathbf{A}}} e^{-i\mathbf{X}\cdot\mathbf{p}} = (\text{const.}) \tilde{T}_{\mathbf{X}} \quad (8.8)$$

Thus, from here on, we refer to \hat{T}_X as magnetic translation operator. For example,

$$\hat{T}_{\mathbf{X}} |\mathbf{x}\rangle = e^{iq\mathbf{X}\cdot\tilde{\mathbf{A}}(\mathbf{x}+\mathbf{X})} |\mathbf{x}+\mathbf{X}\rangle, \quad (8.9)$$

or, in second quantized notation,

$$\hat{T}_{\mathbf{X}} c^*(\mathbf{x}) \hat{T}_{\mathbf{X}}^\dagger = c^*(\mathbf{x}+\mathbf{X}) e^{iq\mathbf{X}\cdot\tilde{\mathbf{A}}(\mathbf{x}+\mathbf{X})}, \quad \hat{T}_{\mathbf{X}} c(\mathbf{x}) \hat{T}_{\mathbf{X}}^\dagger = c(\mathbf{x}+\mathbf{X}) e^{-iq\mathbf{X}\cdot\tilde{\mathbf{A}}(\mathbf{x}+\mathbf{X})}. \quad (8.10)$$

By construction, $[\hat{T}_{\mathbf{X}}, \mathcal{K}(\mathbf{p}-q\mathbf{A})] = 0$. There is, however, one caveat: the magnetic translation operators do not commute with each other in general:

$$[\hat{T}_{\mathbf{X}_1}, \hat{T}_{\mathbf{X}_2}] = e^{iq(\mathbf{X}_1+\mathbf{X}_2)\cdot\tilde{\mathbf{A}}(\mathbf{x})} \left(e^{iq\mathbf{X}_2\cdot\tilde{\mathbf{A}}(\mathbf{X}_1)} - e^{iq\mathbf{X}_1\cdot\tilde{\mathbf{A}}(\mathbf{X}_2)} \right) T_{\mathbf{X}_1} T_{\mathbf{X}_2} \quad (8.11)$$

It is nevertheless possible to find a set of mutually commuting $\hat{T}_{\mathbf{X}}$, by requiring

$$q\mathbf{X}_2 \cdot \tilde{\mathbf{A}}(\mathbf{X}_1) - q\mathbf{X}_1 \cdot \tilde{\mathbf{A}}(\mathbf{X}_2) = 2\pi n, \quad n \in \mathbb{Z}. \quad (8.12)$$

Therefore, choosing $\{\mathbf{X}_i\}$ to be on a lattice whose unit cell contains integer number of flux quanta,² we get a set of commuting operators

$$[\hat{T}_{\mathbf{X}_1}, \hat{T}_{\mathbf{X}_2}] = 0 \quad (8.13)$$

which all commute with kinetic energy.

¹ $e^{X+Y} = e^X e^Y e^{-\frac{1}{2}[X,Y]} e^{\frac{1}{6}(2[Y,[X,Y]]+[X,[X,Y]])} \dots$

² Here we use the term *magnetic flux quantum* to refer to $2\pi/e$. Historically, however, magnetic flux quantization has been observed first in a superconductor [3], and the term flux quantum has been used to mean π/e .

8.2 Two-dimensional Lattice System

Now let us apply the above construction to a two-dimensional lattice system. For simplicity, take a 2D square lattice system with size $(L_x, L_y) = (M_x N_x, M_y N_y)$ with constant perpendicular field $B \mathbf{e}_z = \frac{\Phi_0}{N_x N_y} \mathbf{e}_z$, where $\Phi_0 = 2\pi/q$. Magnetic unit cell can be chosen to have size (N_x, N_y) . From here on, we use the following notation:

$$\begin{aligned}\mathbf{r} &= (x, y) & \text{for } x = 0, \dots, L_x - 1, & \quad y = 0, \dots, L_y - 1 \\ \mathbf{R} &= (X, Y) = (m_x N_x, m_y N_y) & \text{for } m_x = 0, \dots, M_x - 1, & \quad m_y = 0, \dots, M_y - 1\end{aligned}\quad (8.14)$$

Naively, with $\mathbf{A}(\mathbf{x})$ linear to \mathbf{x} , “periodic boundary condition” requires

$$\hat{T}(L_x, 0) = \hat{T}(0, L_y) = 1. \quad (8.15)$$

In terms of L and $\tilde{\mathbf{A}}$, this implies that for any $\mathbf{r} \in \{0, \dots, N_x - 1\} \times \{0, \dots, N_y - 1\}$,

$$q L_x \tilde{A}_x(\mathbf{r}) = q L_y \tilde{A}_y(\mathbf{r}) = 2\pi n, \quad n \in \mathbb{Z} \quad (8.16)$$

Depending on the gauge choice, this leads to different requirements on M and N . For example, in the naive “Landau gauge” with $\mathbf{A}(\mathbf{r}) = -By\hat{\mathbf{e}}_x$ and thus $\tilde{\mathbf{A}}(\mathbf{r}) = -Bx\hat{\mathbf{e}}_y$, the magnetic translation operator writes

$$\hat{T}_{\mathbf{R}} = e^{iq\mathbf{R} \cdot \tilde{\mathbf{A}}(\mathbf{r})} T_{\mathbf{R}} = e^{-iqBYx} T_{\mathbf{R}} = e^{-i2\pi m_y x / N_x} T_{\mathbf{R}}. \quad (8.17)$$

Periodic boundary condition requires

$$\frac{2\pi}{\Phi_0} M_y N_y \frac{\Phi_0}{N_x N_y} x = 2\pi \frac{M_y}{N_x} x = 2\pi n \quad (8.18)$$

and thus M_y should be a multiple of N_x . As will be shown later in Section 8.5, such requirements on the system size can be relaxed by threading a Dirac string through the system.

8.3 Kinetic Energy in Magnetic Field

Kinetic energy of a charged particle minimally coupled to constant magnetic field can be simplified using magnetic translation operator. Consider the following Hamiltonian on a lattice

$$\mathcal{H} = \sum_{\mathbf{r}_1 \mathbf{r}_2} c^\dagger(\mathbf{r}_1) K(\mathbf{r}_1 \mathbf{r}_2) c(\mathbf{r}_2), \quad (8.19)$$

where

$$K(\mathbf{r}_1, \mathbf{r}_2) = t(\mathbf{r}_1, \mathbf{r}_2) e^{-i\varphi(\mathbf{r}_1, \mathbf{r}_2)}, \quad \text{with } \varphi(\mathbf{r}_1, \mathbf{r}_2) \equiv q \int_{\mathbf{r}_2}^{\mathbf{r}_1} \mathbf{A}(\mathbf{r}) \cdot d\mathbf{r}. \quad (8.20)$$

In this chapter, we use $c_\alpha(\mathbf{x})$ to represent an annihilation operator at site \mathbf{x} . Translation of the kinetic energy by \mathbf{R} gives

$$K(\mathbf{r}_1 + \mathbf{R}, \mathbf{r}_2 + \mathbf{R}) = K(\mathbf{r}_1, \mathbf{r}_2) e^{-iq(\tilde{\mathbf{A}}_1 - \tilde{\mathbf{A}}_2) \cdot \mathbf{R}} \quad (8.21)$$

It is easy to show that $[\mathcal{H}, \hat{T}_{\mathbf{R}}] = 0$ when \mathbf{R} is a magnetic lattice vector. It is, therefore, possible to block-diagonalize \mathcal{H} by decomposing it into eigenstates of $\hat{T}_{\mathbf{R}}$. Remember that the convention for momentum basis when $\mathbf{B} = 0$ is

$$\begin{aligned} c_{\mathbf{k}}^\dagger &= \frac{1}{\sqrt{N}} \sum_{\mathbf{r}} c^\dagger(\mathbf{r}) e^{i\mathbf{k} \cdot \mathbf{r}} = \frac{1}{\sqrt{N}} \sum_{\mathbf{r}} T_{\mathbf{r}} c^\dagger(\mathbf{0}) T_{\mathbf{r}}^{-1} e^{i\mathbf{k} \cdot \mathbf{r}} \\ c_{\mathbf{k}} &= \frac{1}{\sqrt{N}} \sum_{\mathbf{r}} e^{-i\mathbf{k} \cdot \mathbf{r}} c(\mathbf{r}) = \frac{1}{\sqrt{N}} \sum_{\mathbf{r}} e^{-i\mathbf{k} \cdot \mathbf{r}} T_{\mathbf{r}} c(\mathbf{0}) T_{\mathbf{r}}^{-1} \end{aligned} \quad (8.22)$$

Similarly, for $\mathbf{B} = B \hat{\mathbf{e}}_z$, we can define crystal momentum basis using magnetic translation operator:

$$c_{\mathbf{k}}^\dagger(\tilde{\mathbf{r}}) \equiv \frac{1}{\sqrt{M}} \sum_{\mathbf{R}} \hat{T}_{\mathbf{R}} c^\dagger(\tilde{\mathbf{r}}) \hat{T}_{\mathbf{R}}^{-1} e^{i\mathbf{k} \cdot \mathbf{R}} = \frac{1}{\sqrt{M}} \sum_{\mathbf{R}} c^\dagger(\tilde{\mathbf{r}} + \mathbf{R}) e^{-iq\mathbf{A}(\tilde{\mathbf{r}}) \cdot \mathbf{R}} e^{i\mathbf{k} \cdot \mathbf{R}} \quad (8.23)$$

where $\tilde{\mathbf{r}}$ is a lattice vector *within a magnetic unit cell*, \mathbf{R} a *magnetic* lattice vector, \mathbf{k} a *magnetic* crystal momentum, and $M = M_x M_y$. The inverse transform is

$$c^\dagger(\tilde{\mathbf{r}} + \mathbf{R}) = \frac{1}{\sqrt{M}} \sum_{\mathbf{k} \in \text{MUC}} e^{iq\mathbf{A}(\tilde{\mathbf{r}}) \cdot \mathbf{R}} e^{-i\mathbf{k} \cdot \mathbf{R}} c_{\mathbf{k}}^\dagger(\tilde{\mathbf{r}}) \quad (8.24)$$

The kinetic energy can then be written as

$$\mathcal{K} = \sum_{\{\tilde{\mathbf{r}}_i\}, \mathbf{k}} c_{\mathbf{k}}^\dagger(\tilde{\mathbf{r}}_1) K_{\mathbf{k}}(\tilde{\mathbf{r}}_1, \tilde{\mathbf{r}}_2) c_{\mathbf{k}}(\tilde{\mathbf{r}}_2), \quad (8.25)$$

where

$$K_{\mathbf{k}}(\tilde{\mathbf{r}}_1, \tilde{\mathbf{r}}_2) = \sum_{\mathbf{R}} e^{-i(\mathbf{k}-q\tilde{\mathbf{A}}(\tilde{\mathbf{r}}_1)\cdot\mathbf{R})} K(\tilde{\mathbf{r}}_1 + \mathbf{R}, \tilde{\mathbf{r}}_2) \quad (8.26)$$

8.4 Bogoliubov Quasiparticles in Magnetic Field

Let us now bring superconductivity into the discussion. Consider the following BdG Hamiltonian

$$\mathcal{H} = \frac{1}{2} \sum_{\mathbf{r}_1 \mathbf{r}_2} \begin{pmatrix} c^\dagger(\mathbf{r}_1) & c^T(\mathbf{r}_1) \end{pmatrix} \begin{pmatrix} K(\mathbf{r}_1, \mathbf{r}_2) & \Delta(\mathbf{r}_1, \mathbf{r}_2) \\ -\Delta^*(\mathbf{r}_1, \mathbf{r}_2) & -K^*(\mathbf{r}_1, \mathbf{r}_2) \end{pmatrix} \begin{pmatrix} c(\mathbf{r}_2) \\ c^*(\mathbf{r}_2) \end{pmatrix} \quad (8.27)$$

In the previous section, we have shown that the kinetic energy \mathcal{K} can be block diagonalized in crystal momentum basis. Here we discuss whether the same applies to the pairing term Δ . Using magnetic translation operators, the Fourier transform of the creation/annihilation operator can be written in terms of the Nambu spinor as follows:

$$\psi^\dagger(\tilde{\mathbf{r}} + \mathbf{R}) = \frac{1}{\sqrt{M}} \sum_{\mathbf{k}} \psi_{\mathbf{k}}^\dagger(\tilde{\mathbf{r}}) e^{-i\mathbf{k}\cdot\mathbf{R} + iq\tilde{\mathbf{A}}\cdot\mathbf{R}\tau_3}. \quad (8.28)$$

The Hamiltonian can then be written as

$$\begin{aligned} \mathcal{H} &= \sum_{\mathbf{R}_1 \mathbf{R}_2} \sum_{\tilde{\mathbf{r}}_1 \tilde{\mathbf{r}}_2} \psi^\dagger(\tilde{\mathbf{r}}_1 + \mathbf{R}_1) H(\tilde{\mathbf{r}}_1 + \mathbf{R}_1, \tilde{\mathbf{r}}_2 + \mathbf{R}_2) \psi(\tilde{\mathbf{r}}_2 + \mathbf{R}_2) \\ &= \sum_{\{\tilde{\mathbf{r}}_i, \mathbf{k}_i\}} \psi_{\mathbf{k}_1}^\dagger(\tilde{\mathbf{r}}_1) H_{\mathbf{k}_1 \mathbf{k}_2}(\tilde{\mathbf{r}}_1, \tilde{\mathbf{r}}_2) \psi_{\mathbf{k}_2}(\tilde{\mathbf{r}}_2), \end{aligned} \quad (8.29)$$

where

$$H_{\mathbf{k}_1 \mathbf{k}_2}(\tilde{\mathbf{r}}_1, \tilde{\mathbf{r}}_2) \equiv \frac{1}{M} \sum_{\{\mathbf{R}_i\}} e^{-i\mathbf{k}_1 \cdot \mathbf{R}_1 + iq\tilde{\mathbf{A}}_1 \cdot \mathbf{R}_1 \tau_3} H(\tilde{\mathbf{r}}_1 + \mathbf{R}_1, \tilde{\mathbf{r}}_2 + \mathbf{R}_2) e^{i\mathbf{k}_2 \cdot \mathbf{R}_2 - iq\tilde{\mathbf{A}}_2 \cdot \mathbf{R}_2 \tau_3}. \quad (8.30)$$

In order for the Hamiltonian to be written in block-diagonal form in terms of $\psi_{\mathbf{k}}(\tilde{\mathbf{r}})$, we need

$$H_{\mathbf{k}_1 \mathbf{k}_2}(\tilde{\mathbf{r}}_1, \tilde{\mathbf{r}}_2) = H_{\mathbf{k}_1}(\tilde{\mathbf{r}}_1, \tilde{\mathbf{r}}_2) \delta_{\mathbf{k}_1 \mathbf{k}_2}. \quad (8.31)$$

When $H \propto \tau_0, \tau_3$, (i.e. the normal components) the condition needed to satisfy Eq. (8.31) is

$$H(\mathbf{r}_1 + \mathbf{R}, \mathbf{r}_2 + \mathbf{R}) = e^{-i\tau_3 q[\tilde{\mathbf{A}}(\mathbf{r}_1) - \tilde{\mathbf{A}}(\mathbf{r}_2)] \cdot \mathbf{R}} H(\mathbf{r}_1, \mathbf{r}_2) \quad (8.32)$$

which is already satisfied by the kinetic term in the diagonal block, as we have shown in the previous section. When $H \propto \tau_1, \tau_2$ (i.e. the pairing components), on the other hand, translational invariance requires that

$$H(\mathbf{r}_1 + \mathbf{R}, \mathbf{r}_2 + \mathbf{R}) = e^{-i\tau_3 q[\tilde{\mathbf{A}}(\mathbf{r}_1) + \tilde{\mathbf{A}}(\mathbf{r}_2)] \cdot \mathbf{R}} H(\mathbf{r}_1, \mathbf{r}_2) \quad (8.33)$$

In general, there is no guarantee that the pairing term can be block diagonalized in the magnetic crystal momentum basis. However, when the vortices form a lattice, which is often the case in order to minimize the free energy, with two vortices within a single magnetic unit cell [4], the pairing term indeed commutes with the magnetic translation operator, and can be written in block diagonal form. Let us confirm here that when the eigenstates of the Hamiltonian are also eigenstates of the magnetic translation operator, the self-consistency does not destroy the magnetic translational symmetry. In the full self-consistency loop, Δ is determined by the following self-consistency equation

$$\Delta_{\alpha\beta}(\mathbf{r}_1, \mathbf{r}_2) = \frac{1}{2} \sum_{\mathbf{r}_3 \mathbf{r}_4 \mu\nu} V_{\alpha\beta,\mu\nu}(\mathbf{r}_1, \mathbf{r}_2; \mathbf{r}_3, \mathbf{r}_4) \langle c_\nu(\mathbf{r}_4) c_\mu(\mathbf{r}_3) \rangle \quad (8.34)$$

In terms of $c_{\mathbf{k}}^\dagger(\tilde{\mathbf{r}})$ and $c_{\mathbf{k}}(\tilde{\mathbf{r}})$,

$$\langle c_\nu(\tilde{\mathbf{r}}_4 + \mathbf{R}_4) c_\mu(\tilde{\mathbf{r}}_3 + \mathbf{R}_3) \rangle = \frac{1}{M} \sum_{\mathbf{k}} \langle c_{-\mathbf{k}\nu}(\tilde{\mathbf{r}}_4) c_{\mathbf{k}\mu}(\tilde{\mathbf{r}}_3) \rangle e^{i\mathbf{k}(-\mathbf{R}_3 + \mathbf{R}_4) + iq(\tilde{\mathbf{A}}_3 \cdot \mathbf{R}_3 + \tilde{\mathbf{A}}_4 \cdot \mathbf{R}_4)}. \quad (8.35)$$

The pairing term can be written as

$$\begin{aligned}\Delta_{\alpha\beta}(\mathbf{r}_1, \mathbf{r}_2) &= \frac{1}{2} \sum_{\mathbf{R}_3 \mathbf{R}_4 \tilde{\mathbf{r}}_3 \tilde{\mathbf{r}}_4} V_{\alpha\beta;\mu\nu}(\mathbf{r}_1 - \tilde{\mathbf{r}}_4 - \mathbf{R}_4, \mathbf{r}_2 - \tilde{\mathbf{r}}_4 - \mathbf{R}_4; \tilde{\mathbf{r}}_3 - \tilde{\mathbf{r}}_4 + \mathbf{R}_3 - \mathbf{R}_4, \mathbf{0}) \\ &\quad \times \frac{1}{M} \sum_{\mathbf{k}} \left\langle c_{-\mathbf{k}\nu}(\tilde{\mathbf{r}}_4) c_{\mathbf{k}\mu}(\tilde{\mathbf{r}}_3) \right\rangle e^{i\mathbf{k} \cdot (\mathbf{R}_3 - \mathbf{R}_4) + iq(\tilde{\mathbf{A}}_3 \cdot \mathbf{R}_3 + \tilde{\mathbf{A}}_4 \cdot \mathbf{R}_4)},\end{aligned}\quad (8.36)$$

where $\tilde{\mathbf{A}}_i$ is a shorthand for $\tilde{\mathbf{A}}(\tilde{\mathbf{r}}_i)$. Under translation by a magnetic lattice vector \mathbf{R} ,

$$\begin{aligned}\Delta_{\alpha\beta}(\mathbf{r}_1 + \mathbf{R}, \mathbf{r}_2 + \mathbf{R}) &= \frac{1}{2} \sum_{\mathbf{R}_3 \mathbf{R}_4 \tilde{\mathbf{r}}_3 \tilde{\mathbf{r}}_4} V_{\alpha\beta;\mu\nu}(\mathbf{r}_1 - \tilde{\mathbf{r}}_4 - \mathbf{R}_4, \mathbf{r}_2 - \tilde{\mathbf{r}}_4 - \mathbf{R}_4; \tilde{\mathbf{r}}_3 - \tilde{\mathbf{r}}_4 + \mathbf{R}_3 - \mathbf{R}_4, \mathbf{0}) \\ &\quad \times \frac{1}{M} \sum_{\mathbf{k}} \left\langle c_{-\mathbf{k}\nu}(\tilde{\mathbf{r}}_4) c_{\mathbf{k}\mu}(\tilde{\mathbf{r}}_3) \right\rangle e^{i\mathbf{k} \cdot (\mathbf{R}_3 - \mathbf{R}_4) + iq(\tilde{\mathbf{A}}_3 \cdot \mathbf{R}_3 + \tilde{\mathbf{A}}_4 \cdot \mathbf{R}_4)} e^{iq(\tilde{\mathbf{A}}_3 + \tilde{\mathbf{A}}_4) \cdot \mathbf{R}}.\end{aligned}\quad (8.37)$$

The structure of the interaction term \mathcal{V} ensures that $(\tilde{\mathbf{A}}_3 + \tilde{\mathbf{A}}_4) \cdot \mathbf{R} = (\tilde{\mathbf{A}}_1 + \tilde{\mathbf{A}}_2) \cdot \mathbf{R}$. Therefore, the self-consistency equation preserves the magnetic translational symmetry of the pairing term:

$$\Delta_{\alpha\beta}(\mathbf{r}_1 + \mathbf{R}, \mathbf{r}_2 + \mathbf{R}) = \Delta_{\alpha\beta}(\mathbf{r}_1, \mathbf{r}_2) e^{-iq(\tilde{\mathbf{A}}_1 + \tilde{\mathbf{A}}_2) \cdot \mathbf{R}}\quad (8.38)$$

To sum, the Hamiltonian can be block diagonalized as

$$H_{\mathbf{k}}(\tilde{\mathbf{r}}_1, \tilde{\mathbf{r}}_2) \equiv \sum_{\mathbf{R}} e^{-i(\mathbf{k}_1 - q\tau_3 \tilde{\mathbf{A}}_1) \cdot \mathbf{R}} H(\tilde{\mathbf{r}}_1 + \mathbf{R}, \tilde{\mathbf{r}}_2).\quad (8.39)$$

As we will see in Chapter 9, self-consistent solution of Eq. (8.35) with the Hamiltonian Eq. (8.27) automatically introduces two vortices per magnetic unit cell.

8.5 Franz-Tešanović Gauge

In previous sections, we have shown that, as a result of out-of-plane magnetic field, the system loses ordinary translation symmetry, but is replaced by a magnetic

translation symmetry. Because of non-zero magnetic flux through each magnetic unit cell, however, the magnetic translation operator differs from the ordinary translation operator, and this leads to small difficulties, one example being the matching of the periodic boundary condition mentioned at the end of Section 8.2.

To resolve this issue, Franz and Tešanović [5] have presented a singular gauge transformation which makes magnetic translation equivalent to ordinary translation. Their starting point is the observation that each superconducting vortex entraps one-half magnetic flux quantum, and that a single magnetic unit cell contains two superconducting vortices. Since a string of infinitesimal radius containing an integer multiple of magnetic flux quantum (a Dirac string) through the system is physically not observable, one can thread those strings through the system so as to cancel out the total flux from the physical magnetic field. As the simplest approach, one might try putting half flux quantum for each vortex. This, however, leads to a multivaluedness of the wave function around the vortex [6, 7]. Franz and Tešanović solved this issue in the following way: Since there are two vortices in each MUC, and there are two species of fermionic excitations (spin up and down), you can insert an integer flux string through one of the vortex, which only the spin up electrons can experience, and another string through the other vortex, which only spin down electrons can experience. By doing this, one can get avoid multivaluedness, and also make magnetic translation operator same as ordinary translation operators.

Working with a lattice model, however, circumvents the singularity problem: As long as the Dirac string stays away from sites and bonds, no singularity enters the Hamiltonian. Therefore, it is possible to place the string anywhere in the system, without any assumptions on the location of the vortices, as in Ref. [5].

For concreteness, let us consider a 2D square lattice of size $N_x \times N_y$, with constant out-of-plane magnetic field $\Phi_0/(N_x N_y)$ through the system. Assume periodic boundary condition, and that the hoppings are only between the nearest neighbors. For every plaquette, the phase winding around it (i.e. Wilson loop variable) should equal $2\pi/(N_x N_y)$ modulo 2π . Defining

$$\begin{aligned} a_{x,y} &\equiv (N_x N_y / 2\pi) \times (\text{Peierls phase from site } (x, y) \text{ to site } (x+1, y)), \\ b_{x,y} &\equiv (N_x N_y / 2\pi) \times (\text{Peierls phase from site } (x, y) \text{ to site } (x, y+1)), \end{aligned} \quad (8.40)$$

the condition for the magnetic flux can be written as

$$f_{x,y} \equiv a_{x,y} + b_{x+1,y} - a_{x,y+1} - b_{x,y} = 1 \pmod{N_x N_y}. \quad (8.41)$$

We then make the total magnetic flux through the whole system zero, by inserting a flux quantum at $(N_x - \epsilon_1, N_y - \epsilon_2)$, where $\epsilon_i \rightarrow 0^+$. The ratio between ϵ_1 and ϵ_2 does not matter when we only have nearest neighbor hoppings. If, however, there are second and third neighbor (and higher) hoppings, we need to make sure that the flux quantum stays out of the ways of these hopping bonds, and therefore $\epsilon_1/\epsilon_2 = 1, 1/2, 2, \dots$ should be avoided. Then Eq. (8.41) writes

$$f_{x,y} = a_{x,y} + b_{x+1,y} - a_{x,y+1} - b_{x,y} = \begin{cases} 1 - N_x N_y, & \text{for } x = N_x - 1, y = N_y - 1 \\ 1 & \text{otherwise.} \end{cases} \quad (8.41')$$

Any set of $\{a_{x,y}, b_{x,y}\}$ which satisfies the above equation is a valid gauge configuration.

A simple example configuration which satisfies Eq. (8.41) can be constructed through following steps. First, set $a_{x,y}$ and $b_{x,y}$ following the Landau gauge $\mathbf{A} = -By\hat{\mathbf{e}}_x$ for most part of the system:

$$a_{x,y} = -y \quad \text{for } x = 0, \dots, N_x - 1 \text{ and } y = 0, \dots, N_y - 1 \quad (8.42)$$

$$b_{x,y} = 0 \quad \text{for } x = 0, \dots, N_x - 1 \text{ and } y = 0, \dots, N_y - 2. \quad (8.43)$$

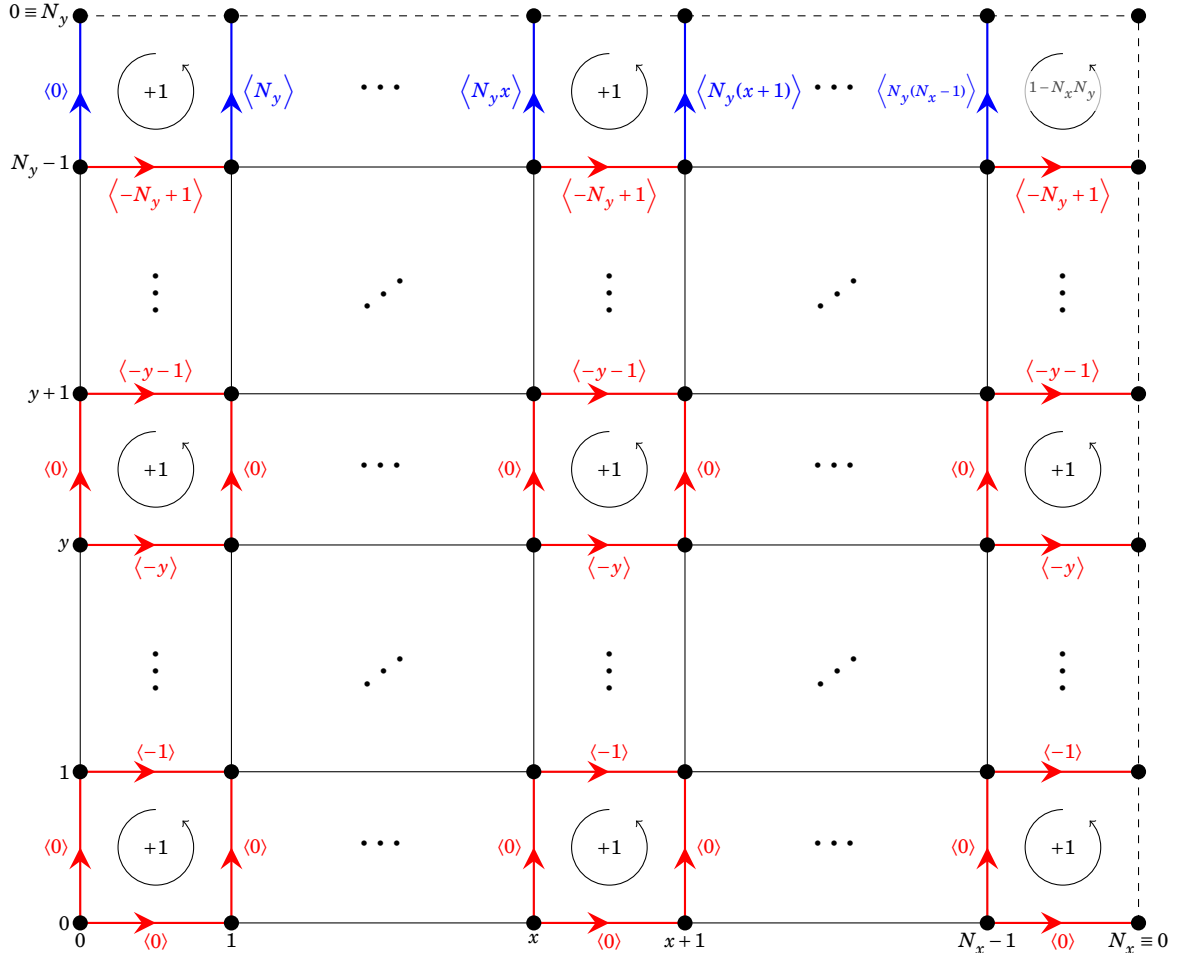


Figure 8.2: An example configuration of “Landau-Franz-Tešanović” gauge on a 2D system with unit magnetic flux quantum through the system. Periodic boundary condition is imposed. The black dots represent sites, and arrows hoppings. The numbers in angled bracket are the a 's and b 's of the hopping, defined as in the text. (They represent phase of the hopping along the direction of the arrow, divided by $2\pi/N_x N_y$.) The loop inside the placket indicates the sum of a and b in that direction.

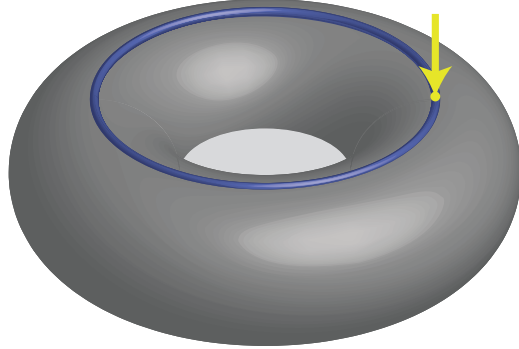


Figure 8.3: The continuum analogue of gauge configuration of Fig. 8.2. The yellow arrow and the blue line marks the Dirac string entering the torus and the branch cut.

(This is marked by red arrows in Fig. 8.2.) This step assigns $2\pi/N_x N_y$ flux through every plaquette except the top row. Now requiring that the plaquettes at the top row also contain $2\pi/N_x N_y$ flux each, we can set

$$b_{x,N_y-1} = N_y x \quad \text{for } x = 0, \dots, N_y - 1 \quad (8.44)$$

(This is marked by blue arrows in Fig. 8.2.) The plaquette at the top right corner then automatically satisfies

$$f_{N_x-1,N_y-1} = 1 - N_x N_y, \quad (8.45)$$

which is exactly what we need.

Note that this is analogous to the continuum gauge configuration with singularity at the the corner of a magnetic unit cell, with branch cuts horizontally connecting the two adjacent singularities.

BIBLIOGRAPHY

1. Meissner, W. & Ochsenfeld, R. Ein neuer Effekt bei Eintritt der Supraleitfähigkeit. *Naturwissenschaften* **21**, 787 (1933).
2. Rjabinin, J. N. & Shubnikow, L. W. Magnetic properties and critical currents of supra-conducting alloys. *Nature* (1935).
3. Deaver, B. S. & Fairbank, W. M. Experimental evidence for quantized flux in superconducting cylinders. *Phys. Rev. Lett.* **7**, 43 (1961).
4. Abrikosov, A. On the magnetic properties of superconductors of the second group. *Sov. Phys. JETP* **5**, 1174 (1957).
5. Franz, M. & Tešanović, Z. Quasiparticles in the vortex lattice of unconventional superconductors: Bloch waves or Landau levels? *Phys. Rev. Lett.* **84**, 554 (2000).
6. Anderson, P. W. Anomalous magnetothermal resistance of high- T_c superconductors: Anomalous cyclotron orbits at a Dirac point. arXiv: cond-mat/9812063.
7. Balents, L., Fisher, M. P. A. & Nayak, C. Dual order parameter for the nodal liquid. *Phys. Rev. B* **60**, 1654 (1999).

CHAPTER 9

RESEARCH PAPER:

SIGNATURES OF UNCONVENTIONAL PAIRING IN NEAR-VORTEX

ELECTRONIC STRUCTURE OF LiFeAs

Kyungmin Lee, Mark H. Fischer, and Eun-Ah Kim

Department of Physics, Cornell University, Ithaca, New York 14853, USA.

Published on New Journal of Physics **15**, 053048 (2013).

Abstract

A major question in Fe-based superconductors remains the structure of the pairing, in particular whether it is of unconventional nature. The electronic structure near a vortex can serve as a platform for phase-sensitive measurements to answer this question. By solving the Bogoliubov-de Gennes equations for LiFeAs, we calculate the energy-dependent local electronic structure near a vortex for different nodeless gap-structure possibilities. At low energies, the local density of states (LDOS) around a vortex is determined by the normal-state electronic structure. At energies closer to the gap value, however, the LDOS can distinguish an anisotropic *s*-wave gap from a conventional isotropic *s*-wave gap. We show within our self-consistent calculation that in addition, the local gap profile differs between a conventional and an unconventional pairing. We explain this through admixing of a secondary order parameter within Ginzburg-Landau theory. In-field scanning tunneling spectroscopy near a vortex can therefore be used as a real-space probe of the gap structure.

9.1 Introduction

The gap structure in the Fe-based superconductors and its possible unconventional nature is still a key issue in the field four years after their discovery. In most compounds, the pairing is believed to be of the so-called s^\pm type, for which the order parameter changes sign between the electron-like and the hole-like Fermi surfaces [1, 2]. Some experimental results are consistent with this prediction [3–7]. However, a major difficulty in distinguishing such an unconventional pairing state from a trivial s -wave gap is that both states are nodeless and transform trivially under all the symmetry operations of the material’s point group. As the experimental probes that are usually used to distinguish various gap structures, such as phase-sensitive probes, are not Fermi pocket specific, an unambiguous evidence of the unconventional s^\pm pairing remains evasive.

One route to accessing phase information using a phase-insensitive probe would be through vortex bound states, as a vortex introduces a spatial texture to the superconducting order parameter. Advancements in in-field scanning tunneling spectroscopy (STS) have enabled the study of vortex bound states. Indeed, a recent STS experiment on LiFeAs under a magnetic field has shown an intriguing energy dependence in the spatial distribution of the local density of states (LDOS) near a vortex [8]. The remaining question is whether the observed LDOS distribution near vortex can be instrumental in selecting one of the proposed gap structures: s^\pm -wave [1], s^{++} -wave [9, 10], and (spin-triplet) p -wave [11, 12]. At zero bias, the LDOS shows a four-fold star shape with high-intensity ‘rays’ along the Fe-As direction. Similar features in NbSe_2 [13] were interpreted as a sign of gap minima along this direction. However, a quasi-classical analysis by Wang *et al.* [14] pointed out that the normal-state band structure of LiFeAs – namely a

highly anisotropic hole pocket around the Γ point – could be producing these rays irrespective of gap structure. By contrast, little attention has been given to the high energy LDOS distribution observed in Ref. [8]: hot spots appearing at the intersection of split rays.

Motivated by these observations, we present a study of the near-vortex electronic structure and signatures of unconventional pairing therein within the Bogoliubov-de Gennes (BdG) framework. By (non-self-consistently) imposing a gap structure and solving the BdG Hamiltonian, we first show that the isotropic s -wave and s^\pm -wave pairing result in different spatial distributions of the LDOS at energies approaching the gap value. In particular, we find s^\pm -wave pairing to yield the observed hot spots. Then we solve the BdG equations self-consistently, and based on our results propose detecting the spatial distribution of the gap around a vortex for a more direct evidence of unconventional s^\pm -wave pairing. A vortex not only suppresses the order-parameter amplitude at its core and introduces a singular point in space around which the phase of the order parameter winds, but it also induces a secondary order parameter in its vicinity [15–19]. Due to the induced secondary order parameter near the vortex, the gap recovery should show a strong angular dependence. Detection of such anisotropy will be an unambiguous evidence of unconventional pairing.

The remainder of this paper is organized as follows: In sections 2 and 3, we introduce the microscopic model and describe the Bogoliubov-de Gennes calculations, respectively. In section 4, we present the results of the BdG calculations and discuss them within Ginzburg-Landau theory. In section 5, we summarize our findings and remark on future directions. Throughout the paper we focus on the large hole pocket and study the single band problem. However, we also

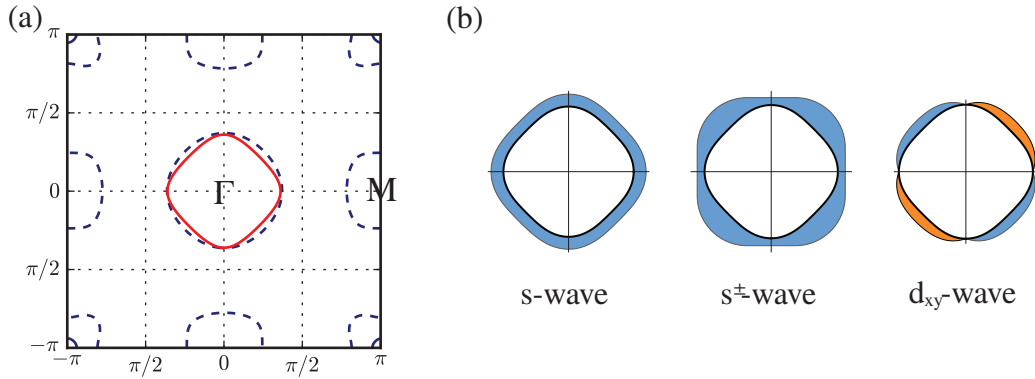


Figure 9.1: (a) Comparison of two tight-binding models for LiFeAs used in this paper in the 1-Fe Brillouin zone. The dashed lines indicate the Fermi surfaces of the five-band model from Ref. [20]. For the most part of this work, we focus on the γ band that is around the Γ point, whose Fermi surface is shown as a solid line. (b) Sketch of the three gap functions with s -, s^\pm -, and d_{xy} -wave momentum structure around the γ -band Fermi surface.

present results from non-self-consistent BdG calculations on a five-band model in section 4, which show good agreement with observations from single-band model calculations in the energy range of our interest.

9.2 Model

We describe LiFeAs in the superconducting state with the (mean-field) BdG Hamiltonian

$$\mathcal{H}^{\text{BdG}} = \sum_{ij} \Psi_i^\dagger \begin{pmatrix} -t_{ij} & \Delta_{ij} \\ \Delta_{ij}^* & t_{ij}^* \end{pmatrix} \Psi_j. \quad (9.1)$$

Here, $\Psi_i \equiv (c_{i\uparrow}, c_{i\downarrow}^\dagger)^T$ is a Nambu spinor, and c_{is} (c_{is}^\dagger) annihilates (creates) an electron at lattice site i with spin s within a single-band model for the large hole pocket around the Γ point: the so-called γ band. However, Eq. (9.1) can easily be

generalized for a multi-band model. In this paper, we focus on the single-band model for the most part since the superconducting gap is the smallest on the γ band [21, 22] and hence we expect low energy physics to be dominated by this band. Moreover, this band mainly stems from the (in-plane) d_{xy} orbitals, and thus shows little k_z dependence [23]. It is therefore a natural choice for LiFeAs. Note that previous BdG calculations on different Fe-pnictides focused on two-band models for the d_{xz} / d_{yz} orbitals [24–29]. Our choice of the hopping matrix t_{ij} is guided by the experimental observations on the γ pocket [21, 22, 30] to be $t = -0.25\text{eV}$ for nearest-neighbor hopping, $t' = 0.082\text{eV}$ for next-nearest-neighbor hopping, and $t_{ii} = \mu = 0.57\text{eV}$ for the chemical potential. Figure 9.1a shows the resulting Fermi surface in solid red line. Though we stay within this single-band model for the self-consistent BdG studies, we have also used a five-band model for the non-self-consistent calculation with tight-binding parameters from Ref. [20] to test the validity of focussing on the γ band for the energy range of our interest (see section 4.2). Figure 9.1a shows the Fermi surface of the five-band model in dashed lines.

The Δ_{ij} are the (bond) gap functions. For a self-consistent solution of \mathcal{H}^{BdG} , we require the gap functions to satisfy

$$\Delta_{ij} = \frac{1}{2} V_{ij} \langle c_{i\downarrow} c_{j\uparrow} + c_{j\downarrow} c_{i\uparrow} \rangle, \quad (9.2)$$

where $V_{ij} < 0$ is the attractive interaction between sites i and j in the singlet channel, and $\langle \cdot \rangle$ denotes the thermal expectation value. Restricting the interaction V_{ij} to a specific form constrains the momentum structure of the gap function, since $\Delta_{ij} \neq 0$ only if $V_{ij} \neq 0$. In the uniform case, an on-site attraction $V_{ij} = U\delta_{ij}$ leads to a spin-singlet s -wave gap $\Delta(\mathbf{k}) = \Delta_s^0$, while a next-nearest-neighbor (NNN) attraction $V_{ij} = V'\delta_{\langle\langle i,j \rangle\rangle}$ allows for the singlet gap functions of s^\pm form, $\Delta(\mathbf{k}) = 4\Delta_{s^\pm}^0 \cos k_x \cos k_y$, and d_{xy} form, $\Delta(\mathbf{k}) = 4\Delta_{d_{xy}}^0 \sin k_x \sin k_y$. Figure 9.1b shows sketches of these gap functions. We restrict our calculations in the following

to these ‘pure’ gap structures. Even though the true gap function is a (symmetry-allowed) mixture of such gap functions, the dominant channel (on-site or NNN interactions) will determine whether an s^\pm - or an s^{++} -wave gap is realized in the presence of the electron pockets.

For the non-self-consistent BdG study, the vortex will be imposed through the gap-function configuration of

$$\Delta_{ij} = \Delta^0 \tanh(|\mathbf{r}_{ij}|/\xi) e^{i\theta_{ij}}, \quad (9.3)$$

where the vector \mathbf{r}_{ij} points to the midpoint of sites i and j , and θ_{ij} is its azimuthal angle measured from the Fe-Fe direction. This corresponds to a single vortex located at the origin suppressing locally the order-parameter amplitude. In addition, the order-parameter phase winds around the vortex core.

For the self-consistent BdG study, we induce the vortices by applying a magnetic field $H\hat{z}$. Assuming minimal coupling between an electron and the field, the hopping between sites i and j acquires a Peierls phase

$$t_{ij} \longrightarrow t_{ij} e^{i\varphi(\mathbf{r}_i, \mathbf{r}_j)}, \quad \varphi(\mathbf{r}_i, \mathbf{r}_j) \equiv -\frac{\pi}{\Phi_0} \int_{\mathbf{r}_j}^{\mathbf{r}_i} \mathbf{A}(\mathbf{r}) \cdot d\mathbf{r}, \quad (9.4)$$

where $\Phi_0 = h/2e$ is the magnetic fluxoid and \mathbf{r}_i is the vector pointing to the site i . We assume a uniform magnetic field H and write the vector potential in the Landau gauge $\mathbf{A}(\mathbf{r}) = -Hy\hat{x}$. From the self-consistent solution Δ_{ij} , we can define local gap order parameters of different symmetries. For an on-site interaction, the local s -wave order parameter is defined as $\Delta_s(\mathbf{r}) = \Delta_{\mathbf{r}, \mathbf{r}}$. Note that from here on, we use \mathbf{r} without any site index to denote both a lattice site and the vector pointing to it in units of the lattice constant a_0 . With NNN interaction, we define local order parameters of s^\pm form

$$\Delta_{s^\pm}(\mathbf{r}) = \frac{1}{4} [\tilde{\Delta}_{\mathbf{r}+(1,1), \mathbf{r}} + \tilde{\Delta}_{\mathbf{r}+(1,-1), \mathbf{r}} + \tilde{\Delta}_{\mathbf{r}+(-1,-1), \mathbf{r}} + \tilde{\Delta}_{\mathbf{r}+(-1,1), \mathbf{r}}] \quad (9.5)$$

and d_{xy} form

$$\Delta_{d_{xy}}(\mathbf{r}) = \frac{1}{4}[\tilde{\Delta}_{\mathbf{r}+(1,1),\mathbf{r}} - \tilde{\Delta}_{\mathbf{r}+(1,-1),\mathbf{r}} + \tilde{\Delta}_{\mathbf{r}+(-1,-1),\mathbf{r}} - \tilde{\Delta}_{\mathbf{r}+(-1,1),\mathbf{r}}], \quad (9.6)$$

where $\tilde{\Delta}_{\mathbf{rr}'} \equiv \Delta_{\mathbf{rr}'} \exp[-i\varphi(\mathbf{r}, \mathbf{r}')]$ ensures that order parameters of different symmetries do not mix under magnetic translations. Note that for the uniform case, $\Delta_s(\mathbf{r}) = \Delta_s^0$, $\Delta_{s^\pm}(\mathbf{r}) = \Delta_{s^\pm}^0$, and $\Delta_{d_{xy}}(\mathbf{r}) = \Delta_{d_{xy}}^0$ as defined above.

9.3 Method

In this section, we elaborate on our two approaches to solve the BdG equations and obtain the LDOS near a vortex. For both, diagonalizing the Hamiltonian \mathcal{H}^{BdG} in Eq. (9.1) for a system of size (N_x, N_y) is computationally the most expensive part.

9.3.1 Non-Self-Consistent Approach

For the non-self-consistent calculation, we impose a gap function in the form given by Eq. (9.3) and find the low lying eigenvalues and eigenstates of \mathcal{H}^{BdG} using the Lanczos algorithm¹. The LDOS can be calculated from the eigenenergies E^n and eigenstates $[u^n(\mathbf{r}), v^n(\mathbf{r})]$ as

$$N(\mathbf{r}, E) = \sum_n |u^n(\mathbf{r})|^2 \delta(E - E^n) + |v^n(\mathbf{r})|^2 \delta(E + E^n). \quad (9.7)$$

Since we are not interested in the absolute value of the LDOS but rather in the spatial profile at a given energy, we normalize the LDOS such that for a given energy E , the maximum value of $N(\mathbf{r}, E)$ is unity.

¹We suppress low energy states from forming at the boundary by imposing an on-site potential of 10 eV to the sites at the boundary.

9.3.2 Self-Consistent Approach

For the self-consistent calculation, we assume initial gap functions and use the eigenvalues and eigenvectors of Eq. (9.1) to calculate the gap functions given by Eq. (9.2). We proceed iteratively until self-consistency is achieved. In diagonalizing $\hat{\mathcal{H}}^{\text{BdG}}$, we can no longer make use of the crystal momentum basis to simplify the problem since the Peierls phase factor prevents the kinetic part of the Hamiltonian from commuting with the ordinary lattice translation operator $T_{\mathbf{R}}$. However, the kinetic part commutes with the magnetic translation operator

$$\hat{T}_{\mathbf{R}} \equiv e^{-i \frac{\pi}{\Phi_0} \mathbf{A}(\mathbf{R}) \cdot \mathbf{r}} T_{\mathbf{R}} \quad (9.8)$$

for a magnetic lattice vector \mathbf{R} whose unit cell contains two magnetic fluxoids.

The pairing term in general does not commute with $\hat{T}_{\mathbf{R}}$. Nevertheless, when vortices form a lattice, $\hat{T}_{\mathbf{R}}$ commutes with the pairing term when \mathbf{R} is a vector of a vortex sublattice containing every other vortex. Since we focus on the electronic structure near a single vortex, we expect the shape of the vortex lattice to have little influence on our results. Therefore, we make an arbitrary choice for its primitive vectors to be $L_x \hat{x}$ and $L_y \hat{y}$, such that \mathbf{R} forms a rectangular lattice $\mathbf{R} = (m_x L_x, m_y L_y)$, where $m_\alpha = 0 \cdots M_\alpha - 1$ and $M_\alpha \equiv N_\alpha / L_\alpha$ ². Note that periodic boundary conditions in the Landau gauge $\mathbf{A}(\mathbf{r}) = -Hy\hat{x}$ require the total magnetic flux through the system to be an integer multiple of $2\Phi_0 N_x$. In addition, one magnetic unit cell contains a magnetic flux of $2\Phi_0$, i.e. $H = 2\Phi_0 / L_x L_y$. We satisfy these two requirements by choosing $M_x = L_y, M_y = L_x$.

²This choice yields an oblique vortex lattice, since there are two vortices in each (rectangular) magnetic unit cell, trying to form a triangular vortex lattice as a self-consistent solution.

Working with the magnetic Bloch states

$$\Psi_{\mathbf{k}}(\mathbf{r}) = \sum_{\mathbf{R}} e^{-i\mathbf{k}\cdot\mathbf{R}} \hat{T}_{\mathbf{R}} \Psi(\mathbf{r}) \hat{T}_{\mathbf{R}}^{-1} \quad (9.9)$$

allows us to block diagonalize the Hamiltonian

$$\mathcal{H}^{BdG} = \frac{1}{M_x M_y} \sum_{\mathbf{k}} \sum_{\mathbf{r}, \mathbf{r}'} \Psi_{\mathbf{k}}^{\dagger}(\mathbf{r}) H_{\mathbf{k}}(\mathbf{r}, \mathbf{r}') \Psi_{\mathbf{k}}(\mathbf{r}'). \quad (9.10)$$

The indices \mathbf{k} and \mathbf{r} from here on are defined in the magnetic Brillouin zone and magnetic unit cell, respectively, that is

$$\mathbf{k} = \left(2\pi \frac{m_x}{L_x M_x}, 2\pi \frac{m_y}{L_y M_y} \right), \quad m_\alpha = 0 \cdots M_\alpha - 1, \quad (9.11a)$$

$$\mathbf{r} = (\ell_x, \ell_y), \quad \ell_\alpha = 0 \cdots L_\alpha - 1. \quad (9.11b)$$

By diagonalizing the matrices $H_{\mathbf{k}}$ of dimension $2L_x L_y \times 2L_x L_y$ in Eq. (9.10), we can compute the eigenstates and eigenenergies of \mathcal{H}^{BdG} . These are then used to calculate Δ_{ij} with Eq. (9.2) closing the self-consistency cycle. Finally, we use the self-consistent solution Δ_{ij} to calculate the local order parameters of s -, s^\pm - and d_{xy} -wave symmetry and also the LDOS of the electronic degrees of freedom, as defined in Eq. (9.7).

9.4 Results

9.4.1 Non-Self-Consistent Approach on Single Band Model

Figure 9.2 shows the near-vortex LDOS calculated by diagonalizing \mathcal{H}^{BdG} of Eq. (9.1) with fixed gap functions as given by Eq. (9.3) on a system of dimension $(N_x, N_y) = (301, 301)$. We choose realistic values of the parameters for the coherence length $\xi = 16.4a_0$ [31, 32], as well as gap values $\Delta_s^0 = 3\text{meV}$ for on-site pairing and $\Delta_{s^\pm}^0 = 1.5\text{meV}$ for NNN pairing [21, 22, 30].

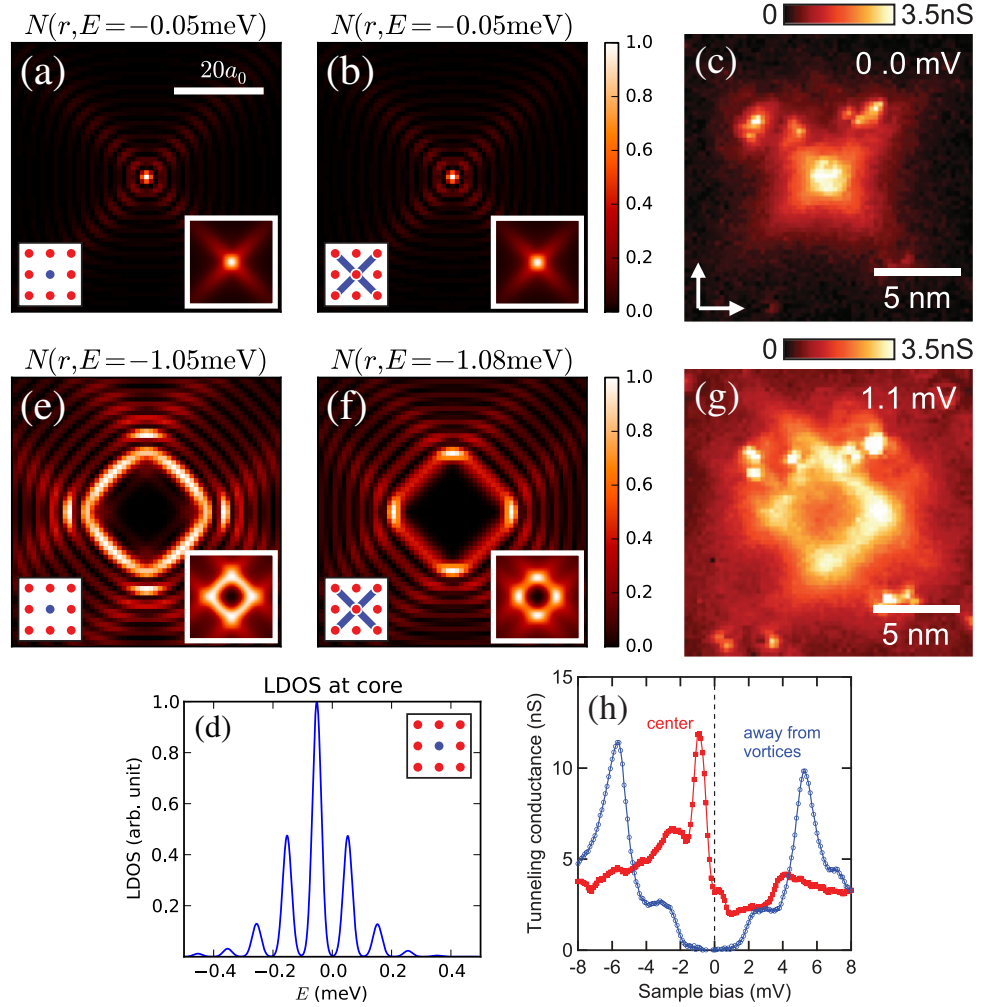


Figure 9.2: Local density of states near a vortex for the non-self-consistent calculation with the gap function given by Eq. (9.3). The value $N(\mathbf{r}, E)$ has been normalized such that the maximum value in each map is unity. (a) shows the LDOS at the lowest bound state energy with on-site pairing with $\Delta^0 = 3 \text{ meV}$, and (e) is at higher energy. (b) and (f) are with NNN pairing with $\Delta^0 = 1.5 \text{ meV}$. The left insets in (a),(b),(e) and (f) indicate the local structure of the pairing, and the right insets are LDOS after gaussian filtering ($\sigma = 3a_0$) reducing spatial resolution for better comparison with experiment [8]. (c) and (g) are the near-vortex LDOS maps observed in Ref. [8]. (d) is the LDOS as a function of energy at the vortex core for the on-site pairing, Gaussian-filtered in both energy ($\sigma = 0.15 \text{ meV}$) and position ($\sigma = a_0$). (h) shows the experimental tunneling spectra from Ref. [8] for comparison.

We can interpret the vortex bound states in this non-self-consistent BdG calculation as bound states in a potential well given by Eq. (9.3), where only states around the normal-state Fermi surface constitute the bound states. There are then two sources of anisotropy: anisotropic, quasi-one-dimensional low-energy properties of the normal state, and an anisotropic gap, both defined in the momentum space. The geometric distribution of LDOS will be dominated by one or the other source of anisotropy at different energies.

At low energies, the normal state properties dominate the distribution of LDOS (Fig. 9.2a and b). Hence irrespective of pairing structure, the bound state is located at the center of the potential well. Since the Bloch states making up this bound state have two main velocities due to the quasi-one-dimensional parts of the Fermi surface, the bound state mainly extends in these two directions out of the well, resulting in the rays in Fig. 9.2a and b. The gap is suppressed near the vortex center, and its anisotropy is of little importance. Hence the flat (quasi-one-dimensional) parts of the electronic structure in Fig. 9.1a (solid line) dominate over the small anisotropy of the s^\pm gap (see Fig. 9.1b). For a better comparison with experiment, we present results of reduced spatial resolution by gaussian filtering ($\sigma = 3a_0$) in the insets. The low resolution result is consistent with results of the quasi-classical analysis by Wang *et al.* [14] and in good agreement with experiment shown in Fig. 9.2c.

At higher energies on the other hand, the bound state is located away from the vortex core. The quasi-one-dimensionality of the Fermi surface allows for localization in one direction and extension in the other. This leads to a square-like inner ring in the LDOS for both pairings (Fig. 9.2e and f). The difference, however, results from the anisotropy of the gap function. While the isotropic s -wave

gap is analogous to a potential that is independent of momentum, the anisotropic gap is one for which different states around the Fermi surface experience different potentials depending on their momenta. With the gap function of s^\pm form, the quasi-one-dimensional portion of the Fermi surface experiences a stronger trap potential, leading to a suppression of its contribution to the bound-state wave function. As a result, the bound state exhibits pronounced isolated segments, ‘hot spots,’ within the inner ring that point in the Fe-Fe direction, as shown in Fig. 9.2f. We again gaussian filter the images and show them in the insets. Note the ‘hot spot’ are robust and even more pronounced in the low resolution insets in Fig. 9.2f in good agreement with the experimental data Fig. 9.2g.

We now turn to the LDOS at the core of the vortex and its particle-hole asymmetry. This turns out to be largely insensitive to anisotropy of pairing. The LDOS at the core of the vortex for the on-site pairing shown in Fig 9.2d exhibits particle-hole asymmetry with the highest peak at negative energy. Such asymmetry appears in the so-called ‘quantum-limit’ vortex bound state [33], whose highest LDOS peak is at energy $\Delta^2/2E_F$ above(below) the Fermi energy for an electron(hole)-like band, where E_F is the energy difference between the Fermi energy and the bottom(top) of the band. The energy of the LDOS peak being 0.05meV below the Fermi energy is expected given $E_F = 98\text{meV}$ and $\Delta = 3\text{meV}$ within our input bandstructure. Though similar particle-hole asymmetry has been observed in Ref. [8] (see Fig. 9.2h) the energy at which the peak was observed suggests that other hole pockets with larger gap values may be responsible.

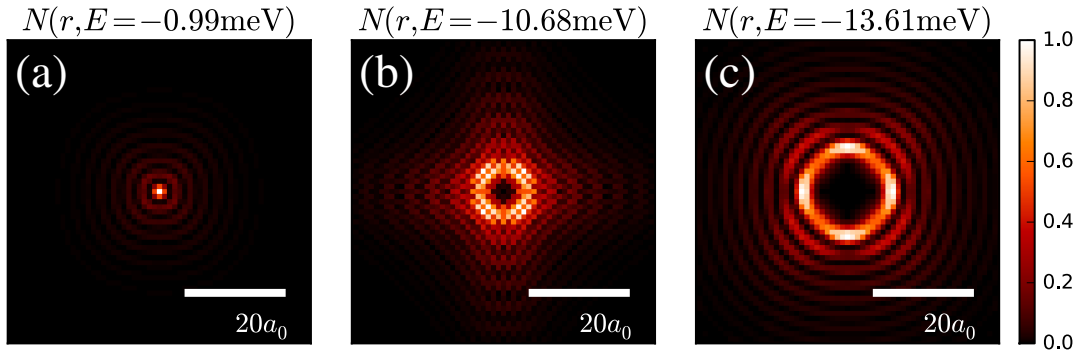


Figure 9.3: LDOS near a vortex from the non-self-consistent calculation with the five-band model from Ref. [20] and NNN pairing of $\Delta_{s\pm}^0 = 15\text{meV}$, (a) at the lowest bound state energy, (b) at an energy where the electron-band contribution dominates, and (c) at an energy where the γ -band contribution dominates.

9.4.2 Non-Self-Consistent Approach on Five Band Model

Now, we check whether the single-band model is sufficient to describe vortex bound states within the energy range of interest. A simple insight can be gained by treating each band independently and estimating the energy of its lowest bound state to be $\Delta^2/2E_F$ following Caroli *et al.* [33] for the gap size Δ and the Fermi energy E_F specific to each band. Using measured Fermi energies and gap parameters [10, 21, 22, 30], we estimate the energies of the lowest bound states of the γ pocket and the electron pockets to be of the same order. However, the lowest bound state energies of the two smaller hole pockets are an order of magnitude larger. This rough estimate implies that the LDOS within the energy below 1meV should be dominated by bound states coming from the γ band and those coming from the two electron bands. If indeed each bound state comes from a single band, we expect to find bound states with LDOS distribution resembling what we predicted in section 4.1.

For concreteness, we carry out a non-self-consistent BdG calculation using the band structure given by Ref. [20] with five bands. Unfortunately, the γ -pocket Fermi surface of this band structure (dashed line in Fig. 9.1a) is far more isotropic compared to what has been measured in Ref. [30] and guided the band structure we use in the rest of this paper. Hence we do not expect as pronounced ‘ray’ features at low energies compared to what is shown in Fig. 9.2 from our (single-band) calculations and experiment. Another issue we face with a five-band calculation is the limitation on the accessible system size. For a system of size (101,101), we impose NNN pairing that is trivial in the orbital space having magnitude $\Delta_{s\pm} = 15\text{meV}$ in order to fit the vortex bound states within the system and minimize the boundary effect. As in the single-band calculation, we create a vortex at the center of the form given in Eq. (9.3), however with $\xi = 10a_0$. Figure 9.3 shows the resulting LDOS at different bound state energies. At the lowest energy there is no clear sign of ‘rays’ though a small amount of anisotropy is still present, as expected from the smaller γ -band anisotropy (see Fig. 9.3a). Figures 9.3b and c show typical LDOS images of vortex bound states at higher energies. Figure 9.3b looks very different from the LDOS distribution obtained in section 4.1 and we hence assign the corresponding bound state to the electron pockets. However, the LDOS shown in Fig. 9.3c shows the same ‘hot spots’ as obtained within our single-band calculation and shown in Fig. 9.2f. Focussing on the γ band should thus suffice to capture the features observed in Ref. [8].

9.4.3 Self-Consistent Approach

Figure 9.4 shows the results from the (single-band) self-consistent calculation. We compare two pairing interactions – on-site attraction $U = -0.35\text{eV}$, and

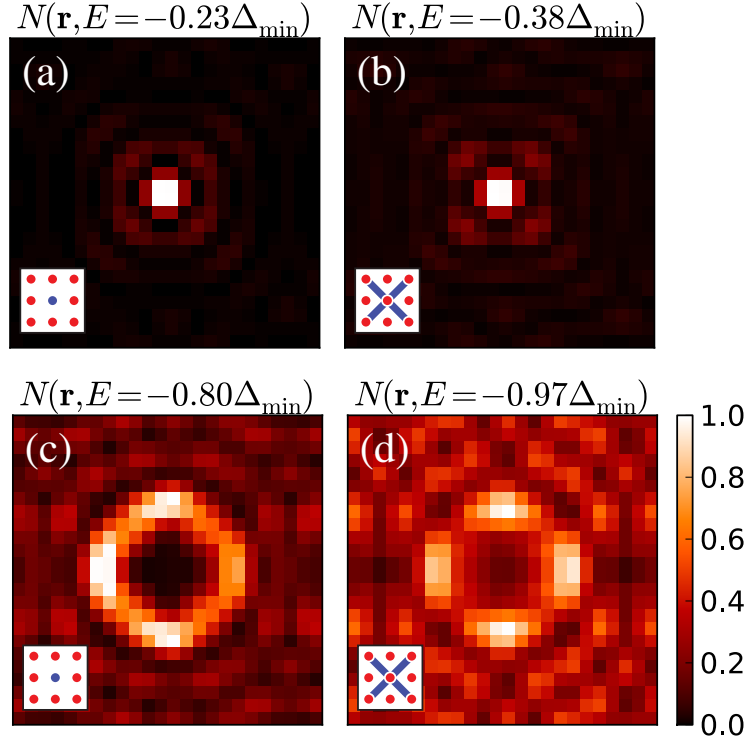


Figure 9.4: Local density of states near a vortex within our self-consistent calculation. Again, $N(\mathbf{r}, E)$ is normalized within each image. (a) is the LDOS at the lowest bound state energy with on-site attraction $U = -0.35\text{eV}$, and (c) is at higher energy. (b) and (d) are with NNN attraction $V' = -0.3\text{eV}$. The inset in each figure represents the local attractive interaction in the singlet pairing channel.

NNN attraction $V' = -0.3\text{eV}$ – for a system with magnetic unit cell of dimensions $(L_x, L_y) = (19, 38)$. This corresponds to a full lattice size of $(N_x, N_y) = (38 \times 19, 19 \times 38)$. In zero field, the two cases lead to a uniform superconducting gap of $\Delta_s^0 = 27\text{meV}$ and $\Delta_{s^\pm}^0 = 10\text{meV}$, respectively. We have chosen U and V' such that the coherence length $\xi \propto \Delta^{-1}$ is small compared to the inter-vortex spacing. This allows us to focus on a nearly isolated vortex within the computationally feasible size of the magnetic unit cell. Although the resulting gap values are an order of magnitude larger than what is known experimentally, this should not affect the validity of the results in a qualitative manner. Both at low energy and at higher

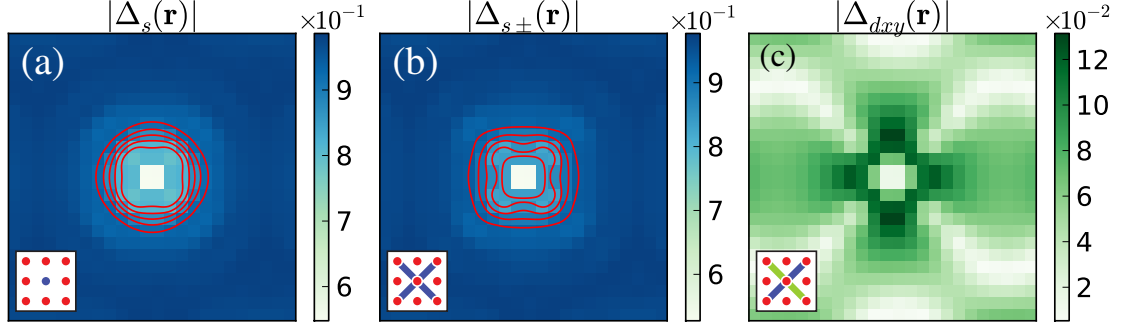


Figure 9.5: Spatial distribution of different symmetry components of order parameters. (a) $\Delta_s(\mathbf{r})$ for on-site attraction $U = -0.35\text{eV}$. (b) $\Delta_{s\pm}(\mathbf{r})$ and (c) $\Delta_{d_{xy}}(\mathbf{r})$ for NNN pairing $V' = -0.3\text{eV}$. The values have been normalized by the value of the dominant order parameter in the absence of magnetic field for each case: Δ_s^0 for (a), and $\Delta_{s\pm}^0$ for (b), (c). The equal-amplitude contours in red go from 0.825 for the innermost to 0.925 for the outermost contours (after normalization) with equal intervals between the contours in between. The insets again indicate the structure of the local order parameter. Note that the color-scale for $\Delta_{d_{xy}}(\mathbf{r})$ is much smaller than for $\Delta_s(\mathbf{r})$.

energy close to the gap value, we observe features that qualitatively agree with the results obtained in the previous section.

The self-consistent calculation also allows us to study the local order parameters of a given structure near a vortex. Unlike for the on-site attraction, where $\Delta_s(\mathbf{r})$ is the only allowed gap function, order parameters of different symmetries can mix near a vortex for NNN attraction. A near-vortex map of $\Delta_s(\mathbf{r})$ for on-site pairing shown in Fig. 9.5a indeed shows almost isotropic healing of the order parameter away from the vortex core. However, for the NNN attraction which leads to uniform s^\pm -wave pairing in zero-field, the secondary order parameter $\Delta_{d_{xy}}(\mathbf{r})$ is induced near the vortex. Coupling between this secondary order parameter and the primary $\Delta_{s\pm}(\mathbf{r})$ leads to a strong angular variation of both components as can be seen in Fig. 9.5b and c.

To gain further insight into the admixing of a secondary order parameter near a vortex for the anisotropic pairing, we analyze the Ginzburg-Landau free-energy density. The free-energy density for s -wave and d -wave order parameters reads

$$\begin{aligned} f = & \alpha_s |s|^2 + \alpha_d |d|^2 + \beta_1 |s|^4 + \beta_2 |d|^4 + \beta_3 |s|^2 |d|^2 \\ & + \beta_4 (s^{*2} d^2 + \text{c.c.}) + \gamma_s |\vec{D}s|^2 + \gamma_d |\vec{D}d|^2 \\ & + \gamma_v (D_x s D_y d^* + D_y s D_x d^* + \text{c.c.}), \end{aligned} \quad (9.12)$$

where s and d are shorthands for $s(\mathbf{r})$ and $d(\mathbf{r})$, the order-parameter fields for the s^\pm and d_{xy} gaps, respectively, and $D_i = \partial_i - ieA_i$ is the covariant derivative. The fields $s(\mathbf{r})$ and $d(\mathbf{r})$ can be thought of as $\Delta_{s/s^\pm}(\mathbf{r})$ and $\Delta_{d_{xy}}(\mathbf{r})$ after coarse graining. This type of admixing near a vortex has previously been studied in the context of cuprates, leading to the prediction of a fourfold-anisotropic order parameter around a vortex [15–18]³. As the large halo around vortices in cuprates [34] hindered the observation of this admixing, LiFeAs presents an opportunity for this observation.

The spatial variation of the secondary component d_{xy} in Fig. 9.5c is largely due to the derivative coupling, the term proportional to γ_v in Eq. (9.12). This intermixing term is expected to be large when the s -wave order parameter is of s^\pm type, since the same NNN pairing interaction is responsible for both s -wave and d -wave order parameter. For $|s| \gg |d|$ and $|\vec{D}s| \gg |\vec{D}d|$ the spatial structure of the d_{xy} component is determined largely by the structure of the s -wave component. Minimizing Eq. (9.12) with respect to $d(\mathbf{r})$ and keeping only terms up to linear order in $d(\mathbf{r})$, we find

$$-\gamma_d \vec{D}^2 d + \alpha_d d + \beta_3 |s|^2 d + \beta_4 s^2 d^* = \gamma_v (D_x D_y + D_y D_x) s. \quad (9.13)$$

³The microscopic model we consider is related to the single-band model of cuprates through rotation by 45° , the roles played by s -wave and d -wave order parameters are reversed and our d -wave order parameter is of d_{xy} form rather than $d_{x^2-y^2}$.

Hence, the curvature in the leading s -wave component will induce the secondary (d_{xy}) component. Now, consider a single isolated vortex. As $s(\mathbf{r})$ is recovered at the length scale of the coherence length ξ away from the core of the vortex, we expect a large $d(\mathbf{r})$ due to coupling to the large curvature of $s(\mathbf{r})$ at this distance. Since $\xi = \hbar v_F / \pi \Delta \sim 3.0 a_0$ for the uniform gap value with $V' = -0.3$ eV, this is in agreement with the positions of the maxima of $d(\mathbf{r})$ in Fig. 9.5c as a function of $|\mathbf{r}|$ setting the vortex core at the origin. We can also explain the angular variation and the form of the anisotropy of $d(\mathbf{r})$ in this framework. If we assume $s(\mathbf{r}) = f(r)e^{i\theta}$ with a slowly changing $f(r)$ and the azimuthal angle θ measured from the Fe-Fe direction, we find from Eq. (9.13)

$$d(\mathbf{r}) \sim \partial_x \partial_y s(\mathbf{r}) \sim e^{-i\theta} (1 + 3e^{4i\theta}), \quad (9.14)$$

ignoring the phase due to the magnetic field. The structure of the derivative hence gives rise to a four-fold anisotropy, which explains the fact that $|d(\mathbf{r})|$ is maximum in the Fe-Fe direction, while it is suppressed along the 45° direction. Coupling to $d(\mathbf{r})$ gives then in turn cause for the four-fold anisotropy in $s(\mathbf{r})$.

9.5 Conclusion

We have contrasted the effects of anisotropic s^\pm -wave (NNN) pairing and isotropic s -wave (on-site) pairing on the near-vortex local density of states in LiFeAs by solving Bogoliubov-de Gennes equations both non-self-consistently and self-consistently. We have found qualitative changes in the geometric distribution of the density of states as a function of energy. At low energies, the anisotropy of the vortex bound state, and hence the LDOS, is determined by the normal state low energy electronic structure, independent of the gap structure. Different

pairing structures, however, lead to qualitatively different LDOS distributions at higher energies: While the isotropic s -wave shows a square-like feature of roughly equal intensity, four ‘hot spots’ develop in the case of an (anisotropic) s^\pm -wave gap. Indeed, our results for the latter case qualitatively agree with recent experiments [8].

From the self-consistent treatment we have further found a difference in the recovery of the order parameter away from the vortex core: a pronounced angular dependence of the s^\pm -wave gap compared to isotropic behavior for the s -wave gap. Employing a Ginzburg-Landau analysis, we have explained this difference through admixing of a secondary order parameter supported by the NNN interaction. Note that such intermixing is negligible for an s -wave pairing with a dominant on-site pairing interaction, as no other pairing instabilities are nearby. For the NNN interaction, however, s^\pm - and d_{xy} -wave instabilities have comparable transition temperatures. Detection of the anisotropy or even the secondary order parameter would be a strong proof of the unconventional nature of the pairing.

In this work, we focused on the γ band with interest in low energy properties, as this is the band with the smallest gap [21, 22]. Hence, for features at energies less than the gap scale, we expect our calculation to capture salient features of in-field STS experiments. The comparison between the calculated LDOS for the single- and the five-band models and the results in Ref. [8] supports this conjecture.

In closing we note that our calculation captures Friedel-like oscillations, frequently referred to as quasi-particle interference (QPI), due to vortices. QPI in the presence of vortices was successfully used to access phase information with STS in cuprates [35]. Recent in-field QPI experiments on FeSe have been interpreted to

be consistent with an s^\pm scenario when a vortex is treated as a magnetic scatterer for BdG quasiparticles [4]. However, a vortex is at once a point of gap suppression, a point with magnetic flux, and a point around which the order-parameter phase winds. While we treated vortices faithfully in the self-consistent calculation, we could not investigate effects of inter-pocket sign change as we only considered one pocket. An extension of the present work with the full band structure would be necessary to work out what to expect for different order-parameter possibilities, especially how the phase difference between different pockets affects in-field QPI.

BIBLIOGRAPHY

1. Hirschfeld, P. J., Korshunov, M. M. & Mazin, I. I. Gap symmetry and structure of Fe-based superconductors. *Rep. Prog. Phys.* **74**, 124508 (2011).
2. Stewart, G. R. Superconductivity in iron compounds. *Rev. Mod. Phys.* **83**, 1589 (2011).
3. Chen, C.-T., Tsuei, C. C., Ketchen, M. B., Ren, Z.-A. & Zhao, Z. X. Integer and half-integer flux-quantum transitions in a niobium-iron pnictide loop. *Nat. Phys.* **6**, 260 (2010).
4. Hanaguri, T., Niitaka, S., Kuroki, K. & Takagi, H. Unconventional *s*-wave superconductivity in Fe(Se,Te). *Science* **328**, 474 (2010).
5. Christianson, A. D. *et al.* Unconventional superconductivity in $\text{Ba}_{0.6}\text{K}_{0.4}\text{Fe}_2\text{As}_2$ from inelastic neutron scattering. *Nature* **456**, 930 (2008).
6. Lumsden, M. D. *et al.* Two-dimensional resonant magnetic excitation in $\text{BaFe}_{1.84}\text{Co}_{0.16}\text{As}_2$. *Phys. Rev. Lett.* **102**, 107005 (2009).
7. Li, S. *et al.* Spin gap and magnetic resonance in superconducting $\text{BaFe}_{1.9}\text{Ni}_{0.1}\text{As}_2$. *Phys. Rev. B* **79**, 174527 (2009).
8. Hanaguri, T. *et al.* Scanning tunneling microscopy/spectroscopy of vortices in LiFeAs. *Phys. Rev. B* **85**, 214505 (2012).
9. Kontani, H. & Onari, S. Orbital-fluctuation-mediated superconductivity in iron pnictides: Analysis of the five-orbital Hubbard-Holstein model. *Phys. Rev. Lett.* **104**, 157001 (2010).
10. Borisenko, S. V. *et al.* One-sign order parameter in iron based superconductor. *Symmetry* **4**, 251 (2012).

11. Brydon, P. M. R., Daghofer, M., Timm, C. & van den Brink, J. Theory of magnetism and triplet superconductivity in LiFeAs. *Phys. Rev. B* **83**, 060501 (2011).
12. Hänke, T. *et al.* Probing the unconventional superconducting state of LiFeAs by quasiparticle interference. *Phys. Rev. Lett.* **108**, 127001 (2012).
13. Hayashi, N., Ichioka, M. & Machida, K. Star-shaped local density of states around vortices in a type-II superconductor. *Phys. Rev. Lett.* **77**, 4074 (1996).
14. Wang, Y., Hirschfeld, P. J. & Vekhter, I. Theory of quasiparticle vortex bound states in iron-based superconductors: Application to scanning tunneling spectroscopy of LiFeAs. *Phys. Rev. B* **85**, 020506 (2012).
15. Joynt, R. Upward curvature of H_{c2} in high- T_c superconductors: Possible evidence for s - d pairing. *Phys. Rev. B* **41**, 4271 (1990).
16. Berlinsky, A. J., Fetter, A. L., Franz, M., Kallin, C. & Soininen, P. I. Ginzburg-Landau theory of vortices in d -Wave superconductors. *Phys. Rev. Lett.* **75**, 2200 (1995).
17. Ren, Y., Xu, J.-H. & Ting, C. S. Ginzburg-Landau equations and vortex structure of a $d_{x^2-y^2}$ superconductor. *Phys. Rev. Lett.* **74**, 3680 (1995).
18. Ichioka, M., Enomoto, N., Hayashi, N. & Machida, K. s - and d_{xy} -wave components induced around a vortex in $d_{x^2-y^2}$ -wave superconductors. *Phys. Rev. B* **53**, 2233 (1996).
19. Heeb, R., van Otterlo, A., Sigrist, M. & Blatter, G. Vortices in d -wave superconductors. *Phys. Rev. B* **54**, 9385 (1996).
20. Eschrig, H. & Koepernik, K. Tight-binding models for the iron-based superconductors. *Phys. Rev. B* **80**, 104503 (2009).

21. Borisenko, S. V. *et al.* Superconductivity without nesting in LiFeAs. *Phys. Rev. Lett.* **105**, 067002 (2010).
22. Umezawa, K. *et al.* Unconventional anisotropic s-Wave superconducting gaps of the LiFeAs iron-pnictide superconductor. *Phys. Rev. Lett.* **108**, 037002 (2012).
23. Hajiri, T. *et al.* Three-dimensional electronic structure and interband nesting in the stoichiometric superconductor LiFeAs. *Phys. Rev. B* **85**, 094509 (2012).
24. Hu, X., Ting, C. S. & Zhu, J.-X. Vortex core states in a minimal two-band model for iron-based superconductors. *Phys. Rev. B* **80**, 014523 (2009).
25. Jiang, H.-M., Li, J.-X. & Wang, Z. D. Vortex states in iron-based superconductors with collinear antiferromagnetic cores. *Phys. Rev. B* **80**, 134505 (2009).
26. Zhou, T., Wang, Z. D., Gao, Y. & Ting, C. S. Electronic structure around a vortex core in iron-based superconductors: Numerical studies of a two-orbital model. *Phys. Rev. B* **84**, 174524 (2011).
27. Gao, Y., Huang, H.-X., Chen, C., Ting, C. S. & Su, W.-P. Model of vortex states in hole-doped iron-pnictide superconductors. *Phys. Rev. Lett.* **106**, 027004 (2011).
28. Hung, H.-H. *et al.* Anisotropic vortex lattice structures in the FeSe superconductor. *Phys. Rev. B* **85**, 104510 (2012).
29. Ye, X.-S. Bound states and vortex core shrinking effects in iron-based superconductors. *Physica C: Superconductivity* **485**, 6 (2013).
30. Allan, M. P. *et al.* Anisotropic energy gaps of iron-based superconductivity from intraband quasiparticle interference in LiFeAs. *Science* **336**, 563 (2012).

31. Lee, B., Khim, S., Kim, J. S., Stewart, G. R. & Kim, K. H. Single-crystal growth and superconducting properties of LiFeAs. *Europhys. Lett.* **91**, 67002 (2010).
32. Kurita, N. *et al.* Determination of the upper critical field of a single crystal LiFeAs: The magnetic torque study up to 35 Tesla. *J. Phys. Soc. Jpn.* **80**, 013706 (2011).
33. Caroli, C., Gennes, P. D. & Matricon, J. Bound fermion states on a vortex line in a type II superconductor. *Phys. Lett.* **9**, 307 (1964).
34. Hoffman, J. E. *et al.* A four unit cell periodic pattern of quasi-particle states surrounding vortex cores in $\text{Bi}_2\text{Sr}_2\text{CaCu}_2\text{O}_{8+\delta}$. *Science* **295**, 466 (2002).
35. Hanaguri, T. *et al.* Coherence factors in a high- T_c cuprate probed by quasi-particle scattering off vortices. *Science* **323**, 923 (2009).

APPENDIX A

DYNAMICAL SUSCEPTIBILITY AT NON-ZERO TEMPERATURE

Every spectroscopy is a measurement of response to time-dependent perturbation. Here, two important time scales exist: First is the *period*, or *inverse frequency* $T \sim 1/\omega$ of the probing signal, which is a measure of how fast the perturbation varies. Second is the *thermal equilibration time* τ , over which the system relaxes to thermal equilibrium. Two limits exist that are easy to approach: First is when $\omega\tau \ll 1$. In this limit, the system reaches thermal equilibrium faster than the time scale over which the measurement is done. It is therefore safe to assume that what is measured at time t is its “static” expectation value in a system with the perturbation at time t . If we let \hat{A} and $\Phi(t)$ represent the observable and the external perturbation, this relation can be written as

$$\langle \hat{A} \rangle(t) \approx \frac{1}{\text{Tr}\left(e^{-\beta\hat{H}[\Phi(t)]}\right)} \text{Tr}\left(e^{-\beta\hat{H}[\Phi(t)]}\hat{A}\right) \quad (\text{A.1})$$

In the opposite limit $\omega\tau \gg 1$, on the other hand, the effect of thermalization during measurement can be ignored. The time-dependent response of the system at non-zero temperature therefore reduces to an ensemble average of the response of the eigenstates of non-perturbed Hamiltonian. Especially in the limit where the perturbation is infinitesimal, the response can be calculated as dynamical susceptibility within linear response theory. In this chapter, we derive dynamical susceptibility in a system with non-zero temperature.

A.1 Linear Response Theory at Non-zero Temperature

Let us consider a time-dependent Hmiltonian $\hat{H}(t) = \hat{H}_0 + \hat{H}_1(t)$, where \hat{H}_0 is the non-perturbed Hamiltonian, and $\hat{H}_1(t)$ is perturbation which is slowly turned on

$(\hat{H}_1(-\infty) = 0)$. Then at time $t = -\infty$, the density matrix $\hat{\rho} = \hat{\rho}_0 \equiv e^{-\beta\hat{H}_0}/Z$. Writing the time-dependent density matrix as the sum of the non-perturbed piece and a perturbed piece

$$\hat{\rho}(t) = \hat{\rho}_0 + \hat{\rho}_1(t). \quad (\text{A.2})$$

The equation of motion of ρ

$$i \frac{d\hat{\rho}}{dt} = [\hat{H}, \hat{\rho}] \quad (\text{A.3})$$

can be rewritten as

$$i \frac{d\hat{\rho}_1}{dt} = [\hat{H}_0, \hat{\rho}_1] + [\hat{H}_1, \hat{\rho}_0] + O(\hat{H}_1^2) \quad (\text{A.4})$$

Integration of the above equation leads to

$$\hat{\rho}_1(t) = \hat{\rho}_1(-\infty) - i e^{-i\hat{H}_0 t} \left\{ \int_{-\infty}^t dt' e^{i\hat{H}_0 t'} [\hat{H}_1(t'), \hat{\rho}_0] e^{-i\hat{H}_0 t'} \right\} e^{i\hat{H}_0 t}. \quad (\text{A.5})$$

Expectation value of an observable \hat{A} at time t is therefore

$$A(t) = \langle \hat{A} \rangle(t) = \langle \hat{A} \rangle_0 - i \text{Tr} \left\{ e^{-i\hat{H}_0 t} \left[\int_{-\infty}^t dt' e^{i\hat{H}_0 t'} [\hat{H}_1(t'), \hat{\rho}_0] e^{-i\hat{H}_0 t'} \right] e^{i\hat{H}_0 t} \hat{A} \right\} \quad (\text{A.6})$$

where $\langle \cdot \rangle_0$ is the thermal average in the unperturbed system:

$$\langle \hat{A} \rangle_0 \equiv \frac{\text{Tr} [\hat{A} e^{-\beta\hat{H}_0}]}{\text{Tr} [e^{-\beta\hat{H}_0}]} \quad (\text{A.7})$$

Defining $\hat{O}^{(I)}(t) \equiv e^{i\hat{H}_0 t} \hat{O} e^{-i\hat{H}_0 t}$, Eq. (A.6) can be written compactly as

$$A(t) = \langle \hat{A} \rangle_0 - i \int_{-\infty}^t dt' \left\langle [\hat{A}^{(I)}(t), \hat{H}_1^{(I)}(t')] \right\rangle_0 \quad (\text{A.8})$$

Now let us consider perturbation of the following form

$$\hat{H}_1(t) = -\hat{B} \cdot \Phi(t). \quad (\text{A.9})$$

Here, \hat{B} and $\Phi(t)$ can be multi-component objects. In the linear response regime, however, each component can be treated independently. Assuming $\langle \hat{A} \rangle_0 = 0$ for simplicity, we can write

$$A(t) = \int_{-\infty}^{\infty} dt' \chi_{AB}^R(t, t') \Phi(t') \quad (\text{A.10})$$

where χ_{AB}^R is the *retarded susceptibility*

$$\chi_{AB}^R(t, t') \equiv i\Theta(t - t') \left\langle \left[\hat{A}^{(I)}(t), \hat{B}^{(I)}(t') \right] \right\rangle_0 \quad (\text{A.11})$$

A.2 Spectral Representation

Often the measurement is presented in frequency.

For notational convenience we suppress superscript (I) and subscript 0 as well as the hats ($\hat{\cdot}$) for operators. The retarded susceptibility at frequency ω is defined as

$$\chi_{AB}^R(\omega) = i \int_{-\infty}^{\infty} dt \Theta(t) \langle [A(t), B(0)] \rangle \quad (\text{A.12})$$

Expanding this out,

$$\chi_{AB}^R(\omega) = \int_0^{\infty} dt \text{Tr} \left(\rho_0 e^{iH_0 t} A e^{-iH_0 t} B - \rho_0 B e^{iH_0 t} A e^{-iH_0 t} \right) \quad (\text{A.13})$$

Trace of the first term is

$$\sum_m \left\langle m \left| \rho_0 e^{iH_0 t} A e^{-iH_0 t} B \right| m \right\rangle = \frac{1}{Z} \sum_{m,n} e^{-\beta E_m} e^{iE_m t} e^{-iE_n t} \langle m | A | n \rangle \langle n | B | m \rangle \quad (\text{A.14})$$

where $|m\rangle$ and E_m are an eigenstate of H_0 and its energy. After similar expansion of the second term, we arrive at the following expression for the dynamical susceptibility

$$\chi_{AB}^R(\omega) = \frac{1}{Z} \sum_{m,n} \left(e^{-\beta E_m} - e^{-\beta E_n} \right) \langle m | A | n \rangle \langle n | B | m \rangle \left(i \int_0^{\infty} dt e^{i(\omega + E_m - E_n)t} \right) \quad (\text{A.15})$$

For the convergence of the last integral, we add a small decaying factor

$$i \int_0^\infty dt e^{i(\omega+E_m-E_n+i\eta)t} = -\frac{1}{\omega + i\eta + E_m - E_n}. \quad (\text{A.16})$$

Finally we arrive at the spectral representation of dynamical susceptibility

$$\chi_{AB}^R(\omega) = \frac{1}{Z} \sum_{m,n} \left(e^{-\beta E_n} - e^{-\beta E_m} \right) \frac{\langle m|A|n\rangle \langle n|B|m\rangle}{\omega + i\eta + E_m - E_n} \quad (\text{A.17})$$

At non-zero temperature, it is convenient to consider imaginary time evolution instead of real time evolution. Known as *Matsubara* formalism, working with imaginary time not only handles singularities in a more natural way (without explicitly introducing η as in the previous section), but also provides a way to extract dynamical susceptibilities from numerical simulations of thermal systems.

Defining the “imaginary time-evolved operator”

$$A(\tau) \equiv e^{H_0\tau} A e^{-H_0\tau} \quad (\text{A.18})$$

and imaginary time-ordered susceptibility

$$\chi_{AB}(\tau) = \langle T_\tau A(\tau) B(0) \rangle \quad (\text{A.19})$$

where T_τ is imaginary time-ordering operator. Susceptibility at Matsubara frequency $i\omega_n$ is

$$\begin{aligned} \chi_{AB}(i\omega_n) &= \int_0^\beta d\tau e^{i\omega_n \tau} \chi_{AB}(\tau) \\ &= \frac{1}{Z} \sum_{m,n} \left(e^{-\beta E_n} - e^{-\beta E_m} \right) \frac{\langle m|A|n\rangle \langle n|B|m\rangle}{i\omega_n + E_m - E_n} \end{aligned} \quad (\text{A.20})$$

From this, we see that the Matsubara susceptibility is related to retarded susceptibility by analytic continuation:

$$\chi_{AB}^R(\omega) = \chi_{AB}(i\omega_n) \Big|_{i\omega_n \rightarrow \omega} \quad (\text{A.21})$$